To the Graduate Council:

I am submitting herewith a dissertation written by Özgür Polat entitled "Wide-Range Characterization of Current Conduction in Superconductors-Tuning Their Properties by Nanoscale Modification of Materials." I have examined the final electronic copy of this dissertation for form and content and recommend that it be accepted in partial fulfillment of the requirements for the degree of Doctor of Philosophy, with a major in Physics.

James R. Thompson, Major Professor

We have read this dissertation
and recommend its acceptance:

Tolga Aytug

Adriana Moreo

Hanno H. Weitering

Veerle Keppens

Accepted for the Council:

Carolyn R. Hodges

Vice Provost and
Dean of the Graduate School

(Original signatures are on file with official student records.)

Wide-Range Characterization of Current Conduction in Superconductors-Tuning Their Properties by Nanoscale Modification of Materials

A Dissertation

Presented for

The Doctor of Philosophy

Degree

The University of Tennessee, Knoxville

Özgür Polat

December 2009

Acknowledgements

Foremost, I would like to express my deepest gratitude to my advisors Dr. James R. Thompson and Dr. Tolga Aytug for their continuous support of my PhD study and research, for their patience, motivation, enthusiasm, and immense knowledge. Their guidance helped me in all the time of research and writing of this thesis. I can not imagine having better advisors and mentors for my PhD study. They have also helped me to open my eyes toward a beauty of the nature and science.

I am also extremely grateful to Dr. David Christen who is our group leader and also served on my committee. His guidance and advice have assisted me very much.

Besides my advisors, I would like to thank the rest of my thesis committee: Dr. Adriana Moreo, Dr Hanno Weitering, and Dr. Veerle Keppens, for their encouragement, insightful comments, and suggestions.

My sincere thanks go to Dr. M. P. Paranthaman, for giving me the opportunities in his group and leading my work on diverse exciting projects. Many thanks also go to my collaborators at ORNL, NC A&T University, and SuperPower Inc.

The lively and always cooperative atmosphere in our lab was certainly inspired by diligent PhD students and Postdocs. Many, many thanks go to John W. Sinclair, Anota Ijaduola, Yifei Zhang, Yuri Zuev, K. Kim, X. Xiong, S. Cook, Fred List, and our group secretary Nancy Ward, for an excellent working environment, help in practical matters and many interesting discussions about all possible topics.

My final, and most heartfelt, acknowledgment must go to my parents, my father and my mother, and my family, my wife and my daughter. Their support, encouragement,

and endless love make it possible for me to complete my work successfully without any difficulties.

Abstract

Significant progress has been made in the development of $YBa_2Cu_3O_{7-x}$ (YBCO)-based coated conductors (CCs) since the discovery of YBCO in 1987. Nowadays, high temperature superconductor (HTS) materials are advancing toward wide application areas in medical physics, industry, and science. The successful applications of these materials require clear understanding of the mechanisms controlling the current carrying capacity. It has been demonstrated the maximum current that a HTS can support is strongly affected by the vortex dynamics within the HTS materials. In this dissertation, we employed a combination of methods: conventional transport, magnetometry in a swept magnetic field, and "flux creep" measurements to obtain current density *J* vs. electric field *E* characteristics. Moreover, we determined the superconducting properties of the HTS materials as a function of temperature, magnetic field strength, and field orientation. Another significant issue in the commercialization of HTS materials is the manufacturing cost of CCs. Although the superconducting films can be deposited on the flexible biaxially textured coating on metallic substrates with high quality performance, these substrates require deposition of several buffer layers to achieve high quality HTS coatings. Hence, in the second part of this thesis, we focused on the simplification of the Ion Beam Assisted Deposition (IBAD) buffer architecture. Development of a simplified architecture is one of the key issues for reduced manufacturing cost of second generation superconducting wire production. In this thesis, we demonstrated that the present IBAD template can be simplified by eliminating one of the buffer layers from the standard architecture. In addition, we displayed that the $LaMnO_3$ (LMO) cap layers can be further

functionalized by replacing it a nanocomposite LMO:MgO cap layer, resulting in two-phase separated composite MgO nanostructures within the LMO matrix. Measurements of orientation-dependent J_c of YBCO coatings deposited on these nanostructured cap buffer layers revealed enhanced correlated *c*-axis pinning and improved in-field J_c performance. Our results underscore that (i) better understanding of vortex dynamics is a very valuable tool to establish practical level of HTS operation and (ii) formulation of novel material fabrication approaches is indispensable in the pursuit of more efficient, economical, high performance superconducting devices.

Table of Contents

List of Figures

Chapter 1

Introduction

1.1 Introductory Remarks

In 1911, Heike Kamerlingh Onnes discovered superconductivity and was awarded the Nobel Prize in 1913 for this discovery. He found that the resistance of mercury (Hg) dropped continuously as the temperature decreased, then abruptly changed when the transition temperature, T_c, was reached near 4.2 Kelvin as shown in Fig. 1.1. Below this temperature, mercury behaves entirely differently: its electrical resistance changes dramatically and becomes zero at T_c, defined as superconducting transition temperature. At this temperature, a small electrical current could be transported without losses. He called this phenomenon superconductivity [1]. Since then, many more superconductors have been discovered, including many metallic elements, together with numerous alloys and compounds. At the critical temperature T_c, a superconductive material undergoes to a phase transition from a normal metallic state to a superconducting state. The first superconductors (SCs) discovered were elements, alloys, and compounds, which have low T_c below about 20 K. These superconducting materials are called as low temperature SCs. After 75 years, in 1986 Bednorz and Muller discovered the first high temperature superconductor (HTS) in a $La_{2-x}Ba_xCuO_4$ material with a T_c in excess of 30 K [2]. This discovery opened a new era in the field of superconductivity and solid state physics. The following year M. K. Wu [3] discovered another cuprate (copper oxide), $YBa_2Cu_3O_{7-\delta}$ (YBCO), with a T_c of 92 K. Now YBCO has become one of the most studied cuprates.

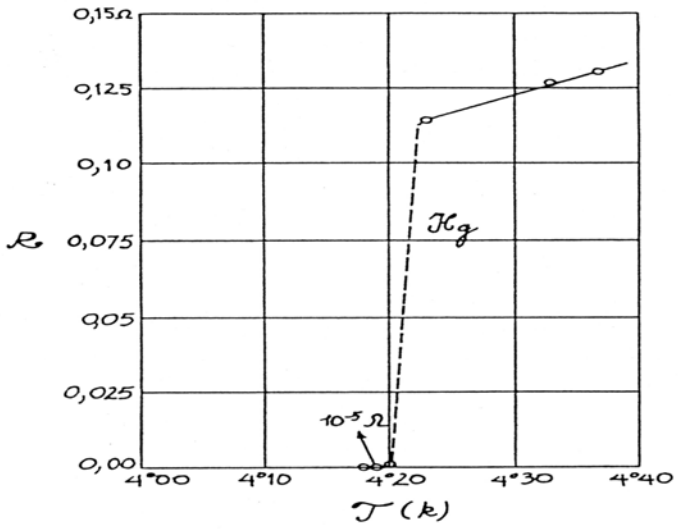

Figure 1.1: Resistance versus Temperature

The T_c of YBCO is higher than the boiling point of liquid nitrogen, 77 K. Currently, liquid nitrogen is widely used as a refrigerant for YBCO.

The possibility of operating HTS materials at liquid nitrogen temperature has triggered world wide research and commercial investments. Much research has been directed toward electric power equipment, such as motors, magnets, generators, and transmission lines. All of these power applications require superconducting material to be formed into a long and flexible conductor for replacement of its counterpart copper wire, which is currently being used in these applications. At the same time, significant market demand means that we need to fully exploit the current-carrying capability of HTS wires and reduce the manufacturing cost of these wires. Technologically, the main aim is to produce robust, economical, and scalable processes for manufacturing HTS wires, which

can support high current at 77 K and in high magnetic fields. Until recently, the first generation (1G) Bi-based HTS wires fabricated by the powder-in-tube method have dominated the market. However, there are some issues with the 1G wire, including low current carrying capability at moderate to high magnetic fields and significant cost of the silver matrix surrounding the Bi-based HTS material. Driven by these issues of cost and poor performance in high magnetic fields, a major transition is in progress from 1G to the second generation (2G) of YBCO-based HTS wires that promise reduced cost material processing and labor, accompanied with much better conduction of high currents in high temperatures and at high magnetic fields. These 2G wires utilize a HTS thin film formed on a flexible metallic substrate and are called coated conductors (CC). The quality of CCs is strongly affected by the substrate (tape) material. Hence, the substrate must fulfill many requirements, including good and desirable crystallographic texture and non-reactivity at high temperatures with the other materials that are employed to form the HTS coatings. The performance improvement of well textured HTS materials can be achieved through a better understanding of vortex-vortex and vortex-defect interactions. The study of vortex physics is one of the most appealing research areas in solid state physics, because the behavior of vortices governs the physical properties of SCs, including the maximum electric current that a superconducting material can support. A key question for investigation is how the superconducting mixed state, in which the external magnetic field penetrates the material in the form of quantized vortex filaments, is changed by the behavior of vortices when a transport current is applied.

If the vortices are forced to move, there will be energy dissipation; this causes heating and it is inevitable, unless the vortices are immobilized, or "pinned" by inhomogeneities in the material, which can be either natural or artificially engineered. In fact, vortex motion (accompanied by power dissipation) occurs easily in HTS materials, due to a combination of high anisotropy and a short coherence length that enhances the effect of thermal fluctuations of the vortices. These thermal fluctuations lead to strong magnetic relaxation and limit the current-carrying capacity of these materials. The mobile vortices in the media create an electric field E parallel to the current density J, which causes power dissipation in the material. The material's E-J characteristics encapsulate the electrodynamical properties of a HTS material. In many cases, the $E(J)$ characteristics are well described by a power-law relation, $E \sim J^n$. This relation has been demonstrated by magnetic and transport measurements.

The focus of this dissertation is twofold: characterizing and analyzing superconducting materials in order to establish the limits of performance that are achievable and addressing material issues to improve properties and further decrease the manufacturing cost of wires without compromising their performance levels. The first part of this thesis focuses on the performance of the HTSs in magnetic fields, where vortex interactions with themselves and with material inhomogeneities determine the material's current conduction capability for technological applications. Of particular interest are the wide range studies of 'current-voltage' $E(J)$ characteristics of second generation (2G) wires, which provide understanding of the electrical properties of these materials in regimes of technological relevance. A combination of electrical and

contactless magnetic–based methods has been employed to broadly characterize and analyze the relevant superconductive properties as a function of temperature, magnetic field, orientation in field, and effective electric field levels commensurate with real devices. The second part of this dissertation focuses on the materials development: specifically, improvement of materials processing/performance that could potentially lead to reduced manufacturing cost of second generation superconducting wire production.

1.2 Overview of the Thesis

In chapter 2, we will present a general scientific background describing the basic phenomena and the theory of superconductivity relevant to our study. Subsequently, we will focus on the vortex dynamics. Moreover, we will discuss the calculation of the J_c from contact-free magnetic hysteresis studies.

The coated conductors will be reviewed in chapter 3. We will describe the kind of fabrication methods that are used to obtain biaxially textured metallic substrates. Epitaxial thin films, buffer layers, as well as issues in one of the leading techniques, the Ion Beam Assisted Deposition (IBAD) method that is widely used to fabricate coated conductors, will also be discussed in detail

Chapter 4 explains the experimental equipment and procedures, which were used in this thesis. The film synthesis and electromagnetic characterization of superconductor films will also be discussed in detail.

A detailed investigation of vortex dynamics in rare-earth (REBCO) thin films is the subject of chapter 5. In chapter 5, electrical properties of two REBCO films, (SmY)BCO and (GdY)SmBCO will be discussed. We will first present their field performance, followed by creep measurements and wide-range *E*-*J* characteristics of these samples will be discussed. The obtained experimental data will be interpreted by the assistance of two theoretical models, the vortex-glass and collective creep theories.

The first section of chapter 6 concentrates on the buffer layer simplification in IBAD technique, since simplification of the present IBAD architecture is one of the key issues for reduced manufacturing cost of second-generation superconducting wire production. In the second section, we will show that the standard $LaMnO_3$ (LMO) cap layer can be functionalized by replacing it with a composite LMO:MgO layer. The formation of phase separated MgO nanocolumns within the composite cap layers and the impact of these nanostructures on the electrical properties of YBCO films will be discussed in detail.

In chapter 7, we will summarize the main experimental results presented in this thesis.

Chapter 2

Theoretical Background

In this chapter, we shall develop theoretical background employed during our investigations. First, the London equations and Ginzburg-Landau theory will be discussed, which will be followed by the review of vortex dynamics in the HTS material. Magnetic relaxations of the critical current density and electric field-current density (*E*-*J*) characteristics will also be detailed in this chapter. Finally, the Bean critical state model will be described.

2.1 Physics of Superconductors

2.1.1 The London Equations

If a SC is cooled below its T_c in the presence of a weak magnetic field, the internal magnetic field is expelled. Hence, the SC shows perfect diamagnetism. This phenomenon is called the Meissner effect and was discovered by Meissner and Ochsenfeld in 1932 [4]. According to the Meissner effect, SCs develop currents on the surface, which create magnetic fields that exactly cancel the external field. Thus, the interior of SC material is left in a field-free state with flux density $B = 0$. In addition, the Meissner effect also implies that a type-I SC will be destroyed at a certain magnetic field known as the critical field, H_c. In 1935, the London brothers Fritz and Heinz proposed their equations that are consistent with the Meissner effect and showed and how these can

be used with Maxwell's equations to predict the magnetic field and surface current variations with the distance from the surface of SC [5]. The London equations for the vector potential **A** and the macroscopic flux density **B** can be written as follows

$$\mathbf{A} = -\frac{m}{n_s e^2}\mathbf{J} \tag{2.1}$$

$$\mathbf{B} = -c\nabla \times \frac{m}{n_s e^2}\mathbf{J} \tag{2.2}$$

Here n_s is the density of superconducting charge carriers and m and e are the carrier's mass and charge, respectively.

Taking the curl of both sides of Eq. (2.2), and using Maxwell's equation, we obtain

$$\nabla^2\mathbf{B} = \frac{1}{\lambda^2}\mathbf{B} \quad \text{and} \quad \nabla^2\mathbf{J} = \frac{1}{\lambda^2}\mathbf{J} \tag{2.3}$$

These equations indicate that currents and magnetic fields could exist only within a distance of λ within the SC material. The important length scale λ, the London penetration depth, is given by $\lambda = \frac{mc^2}{4\pi n_s e^2}$ relation.

2.1.2 Ginzburg-Landau (GL) Theory

In 1950, two Russian physicists Ginzburg and Landau [6] formulated their phenomenological theory of SC. The GL theory is based on Landau's formulation for second order phase transition. The transition from the normal state into the superconducting state at T_c is a second order phase transition in the absence of a magnetic field. In order to describe this transition, GL introduced a complex pseudowave function ψ as an order parameter. This can be interpreted as the effective wave function of the superconducting electrons whose density is given by

$$n_s = |\psi|^2 \tag{2.4}$$

The free energy of the SC can be expanded in a power series of $|\psi|^2$ close to T_c. Assuming ψ is small and slowly varying in space; the energy density is given by

$$f_s = f_n + \alpha|\psi|^2 + \frac{\beta}{2}|\psi|^4 + \frac{1}{2m^*}\left|\left(\frac{\hbar}{i}\nabla - e^*\mathbf{A}\right)\psi\right|^2 + \frac{H^2}{8\pi} \tag{2.5}$$

In the absence of fields and gradients (**H**=0 and **A**=0), one obtains

$$f_s - f_n = \alpha|\psi|^2 + \frac{\beta}{2}|\psi|^4 \tag{2.6}$$

Let's find $|\psi|^2$ for which the energy density of SC is a minimum by setting $\frac{\partial f_s}{\partial|\psi|^2} = 0$,

$$\frac{\partial f_s}{\partial |\psi|^2} = 0 = \alpha + \beta |\psi|^2 \tag{2.7}$$

We obtain

$$|\psi|^2 = -\frac{\alpha}{\beta}. \tag{2.8}$$

When the value of $|\psi|^2$ is substituted back into Eq. (2.6), one finds

$$f_s - f_n = -\frac{\alpha^2}{2\beta} = -\frac{H_c^2}{8\pi}, \tag{2.9}$$

which is called the condensation energy. Here $\alpha(T) = \alpha(0)(1 - T/T_c)$ near T_c, where $\alpha(0)$ must be less than zero for a non-zero solution of ψ. β is constant near T_c.

The thermodynamical critical field, H_c, can be approximated by the relation $H_c(T)=H_c(0)[1-(T/T_c)^2]$, where $H_c(0)$ is the critical field at zero temperature. Regarding notation: the magnetizing field **H**, flux density **B**, magnetic moment **m**, etc. are vector quantities. In general, however, it is the magnitude of these quantities that is needed; consequently, the full vector notation will be used only when taking explicit account of the direction.

Minimizing the overall free energy, i.e., Eq. (2.5), the GL differential equations are obtained

$$\alpha\psi + \beta|\psi|^2\psi + \frac{1}{2m^*}\left(\frac{\hbar}{i}\nabla - \frac{e^*}{c}\mathbf{A}\right)^2\psi = 0 \tag{2.10}$$

and the microscopic supercurrent density is

$$\mathbf{J} = \frac{e^* \hbar}{2m^* i}\left(\psi^* \nabla \psi - \psi \nabla \psi^*\right) - \frac{e^{*2}}{m^* c}\left|\psi\right|^2 \mathbf{A} \tag{2.11}$$

where $e^*=2e$ and $m^*=2m$.

The two GL equations have simple solutions in the following cases:

i) One case has $\psi=0$ where **A** is determined by $\mathbf{H} = \nabla \times \mathbf{A}$. This solution describes the normal state. *ii*) A second case with **A**=0 has $\psi = \psi_0 = \sqrt{\frac{-\alpha}{\beta}}$ (far from any surface), corresponding to a perfect Meissner state.

Two characteristic lengths can be deduced from the GL equations in the presence of weak magnetic fields. From equation (2.10), a temperature dependent coherence length can be obtained

$$\xi(T) = \frac{\hbar}{\left|2m^* \alpha(T)\right|^{1/2}} \tag{2.12}$$

which characterizes the distance over which ψ changes appreciably.

Using the Eq. (2.11), one can obtain the penetration depth $\lambda(T)$

$$\lambda(T) = \left(\frac{m^* c^2}{4\pi e^{*2} \psi_0^2}\right)^{1/2} \tag{2.13}$$

which characterizes the distance of penetration of the magnetic field into a superconducting region.

The dimensionless GL parameter is defined by the ratio of the penetration depth and coherence length

$$\kappa = \frac{\lambda}{\xi} \tag{2.14}$$

Since λ and ξ diverge in the same way at T_c, κ is approximately independent of temperature. The GL parameter distinguishes type-I ($\kappa \langle 1/\sqrt{2}$) and type-II ($\kappa \rangle 1/\sqrt{2}$) SCs. For type-I SC, the surface energy associated with a domain wall between normal and superconducting material in the intermediate state is positive.

In type-I SC materials, the applied magnetic field (H_{app}) is excluded from the material, if H_{app} is less than the critical field H_c. However, if $H_{app} > H_c$ the magnetic field enters the SC material and material loses its superconducting properties. For type-I SCs, the thermodynamic critical field, H_c, typically has values between 0.01 Tesla-0.1 Tesla at 0 Kelvin. Figure 2.1a shows the magnetic phase diagram of type-I SC. In type-II SC, the surface energy is negative and magnetic flux is excluded up to a lower critical field H_{c1}; above H_{c1} quantized vortices begin to enter to the SC material until we get to the stage in large applied fields where the cores of these vortices are very close together. The vortex cores begin to overlap strongly at the upper critical field, H_{c2}, and the material returns to its normal state, as seen in Fig. 2.1b. In the case of type-II SCs, the H_c values can exceed ~ 1 Tesla, with upper critical field values, H_{c2}, in the order of 20-40 Tesla at 0 Kelvin. In addition, for HTS materials that are strongly type-II SCs, the H_{c2} values exceed 100 Tesla at 0 Kelvin.

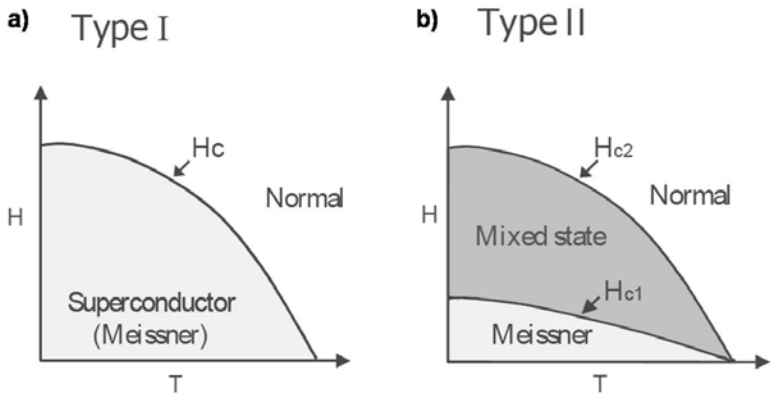

Figure 2.1: Magnetic phase diagrams for a type I (a) and a type II (b) superconductor.

2.2 Vortices in High Temperature Superconductors (HTSs)

High temperature superconductors are type-II materials. Due to their negative surface energy, type-II SC materials favor an arrangement with separate, individual flux lines in order to maximize the area between superconducting and normal domains. At the lower critical field H_{c1}, the magnetic field starts to penetrate continuously into the HTS material in the form of small normal filaments, or vortices. A single vortex, which carries a quantum of flux $\phi_0 = hc/2e = 2.07\times10^{-7}\,G.cm^2 = 2.07\times10^{-15}\,T.m^2$, has a normal core in which the superconducting parameter ψ goes to zero. The vortex core with radius on the scale of ξ is surrounded by supercurrents, as shown in Fig. 2.2. These currents create magnetic fields and thus the magnetic field has its maximum value at the center of the core.

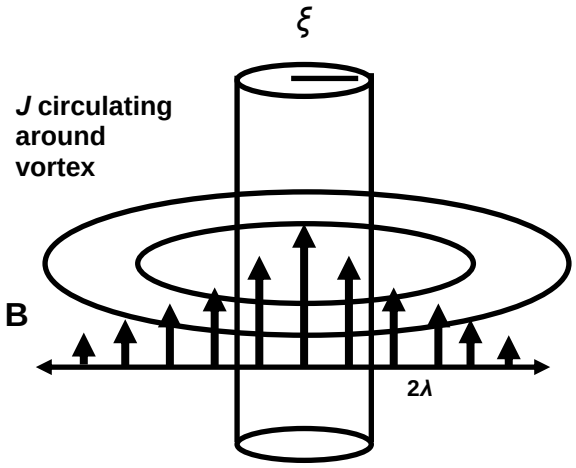

Figure 2.2: Structure of one vortex line in a type II SC. The vortex line is surrounded by supercurrent loops. The magnetic field **B** is the maximum at the center of the vortex line. Going outwards, **B** decreases with characteristic length λ.

This magnetic field decays approximately exponentially over a length scale of the penetration depth λ. Every vortex in the HTS material acts like a "bar magnet" due to the circulating supercurrent. These vortices repel each other because the supercurrents circulating about one vortex produce a repulsive Lorentz force, $\mathbf{F_L}$, on the magnetic field of another vortex.

$$\mathbf{F_L} = \mathbf{J} \times \mathbf{B} \tag{2.15}$$

Hence, vortices form a hexagonal array of flux tubes, known as the Abrikosov lattice [7]. These vortex lattices have been observed by using different techniques such as magnetic decoration [8], neutron scattering [9, 10], electron microscopy [11], electron holography [12], and Hall probe microscopy [13] and scanning tunneling microscopy (STM). In an external magnetic field, the Lorentz force on a current carrying superconductor tends to

move the vortex lattice perpendicular to the **J** and **B** as shown in the Fig. 2.3. If the flux lines move with velocity **v**, an electric field is generated

$$\mathbf{E} = -\mathbf{v} \times \mathbf{B} \tag{2.16}$$

The induced electric field has the same direction as the transport current, i.e., **E** is parallel to **J**. This movement of vortices causes a dissipative voltage, and power is dissipated in the material. The dissipated power density is given by $P = \mathbf{E} \cdot \mathbf{J}$. If the vortices can be immobilized or "pinned" by material defects or crystalline imperfections, a SC can sustain a high density current with little-to-no power loss. Defects and imperfections present energetically favored locations for vortices.

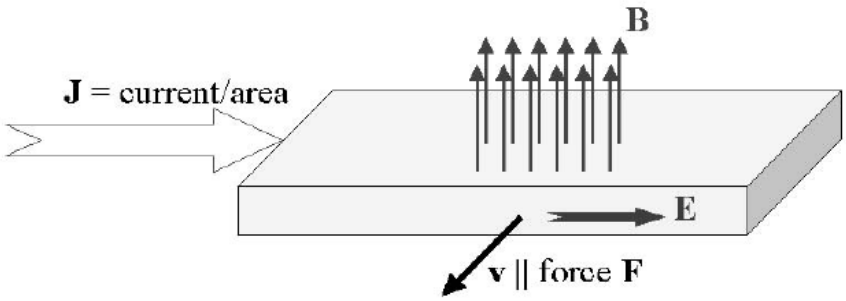

Figure 2.3. Schematic of vortex motion with velocity **v** in a magnetic field **B**, which produces an electric field, $\mathbf{E} = -\mathbf{v} \times \mathbf{B}$.

The pinned flux lines will remain stationary as long as the restraining force due to the pinning potential exceeds the effects of thermal activation and external transport currents. Possible pinning centers include impurities, voids, grain boundaries, dislocations, and oxygen vacancies in the structure of the cuprates. In addition to these pinning centers that occur naturally or intrinsically, there are also other methods to create pinning centers, such as irradiation of the material, addition of nanoparticles, etc. To have more effective pinning centers, the scale of the impurities should be comparable to the scale of ξ, the size of the normal vortex core. The pinning force on a vortex is the gradient of the pinning energy $F_{pinning} = -\frac{\Delta U_{pinning}}{\Delta x} \sim \frac{U_{pinning}}{\xi}$, since ξ is the shortest length scale in the problem. For an optimum pinning force, the defect size should be around the coherence length: a very small defect cannot fully "hold" the vortex core, while bigger non-superconducting pinning centers occupy too much of the useful superconducting matrix and may decrease the transition temperature, T_c

2.2.1 Magnetic Relaxation (Current Decay)

Magnetic relaxation is decay in time of the non-equilibrium magnetization in HTS materials, corresponding to a decay of macroscopic "critical" currents. For pinned flux lines at $T > 0$, there is a finite probability that the flux lines overcome the pinning barriers and hop to another pinning center, driven by the Lorentz force. This flux motion caused by thermal activation is called flux creep. Thermally activated flux motion is generally

stronger in HTS than in low temperature SCs. The reason is that the higher thermal energy, k_BT is more comparable with the pinning energy of flux lines.

Magnetic relaxation was first studied by Anderson-Kim [14, 15] in low temperature SCs. They assumed that there is a linear relation between J and pinning energy U, with $U \sim (J_{c0} - J)$. Unfortunately, the flux creep behavior of HTSs cannot be explained by the linear dependence of pinning energy $U_{eff}(J)$ on current density, due to the combination of strong vortex-vortex interactions and the large thermal energies k_BT made possible by the high T_c's, where k_B is the Boltzmann constant. Experimental results [16, 17] have shown that the relationship between U_{eff} and J is highly non-linear, in reasonable agreement with vortex-glass [18-21] and collective pinning [22] theories. These two theories give similar relationships, with inverse power-law type barrier energy,

$$U_{eff}(J) = U_o(T)\left[\left(\frac{J_{c0}}{J}\right)^{\mu} - 1\right] \tag{2.17}$$

Here U_0, which sets the scale of the energy barrier, is the pinning potential at $J = 0$ and J_{c0} is the current density at which $U_{eff}(J)$ goes to zero. According to the collective pinning theory, extensively reviewed by Blatter et al [23], Eq. (2.17) leads to an "interpolation formula" for the current density:

$$J(T,t) = \frac{J_{c0}}{\left[1 + \frac{\mu k_B T}{U_0}\ln\left(\frac{t}{t_0}\right)\right]^{\frac{1}{\mu}}} \tag{2.18}$$

where t_o is a characteristic attempt time for hopping. The same interpolation formula was derived using the vortex-glass theory [18-21]. The values of the characteristic exponent μ depend on the different creep regimes, as determined by a competition between different energy, current density, and length scales in the complex system of vortices and pinning centers. According to the vortex-glass theory, μ is ≤ 1, while collective pinning predicts different μ values depending on field and temperature. In collective pinning theory for weak, point-like defects, μ=1/7 for low field and low temperature region where creep is dominated by individual flux lines. At high fields and temperatures, μ becomes 3/2 in a region where small bundles of flux lines move. At still higher fields and temperatures, μ decreases to a value of 7/9 as the bundle size of flux lines gets still larger. The normalized relaxation rate (or creep rate) is defined by

$$S = -\frac{1}{M}\frac{dM}{d\ln(t)} = -\frac{d\ln(M)}{d\ln(t)} = -\frac{d\ln(J)}{d\ln(t)} \tag{2.19}$$

Utilizing Eq. (2.18), Eq. (2.19) leads to

$$S = \frac{k_B T}{U_0 + \mu k_B T \ln\left(\frac{t}{t_0}\right)} \tag{2.20}$$

From this expression, the creep rate S increases linearly with low temperatures where the additive term U_0 dominates over the T-dependent term. At higher temperatures, however, where $k_B T > U_o$ the creep rate saturates and S is given as follows:

$$S = \frac{1}{\mu \ln\left(\frac{t}{t_0}\right)} \tag{2.21}$$

2.2.2 Relation between Electric Field-Current Density

As explained in the section 2.2 Vortices in HTSs, when vortices are forced to move, an electric field *E* is induced in the media. Apparently, there will be power dissipation related to the *E* field. The power dissipation becomes more detrimental to the material applications at high temperatures and in large applied magnetic fields. Therefore, it is necessary to investigate the *E-J* characteristics in a wide range of electric fields and temperatures to obtain much more detail about the HTS material in the mixed state in which HTS devices may operate. Recently, we have combined several experimental methods, transport, swept field magnetometry, and flux creep, to obtain *E-J* characteristics over a very wide range of dissipation for several different samples.

For conventional four-probe transport measurements, typical *E* field levels are 1 μV/cm, which is the usual transport criterion for defining the critical current density. In transport studies, the *E* field is typically higher than that obtained by magnetic measurements. Of course, higher *E* fields also generate more energy dissipation. Transport measurements have several advantages, including conceptual simplicity, clarity of the end-to-end current path, and a well-defined orientation relative to a tilted magnetic field in angular studies.

On the other hand, magnetic measurements have certain complementary advantages over transport measurements. The dissipation level tends to be self-limiting, thereby precluding the hazard of “burning out” or destroying a valuable sample.

Transport measurements are often restricted to higher temperatures and lower currents, due to heating of electrical contacts. However, with magnetic measurements, one is able to go to lower temperatures where the current density can be very high. The *E-J* characteristics of a regularly shaped sample can be obtained via Vibrating Sample Magnetometry (VSM) and Superconducting Quantum Interference Device (SQUID) magnetometry measurements. In VSM method, the applied magnetic field is swept at a controlled rate, which induces an average electric field *E* at the perimeter of the square sample with side *a*, as given by

$$E = \frac{d\phi / dt}{perimeter} = \frac{a}{4}\left(\frac{dB}{dt}\right) \tag{2.22}$$

Typically, the field sweep generates $E \sim 10^{-7}$-10^{-9} V/cm in our studies.

In SQUID magnetometry-based creep measurements, the electric field is proportional to the current decay rate *dJ/dt*. The magnetization of a SC disk with radius *R* and thickness *d*, subjected to a fixed applied magnetic field (that does not change with time) is given in the Bean critical state model by

$$M = \frac{m}{V} = \frac{R.J_c}{3} \tag{2.23}$$

Here *m* is the magnetic moment, *V* is volume of the SC disk, and J_c is the maximum current circulating around the disk. The magnetic flux of the disk is approximately

$$\phi = Area.B = \pi R^2.\mu_0\left(H_{eff} + M\right) \tag{2.24}$$

Here H_{eff}=H_{app}-*DM* , which is substituted into Eq. (2.24) to give

$$\phi = Area.B = \pi R^2.\mu_0\left[H_{app} + (1-D)M\right] \tag{2.25}$$

where *D* is the demagnetization factor.

The induced electric field on the perimeter of the SC disk is

$$E = \frac{d\phi / dt}{perimeter} = \frac{\mu_0 R}{2}(1 - D)(\frac{dM}{dt}) \tag{2.26}$$

where (dH_{app}/dt)=0 since the applied field does not vary with time. Recalling Eq. (2.23) and substituting into Eq. (2.26), one obtains

$$E = \frac{d\phi / dt}{perimeter} = \frac{\mu_0 R^2}{6}(1 - D)(\frac{dJ_c}{dt}) \tag{2.27}$$

where $(1 - D) \approx \frac{d}{R}$. Finally, the induced E field becomes

$$E = \frac{\mu_0 R d}{6}(\frac{dJ_c}{dt}) \tag{2.28}$$

In the case of a SC square sample, $R=a/2$, the induced E field on the sample on perimeter is given by,

$$E(J) = \frac{\pi . a}{12} d\left(\frac{dJ}{dt}\right) \tag{2.29}$$

Here d is the HTS thickness and a is the width. This contactless method allows us to reach electric fields in the range of 10^{-10}-10^{-13} V/cm.

2.3 The Modified Bean Critical State Model

The critical state model assumes that the current density circulating in the superconductor (SC) flows with a density equals to the critical current density J_c that in general depends on both r and H. According to Bean critical state model [24, 25], the spatial variation of J_c is constant and given in 1D by the Maxwell relation, $J_c=dH/dx$

within the superconductor sample. The critical current density J_c (current per cross-sectional area, A/cm^2) is the maximum current density which can be sustained by a SC before significant dissipation occurs. There are different methods are used to calculate J_c in a SC. During our study, we use magnetic measurements to obtain J_c. As is well known in electrodynamics, a circulating current generates a magnetic dipole moment given by

$$\mathbf{m} = \frac{1}{2}\int (\mathbf{r} \times \mathbf{J}(\mathbf{r}))dV \tag{2.30}$$

where **J** is the current density at location **r**. The hysteresis of magnetic moment (magnetization) curves as shown in Fig. 2.4 is used to determine J_c values with the help of the critical state model, first introduced by Bean [24, 25]. This model is based on two assumptions: *i*) the supercurrent density is given by J_c and *ii*) any changes in the flux distribution are introduced on the surface of the sample. In essence, the critical state model provides that $J_c(H,T)$ is proportional to $\Delta M = \left(M^- - M^+\right)$, where M^- and M^+ are the magnetization at the same temperature T and same field H, measured in decreasing and increasing field history, respectively. Values for J_c of a rectangular sample with field perpendicular to a face with sides $b>a$ are obtained by the "sandpile" model (in SI units) [26].

$$J_c = \frac{2\Delta M}{a(1 - a/3b)} \tag{2.31}$$

In the creep measurements, the current density of the sample at any given time was obtained using the "sandpile" critical state model for a rectangular SC with sides $b>a$, the current density (in SI units) is given by

$$J(t) = \frac{4M(t)}{a(1-a/3b)} \tag{2.32}$$

where M (t) is the irreversible component of the magnetization.

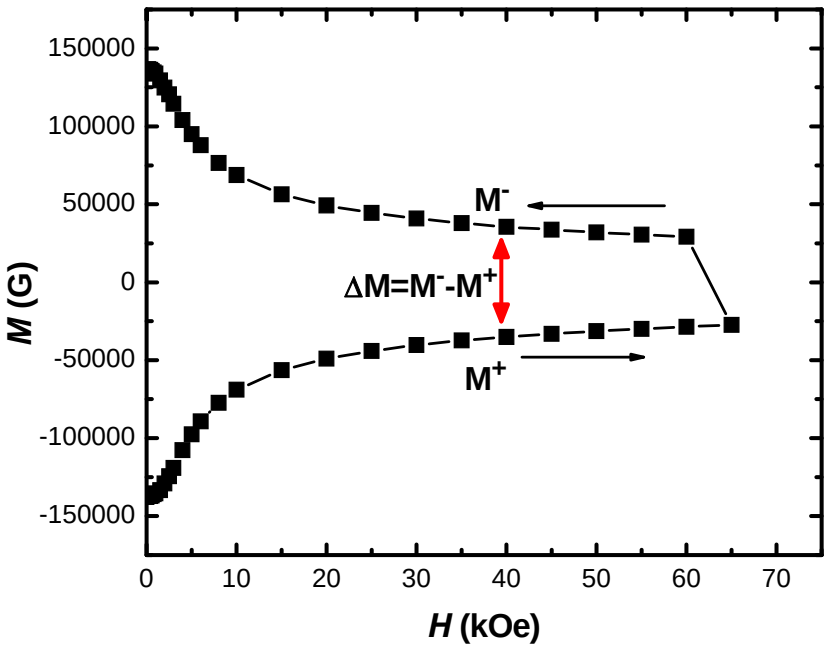

Figure 2.4. The *M-H* loop data exhibiting the hysteresis in the magnetization curve of a 3 μm thick (SmY)BCO film at 10 K.

Chapter 3

Developments in Coated Conductors

In this chapter, we will review the developments in the coated conductors. Fabrication methods for biaxially textured metallic substrates, including Inclined Substrate Deposition (ISD), Rolling Assisted Biaxially Textured Substrates (RABiTS), and Ion Beam Assisted Deposition (IBAD), will be discussed. Next, epitaxial thin film formation concepts will be discussed in detail. Afterwards, we will focus on the properties of buffer layers and their deposition techniques. Finally, general issues associated with the IBAD method will be reviewed.

3.1 Coated Conductors

After discovery of high temperature superconductivity (HTS), enormous efforts have been made in coated conductor (CC) development to manufacture affordable flexible wires with high current density, *J*. The first generation Bi-based HTS wires have had limited impact on industrial applications, due to their high-cost and low current carrying capability in the presence of moderate magnetic fields (<1 Tesla) at liquid nitrogen temperatures. Hence, much effort is now concentrated on the development of $YBa_2Cu_3O_{7-\delta}$ (YBCO)-based second generation coated conductors, since they are less expensive compared to Bi-based HTS wires and can support high *J* in applications

requiring substantial magnetic fields [27]. Initially, the development of CCs based on YBCO materials was limited due to vortex and weak link effects. The weak vortex pinning issue can be overcome by choice of material which have strong flux pinning capability at high temperatures and magnetic fields. Although HTSs have a lot of natural pinning centers such as oxygen vacancies, grain boundaries, voids, misfit dislocations, planar defects, it has been shown that artificial pinning centers are much more effective to enhance J_c of the material. Therefore, extensive investigations have been devoted in developing artificial pinning centers in HTS matrix. So far, different methods have been used to introduce these nanoscale defects, e.g., introducing nonsuperconducting nanoparticles like $BaZrO_3$ [28, 29], Y_2O_3 [30], Y_2BaCuO_5 [31], $BaSnO_3$ [32] in the $YBa_2Cu_3O_{7-\delta}$ (YBCO) matrix, doping with rare-earth elements [33-37], and substrate surface decoration [38-40]. The other significant issue is the problem of weak links that reduce the overall current conduction between grains and the associated J_c values, although the current transport within individual grains can be very high. It has been shown that uniaxially aligned HTS films, whose *c*-axis is perpendicular to the substrate, can be easily deposited on the polycrystalline substrates. However, the superconducting properties of those films are degraded at the grain boundaries due to the disorientation of *a* and *b*-axis. High superconducting performance can be obtained by aligning both *c*-axis and *a*-*b* basal planes of all grains, forming a biaxially aligned structure. It is well established that the substrate has a strong influence on the microstructure and electrical properties of HTS coating. Therefore, in order to have high current conduction, the SC must have a biaxially textured template.

3.2 Fabrication Methods for Biaxially Textured Metallic Substrates

Nowadays, HTS films are deposited on flexible biaxially textured metallic substrates using different deposition techniques to obtain well textured substrates and superconducting layers. These techniques are Inclined Substrate Deposition (ISD) [41, 42], Rolling Assisted Biaxially Textured Substrates (RABiTS) [43-45], and Ion Beam Assisted Deposition (IBAD) [46, 47]. Following is some background information about these techniques.

3.2.1 Inclined Substrate Deposition

It has been shown that biaxially textured yttria stabilized zirconia (YSZ) and MgO buffer layers can be grown on the flexible Hastelloy C276, Ni alloy substrate by electron beam (e-beam) or pulsed laser deposition (PLD) methods [48, 49]. In ISD method, the substrate is inclined by an angle β with respect to deposition target. This orientation between target and substrate gives a preferred orientation to the grown film. On the other hand, due to this geometry, the c-axis orientation of the film is also tilted towards the deposition direction. Therefore, the tilt in the c-axis adversely affects the performance of HTS film. To date, there are no reports that the critical current densities of YBCO films on the ISD buffer tape excess 1 MA/cm^2, at 77 K and self-field. Moreover, the inclination angle affects the texture of the film. The combination of these issues makes this technique less attractive.

3.2.2 Rolling-Assisted Biaxially Textured Substrates (RABiTS)

Another method to obtain biaxially textured substrate is RABiTS. It was shown by a team of scientists from ORNL [50-52] that long length and biaxially textured Ni and Ni-alloy substrates can be obtained by rolling and annealing processes. In the RABITS process, the textured metallic substrate provides a good template for subsequent deposition of buffer layers before the superconducting film is deposited. These buffer layers prevent chemical reactions between superconducting film and Ni/Ni-alloy substrate. More details about properties of buffer layers will be given in the "buffer layer" section. The RABiTS coated conductor architecture contains the standard buffer layer sequence of CeO_2/YSZ/Y_2O_3/Ni, or CeO_2/YSZ/CeO_2. Recently, $La_2Zr_2O_7$ (LZO) deposited with chemical solutions has also been used an optional cap layer. It has been shown that the high quality YBCO films with high J_c values exceeding 2 MA/cm^2 at 77 K are grown successfully on the RABiTS architecture

3.2.3 Ion Beam Assisted Deposition (IBAD)

In the Ion Beam Assisted Deposition (IBAD) method, buffer layers of YSZ [53], gadolinium zirconate $Gd_2Zr_2O_7$, (GZO) [54] or MgO [55] are grown in a vacuum system on an Y_2O_3/Al_2O_3/Hastelloy template. For commercial applications, MgO [55] is preferred as an IBAD template since it can function effectively in a much thinner layer than other previously developed high quality IBAD templates, such as YSZ [53] and GZO [54].

During the buffer layer deposition, an argon (Ar) ion beam directed at an angle to the substrate surface simultaneously bombards the film and thereby produces a biaxially textured buffer layer. After that YSZ, GZO or MgO is deposited, and it is ready to serve as a IBAD-template for the growth of subsequent buffer layers. Once a textured surface has been obtained, a HTS REBCO layer can be grown on top using different processing techniques, such as PLD or metal-organic chemical vapor deposition (MOCVD). The present, standard IBAD (MgO) template [56] has five buffer layers between a polycrystalline Hastelloy (a Ni-based alloy) substrate and the HTS coating (Fig. 3.1). The first layer is 80 nm thick Al_2O_3 and serves as a barrier to prevent upward diffusion of substrate cations. The superior diffusion barrier properties of Al_2O_3 for transition metals such as Ni, Cr, Mn, Mo, etc., as well as for oxygen are well established [57]. The second buffer is a 7 nm thick Y_2O_3 seed layer to facilitate the IBAD-MgO nucleation [58]. The third one is IBAD-MgO, which requires only 10 nm thickness to form the optimal biaxial texture [59, 60]. These three layers are deposited by radio frequency (*rf*) or direct current (*dc*) magnetron sputtering techniques at ambient temperature. In particular, this low temperature process ensures Al_2O_3 to be amorphous or nanocrystalline [57], which acts as better diffusion barrier than polycrystalline counterpart of equivalent thickness. Moreover, the low diffusion coefficient of oxygen in MgO (~ 10^{-22} cm^2/s at 800^oC) [61, 62] as well as its structural, chemical, and thermodynamic stability makes MgO a robust buffer layer component, suitable for subsequent buffer and YBCO depositions at high temperatures (~ 800^oC) and oxygen partial pressures. The fourth layer is a 20 nm thickness of reactively sputtered homo-epitaxial MgO [63], which ensures structural

robustness of IBAD-MgO by further improving the texture and restoring the surface lattice constant to that of the bulk MgO (0.421 nm) [57]. Note that the measured lattice constant of the as-deposited IBAD-MgO varies between 0.43-0.44 nm [57]. The IBAD architecture is completed by a $LaMnO_3$ (LMO) cap layer that provides a structurally and chemically compatible template for the subsequent growth of high quality YBCO coatings [58, 64, 65].

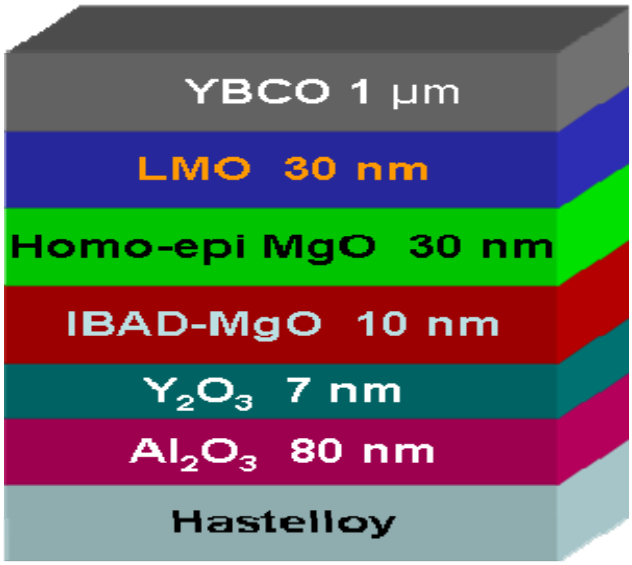

Figure 3.1. The present Ion Beam Assisted Deposition (IBAD) buffer architecture.

3.3 Epitaxial Thin Films

Epitaxy refers to formation of a single crystal film on a single crystal substrate. Epitaxy can be grouped into two types: homoepitaxy and heteroepitaxy. Homoepitaxy is the state when both the film and substrate are of the same materials. On the other hand, heteroepitaxy is related to the situation when film and substrate are of dissimilar materials. From applications point of view, heteroepitaxy is the most general form of epitaxy in various technological applications such as semiconductors, superconducting devices, and optoelectronic devices. The lattice parameter difference between the film and the substrate plays a crucial role on the epitaxial film growth. In homoepitaxy, there is little-to-no lattice strain at the film-substrate interface, because both film and substrate are made of the same materials. In the case of heteroepitaxy, there is lattice mismatch between the film and substrate and hence, the interface is strained or relaxed depending on the magnitude of the difference. This also results in an interface energy, γ_I, which consists of two terms: interface energy due to the formation of a new interface and elastic strain energy because of the lattice mismatch between the film and substrate. The lattice mismatch f is given by

$$f = \frac{a_f - a_s}{a_s} \tag{3.1}$$

where a_f and a_s are the lattice parameters of the film and substrate, respectively.

The growth in the thin film structure can be classified into three modes: two-dimensional (2 D) layer-by-layer growth (Frank-Van der Merwe Growth), 3 D crystallite formation

(Volmer-Weber Growth), and 2 D growth followed by 3 D crystallite formation (Stranski-Krastanov).

Layer by Layer (Frank-Van der Merwe) Growth:

In this growth mode, an initial set of atoms forms a monolayer, and then clusters are developed on the first layer to form the film. The Frank-Van der Merwe (FM) growth mode is shown in Fig. 3.2a. In this growth mode, if the sum of the surface free energy, γ_s and the interface free energy, γ_I, is lower than the free energy of the substrate surface energy, γ_F, it is energetically favorable for the epitaxial layer to completely cover the surface. In this case,

$$\gamma_F + \gamma_I \leq \gamma_S \tag{3.2}$$

For homoepitaxial growth where the deposited film and substrate are made of the same materials, γ_I=0 and $\gamma_F = \gamma_S$, and the above equation is satisfied. For heteroepitaxial growth, the film surface energy γ_F, should be less than the substrate energy and low misfit (i.e., low γ_I) is desired. The elastic strain energy is also taken account since it increases as the number of monolayers increases.

3 D or Island Growth [Volmer-Weber, (VM)] Growth:

In the VW growth mode, individual cluster-like islands are developed. This type of growth is illustrated in Fig. 3.2b. The VW growth occurs when the sum of the interface and surface energies is higher than the substrate energy,

$$\gamma_F + \gamma_I > \gamma_S \tag{3.3}$$

In this mode, adatom-adatom interactions are stronger than those of the adatom with surface, leading to formation of 3 D adatom clusters or islands. However, these 3 D islands coalesce to form a continuous film at longer growth times. During the island nucleation on the substrate surface, atoms or ions give their energies partly or completely to the substrate. Thus, these atoms are adsorbed by the substrate. Adsorbed atoms (adatoms) are bound with the surface by the covalent or Van der Waals forces. If adatoms have enough kinetic energies to overcome those forces, they will diffuse or be desorbed from the surface and return to the gas phase. The diffused atoms will be pinned by the surface defects such as step edges and grain boundary dislocations. The bound atoms themselves behave like the attractive sites for other diffusing atoms. Island growth continues until the islands come together and unite to form continuous film.

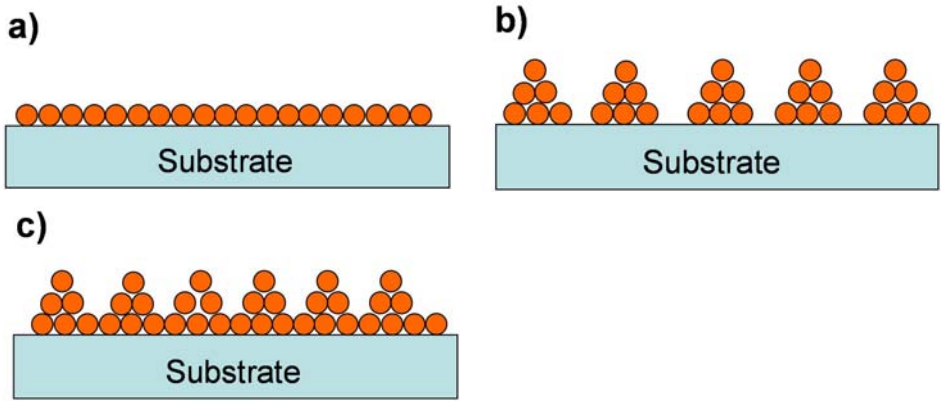

Figure 3.2 The main epitaxial growth modes: a) Layer by Layer (Frank-Van de Merwe); b) Island (Volmer-Weber); c) Stranski-Krastanov

Stranski-Krastanov (SK) Growth Mode:

The SK growth mode combines the 3 D and 2 D growth modes as exhibited in Fig. 3.2c. In this mode, the growth changes from monolayer to island after few monolayers. Because of the lattice mismatch between film and substrate, strain accumulates in the 2 D film and in order to relieve the induced strain, 3 D islands are developed. In other words, the induced strain switches the growth mode from 2 D to 3 D islands. This transition from layer to island based growth occurs at a critical layer thickness that is affected by the chemical and physical properties, such as surface energies and lattice parameters of the grown film and substrate.

3.4 Buffer Layers

There are serious challenges for the synthesis of high quality HTS films on biaxially textured substrates. These challenges can be defeated through good choices of buffer layers. The most significant task of the buffer layer is that it must not react with superconducting film and prevent chemical reactions that could take place between substrate template and superconducting film. Moreover, the substrate should be flexible and available in long length for commercial applications. In addition, the substrate should also provide mechanical support and crystallographic template for the buffer layers. As a matter of fact, it has been shown by many experiments that the quality of superconducting film is strongly affected by the choice of substrate and buffer layer materials.

In addition to properties mentioned above, there are other significant requirements that need to be fulfilled by buffer layers. Buffer layers must possess suitable crystalline orientation, structure and closely match the lattice parameter of the superconducting film. Furthermore, in order to act as an effective barrier, it is desirable that the buffer has a close thermal expansion coefficient with superconducting film and substrate. Significant differences in thermal expansion coefficient could lead to crack formation in buffer layers, which in turn leads to deterioration of the HTS coating performance. Different fabrication processes are used for buffer layer deposition, such as electron beam evaporation (e-beam), pulsed laser deposition (PLD), *rf*- and *dc*-magnetron sputtering.

3.5 Deposition Methods for Buffer Layers

The application of thin film technology has made a significant impact on the different research areas such as electronics, material science, biological research, and physics. The demands for new and improved semiconductor devices have stimulated the research and new thin film deposition techniques. The deposition methods play crucial role in the thin film synthesis. In addition, thin film properties are strongly affected by various deposition parameters, including temperature, pressure, gas ambient, and rate. In the following subsection, the most commonly used deposition methods, i.e., electron beam evaporation (e-beam), pulsed laser deposition (PLD), and magnetron sputtering will be discussed.

3.5.1 Electron Beam Evaporation

In the evaporation process, a source material is heated until it evaporates. Temperatures could reach to 3000^{o}C during this process. Then, the evaporated atoms condense on the substrates surface, which is kept at a lower temperature. All process takes place in pressures $\leq 10^{-5}$ Torr, which allows the molecules to evaporate freely and impinge onto the substrate's surface. In this technique, an electron beam is employed to heat the target and result in evaporation. Electrons are generated from filaments such as tungsten placed inside the electron beam gun. When the filament becomes enough hot, it emits electrons, these electrons are focused onto the source material by using magnetic lenses. When the electron beam strikes the source surface, kinetic energy of electron beam is transformed into thermal energy (heat). Due to this generated heat, the evaporation takes place. During deposition, the target holder is water cooled to avoid melting the crucibles. Even though e-beam evaporation is a very common deposition technique, it is an expensive method in terms of industrial applications. There are also other issues, such as maintaining integrity of electron source and controlling the stoichiometric composition of grown film.

3.5.2 Pulsed Laser Deposition (PLD)

Pulsed laser deposition (PLD) is one of the simplest and most reliable deposition techniques compared to other evaporation methods. In this method, a laser beam is employed to vaporize the target material placed in a vacuum chamber. When a laser beam hits the target, material is ejected from the surface, which is called an ablation

plume. The plume contains plasma, micro size particulate components and deposition gas. Afterwards, the flux of material condenses on the substrate surface and thin film formation takes place. In the literature, numerous papers can be found related to thin films deposited by PLD method. PLD has its own advantages over the other evaporation techniques. For example, it enables the creation of new materials, such as growth of complex oxides or nitrides. There are several serious obstacles for industrial applications of PLD, however. The important limitations of this method are ejection of micro size particulates, which could badly affect film structure, and issues associated with scale-up processes since this technique is ideal for small scale applications. One major drawback for large-scale applications of PLD is that the cost and maintenance of the laser system is very high. All these disadvantages make the PLD method unattractive for large scale applications.

3.5.3 rf- and dc-Magnetron Sputtering

Sputter deposition is one of the most commonly used techniques for thin film growth. The sputtering process shown in Fig. 3.3 is based on the momentum transfer from accelerated energetic ions to the atoms on the surface of a target. The incident ions cause a collision chain reaction in the target. This reaction has two important results: First, if the atoms gain high enough energy to break the surface binding energy, they can be ejected, i.e., sputtered away from the target surface. Second, an important consequence of the collision reaction is that the transferred energy from the ion will result in the

emission of secondary electrons which stimulates the ionization efficiency from the target.

In addition to the secondary electrons, magnets are also utilized to improve the ionization efficiency. Magnetic fields trap electrons close to the surface of the magnetron. Magnetic fields perpendicular to the surface of the cathode force electrons to follow spiral paths around the magnetic field lines.

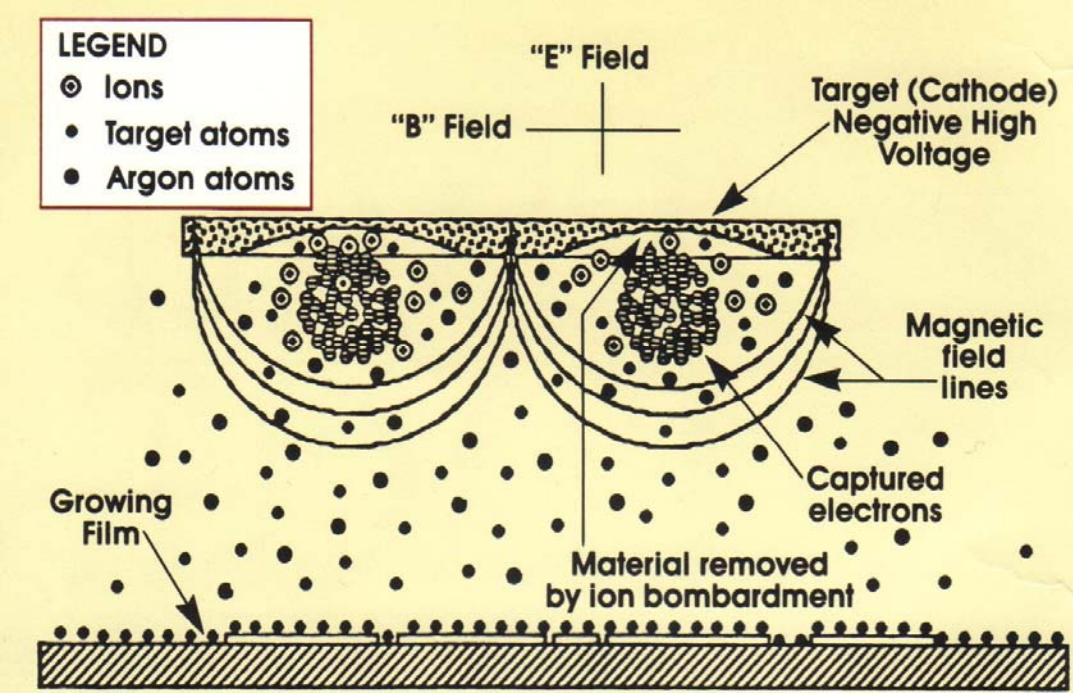

Figure 3.3. Cross section view of planar magnetron.

This produces more ionizing collisions with gas atoms near the cathode. Typically, the sputter gas is inert, i.e., Ar. These collisions increase the density of Ar^+ ions which in turn results in a higher deposition rate. The sputtered atoms are mostly neutral, so they are not affected by the magnetic trap. Charge build-up during Ar^+ ion bombardment can be avoided during the *rf* sputtering in which the sign of the anode-cathode bias is varied at a high rate. For production of highly insulating oxide films, *rf* sputtering works well. Compared with other deposition techniques advantages of sputter deposition are as follows:

- Materials with a high melting point (and low vapor pressure) are easily sputtered
- Deposited films have a composition close to that of the target material
- Films have better adhesion on the substrate
- Sputtering sources generally do not contain hot regions because they are water cooled

Some disadvantages of the sputtering process are:

- Many deposition parameters makes the sputter deposition a complex process
- It is difficult to control where the atoms go, which in turn causes contamination problems.

3.6 General Issues in IBAD Method for Coated Conductor Development

The IBAD method is one of the most common deposition technique used for obtaining textured substrates. Moreover, it does not depend on the choice of substrate

material. Nonetheless, there are several issues need to be overcome for further development and improvement of IBAD-based coated conductors for large scale-up applications. Although the IBAD process is a fast process, it requires a smooth substrate surface, which is achieved via electropolishing the substrate. Yet it is clear that polishing a kilometer long tape is not a convenient method in terms of commercialization of HTS. So there is a need to develop an alternative new method that should provide the same results or even better than electropolishing does. Moreover, it should be cost effective for industrial applications. Another significant issue with IBAD-based coated conductors is that the presence of large number of buffer layers between the cap layer (the top most layer) and Ni-based alloy substrate. The commercially available IBAD architecture consists of LMO/homo-epi MgO/IBAD-MgO/Y_2O_3/Al_2O_3/Hastelloy. Obviously, it is desirable to minimize the number of buffer layers to reduce the overall process complexity and the manufacturing cost. We have addressed this issue in chapter 6. Different research groups have been working to solve these IBAD issues to simplify and reduce the overall process complexity.

Chapter 4

Experimental Methods

In this chapter, we will first discuss the details of material synthesis and developments in three significant steps: deposition of buffer layers, annealing process and growth of YBCO thin films. The second section focuses mainly on the how magnetic measurements were performed and critical currents of REBCO thin films were determined. Finally, we will describe the experimental equipment employed during measurements.

4.1 Material Synthesis and Development

4.1.1 Deposition of Buffer Layers

In the study of buffer layer growth, an *rf* magnetron sputter system was used to deposit standard LMO buffer layers on the IBAD-MgO and on homo-epi MgO templates as well. To ensure consistency, short samples of both templates were cut from two respective batches of long length tapes. The thickness of $LaMnO_3$ (LMO) films was varied from 30 to 240 nm to investigate its effect on the YBCO properties. The sputter target was made from single phase stoichiometric LMO powder, prepared by solid state reaction, which was packed into a two inch copper tray. To optimize the processing parameters of LMO, both temperature and sputter gas compositions were varied. Typical

sputtering conditions consisted of 5-8 mTorr total pressure of only forming gas (Ar-4%H_2), or mixtures of Ar-4%H_2 and water vapor (H_2O), or Ar-4%H_2 and O_2. The LMO films were deposited at substrate temperatures in the range 500-750^oC. The IBAD-MgO templates (with and without homo-epi MgO) used in this study were fabricated by SuperPower, Inc.

After having demonstrated deposition of standard LMO films directly on the IBAD-MgO templates, we have further functionalized the standard LMO cap layers by replacing it with the composite LMO:MgO layer. The composite cap layers were deposited also by employing *rf*-magnetron sputtering system on both IBAD-MgO and homo-epi MgO templates. The sputter target was made from stoichiometric LMO powder, prepared by solid state reaction, which was mixed with MgO powder and packed into a two inch copper tray. The added volume percentage (vol. %) of MgO was varied from 5% up to 75%. The sputtering gas ambient was forming gas (Ar-4% H_2) mixed with O_2, at a total pressure 5-7 mTorr. The substrate temperature was varied from 720^oC up to 750^oC. Prior to deposition of buffer layers, substrates were annealed in-situ at the deposition temperature for 30 minutes to 45 minutes to remove adsorbed H_2O and hydrocarbons.

4.1.2 Annealing Process

For post-annealing process, the furnace was heated up from room temperature to 750^oC in flowing Ar gas at 1 atm. After that epitaxial composite LMO:MgO films were

placed into the crucible and kept at the middle of the furnace for 2 hours. After this heat treatment, the samples were cooled to room temperature.

4.1.3 Deposition of YBCO Thin Films

YBCO films were grown on LMO buffered simplified and standard IBAD architectures by PLD method using a KrF excimer laser system operated at an energy density of ~ 2 J/cm^2 and a repetition rate of 10 Hz. During this deposition, the substrates were maintained at 780^{o}C in 120 mTorr of O_2. Typical YBCO film thicknesses were in the range of 0.8-1 μm. On the other hand, for composite LMO:MgO buffered IBAD architectures, YBCO films of 0.8 μm thickness were deposited by PLD at temperature 790^{o}C in 300 mTorr of O_2 gas pressure.

After deposition, the samples were first cooled to 500^{o}C at a rate of 30^{o}C/min; then the O_2 pressure was increased in the chamber to 400 Torr, and the samples were cooled to room temperature at the same (30^{o}C/min) rate. This was followed by deposition of silver, Ag, on the YBCO films to make good low resistance electrical contact, which is a significant step in measuring the critical current. In order to optimize the oxygen content, YBCO coated samples were ex situ post-annealed in the furnace in flowing pure O_2 gas at 1 atm. The furnace temperature was increased at a rate of 10^{o}C/min up to 500^{o}C and the samples were maintained for 1 hour. Afterward, the temperature was decreased at a rate of 2^{o}C/min to 300^{o}C, and then the samples were furnace cooled to room temperature.

4.2 Physical Characterization of the Films

4.2.1 X-Ray Diffraction

The crystalline structure of a material can be determined by X-ray diffraction, since the interatomic spacing in crystals is of the order of the wavelength of X-ray radiation, a few angstroms, (1Å=10^{-8} cm). X-rays reflected by crystal planes give constructive or destructive interference, depending on the Bragg condition. The situation is illustrated in Fig. 4.1, where the crystal planes make an angle θ with the incident X-ray and the detector is placed at angle 2θ. Constructive interference occurs when the difference in the path length is an integer multiple of the X-ray wave length. This leads to Bragg's law:

$$2d\sin\theta = n\lambda \tag{4.1}$$

where d is the interplane spacing, λ is the wave length of the X-ray, and n is an integer. Crystals have their own interplane spacing, resulting in different diffraction angles. (Diffraction angles vary with interplane spacing of the crystals.) Hence, the X-ray diffraction gives essential information about the alignment of the film material. There can be deviations from the ideal reflection angle due to internal stress or changes in the film stoichiometry. The misalignment of individual crystallites in the film can be determined by recording rocking curves, or ω-scan of the sample. In an ω-scan, the position of the detector and x-ray beam is fixed for 2θ angle of the relevant Miller indices $\{hkl\}$ reflections.

Then, the sample is gradually rotated about an axis in the plane of the film, to detect the reflections from planes which have the same Miller indices. In other words, an ω-scan gives the degree of preferred orientation in the film. The full width at half maximum (FWHM) values are used to quantify the quality of the films. In order to determine the in-plane epitaxial quality of a film, a ϕ-scan is employed. In a ϕ-scan, the incoming angle θ and Bragg angle 2θ are chosen for a plane which is not parallel to the sample surface. The sample is rotated around its normal axis, giving a ϕ-scan. Examples will be shown in chapter 6.

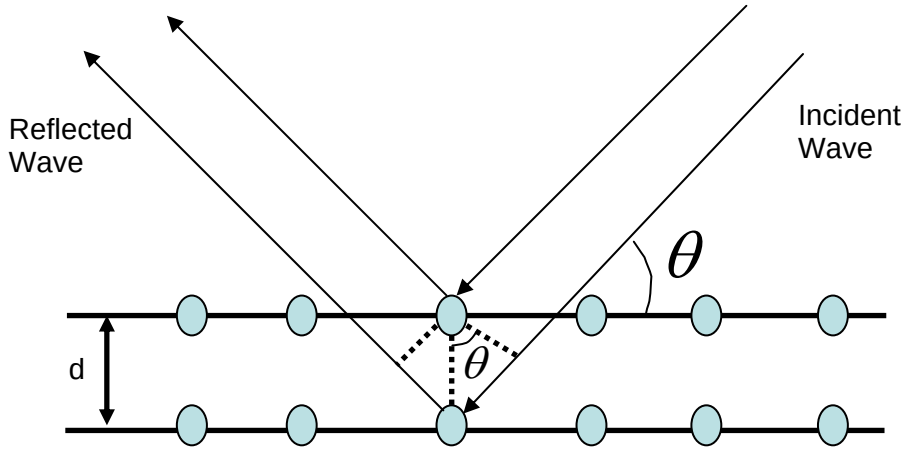

Figure 4.1. Reflection of X-rays by a set of crystal planes separated by a distance *d*.

4.2.2 Scanning Electron Microscopy (SEM)

So as to have information about the sample surface morphology, SEM is used. SEM utilizes high-energy beam of electrons to scan the sample surface. During the scanning process, the electrons interact with the sample and electrons lose part of their energy. The energy exchange between the electron beam and sample yields the reflected high-energy electrons, secondary electrons and electromagnetic radiation. These signals require specialized detectors for their detection.

The SEM consists of three different parts:

- Vacuum system
- Source and lenses
- Detectors and electronic devices

The vacuum system provides a clean and stable environment for electron emission from electron gun.

The electron beam exiting from the electron gun is focused by condenser lenses, which transmit the beam towards the final lens sitting just above the specimen. The final lens determines the shape and the size of the electron beam by employing pairs of scanning coils. In the main chamber, there are detectors that collect the signals produced by the electron beam-sample interactions. Each detector is specialized for its own signal. Different types of electronic amplifiers are used to amplify the weak signals and counting electronics measure the signal. Next the signal is sent to the display screen where the intensity of a pixel shows the strength of signal measured at the corresponding point.

4.2.3 Atomic Force Microscopy (AFM)

The atomic force microscope (AFM), one of the leading tools for surface imaging, is a very high-resolution type of scanning probe microscope. A Digital Instruments Nanoscope III was employed in contact mode to assess the surface morphology of the films. The AFM exhibited in Fig. 4.2 consists of an atomically sharp tip that is attached to a microscale cantilever. The cantilever tips are usually made of silicon, Si, or silicon nitride, Si_3N_4, and the tip radius is of the order of nanometers. The cantilever deforms under repulsive interaction forces between the surface and tip, when it is brought near the sample surface. The deflection of the cantilever, which obeys Hooke's law $F=k.x$ where x is the deflection of the cantilever from its equilibrium position, is measured by using a laser beam reflected from the top of the cantilever into a 2 D photodiode array and compared to the equilibrium value.

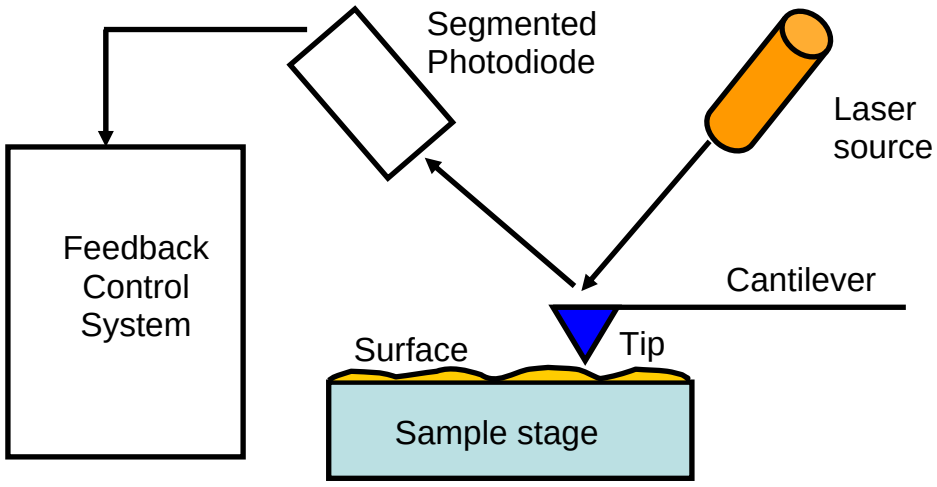

Figure 4.2. Schematic representation of a typical AFM

There are several different imaging modes, which can be used to characterize the surface of the specimen using the AFM. In contact mode, the force between the surface and the tip is kept constant during scanning by maintaining a constant deflection. In the tapping mode, the cantilever oscillates up and down near its resonance frequency. The interaction forces acting on the cantilever when the tip is close to the surface causes a decrease in the amplitude of the oscillation as the tip gets closer to the surface. The drop in the oscillation amplitude is used for the feedback. Unlike the contact mode, in the tapping mode the tip does not touch to the specimen surface. The tapping mode enables study of soft and biological samples.

4.2.4 Auger Electron Microscopy

Auger electron spectroscopy (AES) is another surface investigation technique, which is used widely. The main idea is to ionize the atoms on the surface of the sample by bombarding it with a beam of electrons. The excited atoms lower their energy by emitting Auger electrons. These electrons are detected by electron spectrometer. Auger electrons have distinctive energies, characteristic of the atoms from which they are emitted. AES has many application areas from chemistry to material science. AES is employed to identify the elements on the material surface and it is also used to determine the atomic concentration of elements. In our surface investigations, we have utilized AES to determine and monitor the elemental composition of the nanoparticles on the LMO:MgO composite cap films.

4.2.5 Transmission Electron Microscopy and Z-contrast

Transmission electron microscopy (TEM) and light microscopy use the same basic ideas. TEM exploits electrons instead of light to examine the specimen. When the electrons focused by electromagnetic lenses are sent through the sample, some electrons are scattered elastically and some inelastically by the sample. Inelastically scattered electrons cause (produce) background noise. Therefore, they do not have any contribution to the formation of an image. Those elastically scattered electrons are projected on the fluorescent screen placed at the bottom of the microscope that is used to construct the image. Nanosize objects can be detected by TEM method. It is used from material science to biology.

In our studies, we have used high-resolution transmission electron microscopy (HRTEM) and TEM equipped with energy dispersive spectrometry for cross-sectional examination of interfaces between HTS and buffer layers. In addition to TEM, scanning transmission electron microscopy (STEM) is also used to investigate heterostructures. STEM employs a high angle annular dark detector that captures (detects) elastically and quasi elastically scatter electrons to analyze the chemical composition by Z-contrast image. It has been demonstrated that such high angle scattering is sensitive to the atomic number of the scattering atoms (via Rutherford scattering) and therefore gives qualitative information of the local chemical composition [66-69]. Even very complicated chemical composition of heterostructures can be determined by Z-contrast imagining in STEM with nanometer spatial resolution. In our studies, we have employed Z-contrast image to investigate the structure of nanocolumns in the composite cap layer.

4.3 Electromagnetic Characterization

4.3.1 Magnetic Measurements of REBCO Thin Films

The magnetic measurements of REBCO thin films at different thickness and compositions were performed by SQUID-based Magnetometry and Vibrating Sample Magnetometry (VSM). Samples were cut to size by shearing; damaged or cracked edges of the sample were removed via the laser scribing to make sure there were no damage or cracked regions on the edges of the sample. In order to determine the critical temperature, $T_c \sim 91$ K for all investigated samples, a 10 Oe magnetic field was applied to the sample, after cooling to 5 K in zero applied field. Upon subsequent warming of the sample, the T_c was determined from the disappearance of this Meissner state diamagnetic signal. The magnetic relaxation measurements were conducted in a Superconducting Quantum Interference Device (SQUID) magnetometer. For creep measurements, 4×4 mm^2 samples were used. The sample was first zero field-cooled to a desired temperature. To ensure that the creep measurements were performed in the critical state, the magnetic field (applied normal to the plane of the film) was changed by sufficiently large amount to force flux penetration to the center of the sample: for example, a -1 T field was first applied, then the applied field was increased up to measurement field of +1 T. After fixing the magnetic field, the decaying magnetization $M(t)$ was measured for a period of ~ one hour. Values for $M(t)$ were determined for both increasing and decreasing field histories in the temperature range 5-77 K. In order to maintain the sample in a highly homogeneous

region of magnetic field in the SQUID magnetometer, a scan length of 3 cm was used during the creep measurements.

We have obtained the *E-J* characteristics of REBCO thin films from creep measurements utilizing Eq. (2.29). In addition to SQUID magnetometry, the magnetic moments of square samples, 2x2 mm^2, were measured continuously using the Vibrating Sample Magnetometer (VSM) capability in a Quantum Design PPMS system. The applied magnetic field was swept at a controlled rate in the range (200-10) Oe/s. The average induced electric field E at the perimeter of the sample was determined by Eq. (2.22).

4.3.2 Critical Currents of REBCO Thin Films

For investigated superconducting films, the J_c values were determined by transport and magnetic SQUID and VSM measurements. In magnetic measurements, the modified critical model [24-26] was applied to the magnetic hysteresis to calculate J_c values via Eq. (2.31). All magnetic measurements were performed at the temperature range 5-95 K and field range 0-6.5 T for both SQUID and VSM methods. The applied magnetic field was parallel to the c-axis of the films. The transport J_c values were assigned at a 1 μV/cm criterion at liquid temperature, 77 K. Angular dependence studies were conducted by electrical transport at 77 K in a 1 T applied magnetic field.

4.4 The SQUID Magnetometer

In our magnetic measurements, a SQUID magnetometer, whose schematic diagram is shown in Fig. 4.3, was utilized. This device can measure changes in magnetic flux on the order of one flux quantum, $\phi_o = \frac{hc}{2e} \cong 2.0678 \times 10^{-15} Tm^2 \cong 2.07 \times 10^{-15} Wb$.

Our commercial SQUID magnetometer can detect smallest magnetization down to 10^{-8} emu and up to 300 emu. The field range is 0.05 G to 70 kG with uniformity of 0.01% over 4 cm. The temperature range is 1.9 K to 400 K with an accuracy of 0.01 K.

The sample, which is mounted on the end of the sample rod within a plastic straw, is moved slowly through a set of detection coils coupled to the SQUID sensor via a superconducting flux transformer as exhibited in Fig. 4.4. The moving sample induces a current in the detection coils proportional to magnetic flux variation. The signal is detected by a SQUID sensor, which converts current to voltage with a high sensitivity. Hence, the magnetic moment of the sample is proportional to the voltage variations generated by the SQUID electronics. The applied magnetic field is produced by a superconducting magnet made of niobium-titanium (Nb-Ti) multi filamentary wire. The critical temperature of Nb-Ti is ~9 K, hence in order to keep the magnet superconducting, and the SQUID sensors functioning, a constant supply of liquid helium (He) is needed when the magnetometer is used. In order to assure a good homogeneity of field during the measurement, we have used scans of 3 cm through coil set.

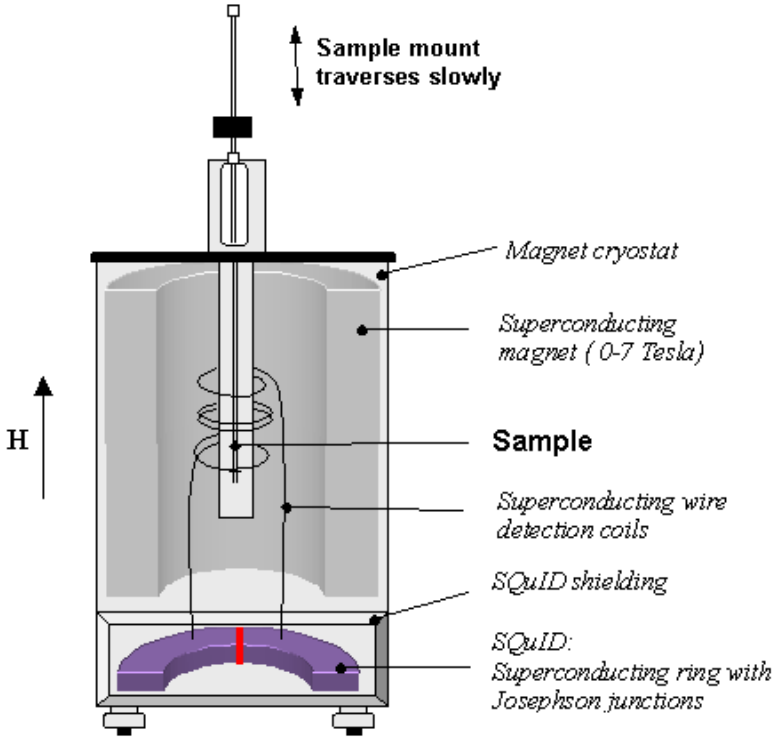

Figure 4.3. Schematic diagram of a SQUID magnetometer

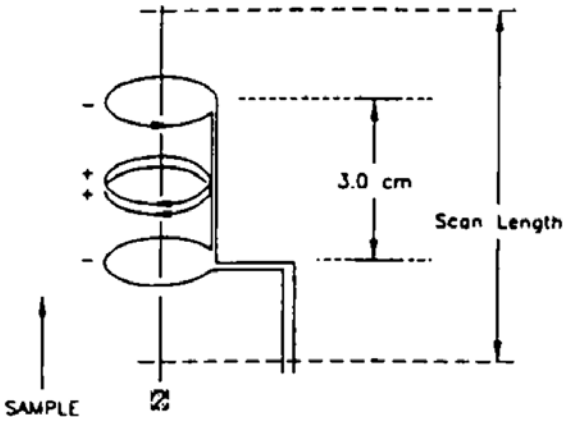

Figure 4.4. A flux transformer with a second-derivative coil geometry in the sample space

4.5 The Vibrating Sample (VSM) Magnetometer

The VSM, shown schematically in Fig. 4.5, uses an electromagnet which provides the magnetizing field (DC), a vibrator mechanism to vibrate the sample in the magnetic field, and detection coils which generate the signal voltage due to the changing flux emanating from the vibrating sample. In the Quantum Design "Physical Property Measurement System (PPMS)," the VSM linear motor transport employs a uniquely designed linear motor to vibrate the sample. The linear motor is designed to operate at 40 Hz, with rapid slewing possible over about 6.5 cm of travel. The large range of motion enables the PPMS VSM system to perform rapid, completely automated centering operations. The output measurement displays the magnetic moment m as a function of the field, H. The sample is attached to the end of a sample rod that is driven sinusoidally. The center of oscillation is positioned at the vertical center of a gradiometer pickup coil. The induced voltage in the pickup coil is amplified and lock-in detected in the VSM detection module. The VSM detection module uses a position encoder signal as a reference for the synchronous detection. This encoder signal is obtained from the VSM motor module, which interprets the raw encoder signals from the VSM linear motor transport.

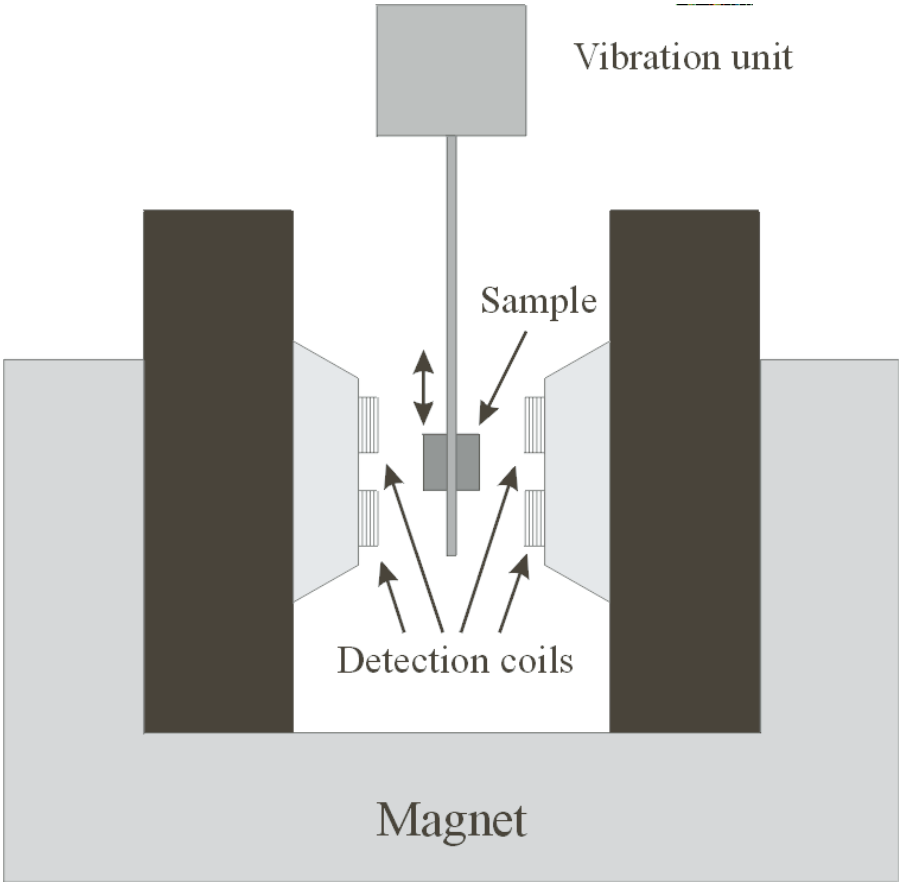

Figure 4.5. A Schematic diagram of a VSM. In the PPMS, the magnetic field is vertical and is supplied by a 8 T superconducting solenoid.

4.6 Transport Method

In this thesis, conventional four-probe transport measurements were carried out at 77 K in magnetic fields up to 1.5 T on a 4 mm wide of tape, where the distance between voltage contacts was 4 mm. First, the sample was immersed in liquid nitrogen at 77 K and magnetic fields were applied perpendicular to the sample surface for determining in-field performance. Typical *E*-field levels are 1 μV/cm, which is the usual transport criterion for the critical current density, J_c. In this method, a progressively larger current was applied to the sample and the corresponding voltage was measured as shown in Fig. 4.6. Transport measurements are most facile at high temperatures or large magnetic fields, where *E* can be measurably large without creating excessive dissipation. In-field performance and angular dependence of J_c of superconducting films were determined via transport technique at 77 K. In-field performance was investigated up to 1.5 T magnetic field. Angular dependence measurements were performed at 1 T applied field, which was varied from -20^o to 120^o. The current was introduced to the sample via copper leads placed by pressure contact onto the films covered by silver pads for low electrical resistance. Moreover, an indium was used between the Ag and Cu leads to prompt good electrical contact.

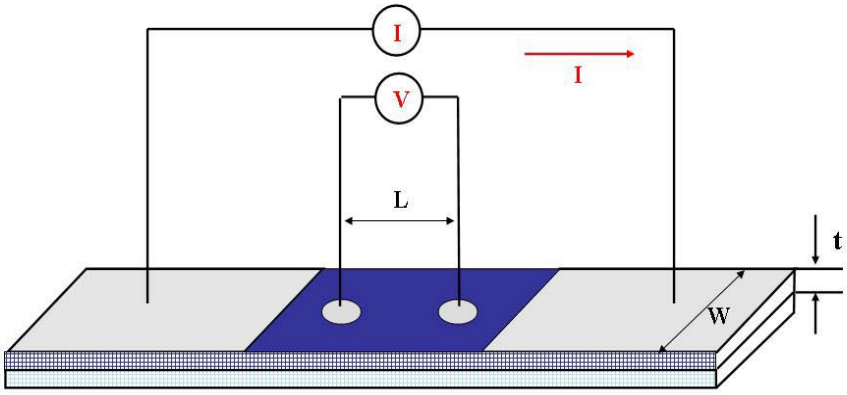

Figure 4.6. Standard four-probe method for the measurement of transport properties of superconducting films.

Chapter 5

Analysis of (RE)$Ba_2Cu_3O_{7-x}$ Thin Films

In this chapter we will focus on the conduction of "critical" currents in high temperature superconductor (HTS) materials, particularly the effects of vortex dynamics. Key superconductive properties of these materials will be broadly characterized by a combination of three complementary experimental methods: conventional four probe electrical transport studies, magnetometry in a swept magnetic field, and SQUID magnetometer-based measurements of current decay (flux creep). We will employ these techniques to determine the superconducting properties of the studied materials as a function of temperature, magnetic field strength and orientation, and film thickness, with electric field levels commensurate with real devices. I have actively participated in the selection of materials and performance of experiments, as well as in the analysis and integration of the data into a coherent, overall picture.

5.1 Investigation of Vortex Dynamics in (GdY)SmBCO and (SmY)BCO Thin Films

After the discovery of the several classes of High Temperature Superconductor (HTS) cuprates, beginning with $La_{2-x}Ba_xCuO_4$ in 1986, tremendous effort has been devoted to the development of these materials from both scientific and application perspectives. From the point of view of applications, HTS have been developed most

prominently as superconducting wires for power devices, where the HTS material must carry large electric currents in substantial magnetic fields. As is well known, HTS are strongly type II superconductors (SC) and in nearly all applications, they operate in the presence of magnetic flux lines (quantized vortices) created by self or externally generated magnetic fields, or both. In order to prevent energy loss caused by their movement, magnetic vortices in HTS must be pinned against motion by nanoscale imperfections and "defects" in the material. Otherwise, flux lines tend to move because of a current-induced Lorentz-like driving force per unit volume, $\mathbf{F} = \mathbf{J} \times \mathbf{B}$, where **J** is the cross-sectional current density and **B** is the magnetic induction (i.e., the area density of vortices). Such flux motion at average velocity *v* induces an electric field in the material, $\mathbf{E} = -\mathbf{v} \times \mathbf{B}$, that is parallel to the current flow. Over a range of a few decades in the electric field, measurements typically yield voltage-current relations that appear power-law in nature, where $E \propto J^n$, with an exponent (the "index" or *n*-value) indicative of the current-induced moving vortices. The features of this exponent are of fundamental interest because it reflects the nature of non-uniform vortex motion. The *n*-value is also of significant practical importance, because the level of the "index losses", $w = E.J \propto J^{n+1}$, is the heat per unit volume that will be generated within the superconductor at the operating current density *J*. For most applications, a material with higher *n* values is generally more desirable because small reductions in operating *J* values lead to dramatically smaller *E*, thereby reducing the intrinsic index losses. Since the *E*-*J* characteristics effectively encapsulate the conductive and vortex state properties of the material, and as such strongly affect the electromagnetic behavior of high temperature

superconducting devices, it is highly useful to investigate the *E*-*J* characteristics over a wide span of electric and magnetic fields in a large temperature range. Figure 5.1 is a schematic illustration of a case where operational criteria require regimes of lower electric field than measured by direct transport. At the operating point, the value of *n* may have evolved to either higher or lower values, and may not be known *a priori*.

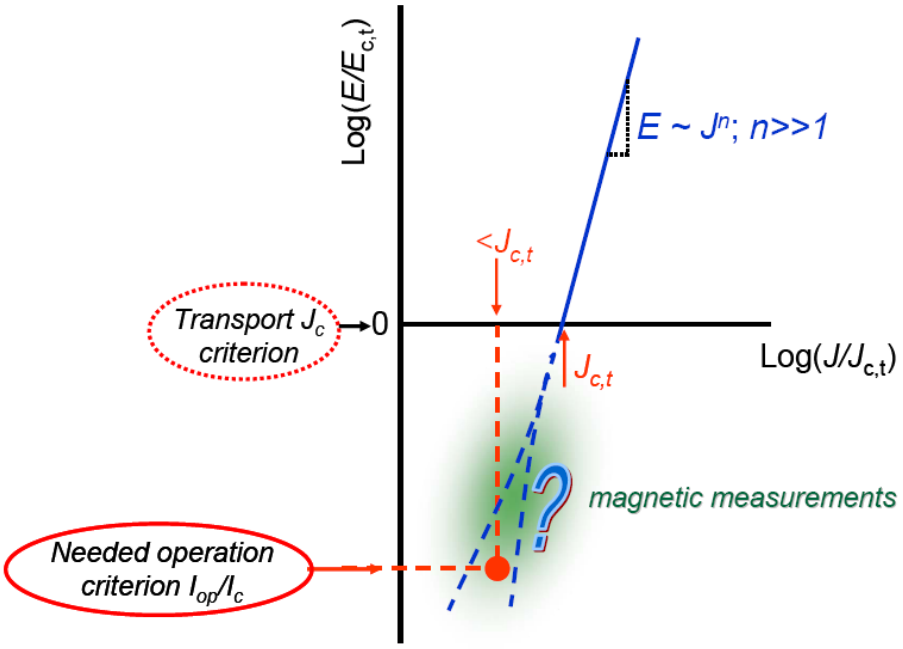

Figure 5.1: A schematic representation of the highly non-linear electric field vs. current density relation for a superconductor. The *E*-field criterion, $E_{c,t}$, that defines the critical current density J_c is too dissipative for some applications. The behavior at low *E* can be investigated on lab-scale samples by magnetometry, to provide both fundamental understanding and needed characteristics for device design.

For measurements on small samples in the laboratory, the lowest transport electric field level is generally limited by the instrumental voltage resolution and voltage tap-spacing, as shown schematically in Fig. 5.2a. In fact, the standard criterion, $E_{c,t}$ = 1 μV/cm, used to define the transport critical current density, $J_{c,t}$, is too dissipative (on the order of watts/cm^3 of superconductor) for many applications.

It turns out that complementary measurements using magnetometry techniques can provide this information as well as enabling a more comprehensive analysis of vortex dynamics over a wide range of voltage-current characteristics. These complementary techniques involve control or observation of the electric field level through the rate of flux change in the sample. Figure 5.2b shows that this can be done by sweeping the magnetic field at a fixed rate, and Fig. 5.2c represents this effect due to the time dependent decay of supercurrent, which generates an internal electric field via Faraday's Law.

In HTS, it is common that thermal excitations also promote flux lines to overcome their pinning energy barriers and occasionally move. This contribution to flux line motion is referred to as magnetic relaxation or flux creep. Creep determines the *E*-*J* characteristics (electric field *E* versus current density *J*) at low dissipation, and it affects the time and temperature dependence of the current density. In addition, it sets limits to the stability of HTS devices in power applications. In the following, we discuss experimental studies of low-level energy dissipation as it relates to the physics of vortex motion in an HTS coating of prototype second-generation wire ("coated conductor").

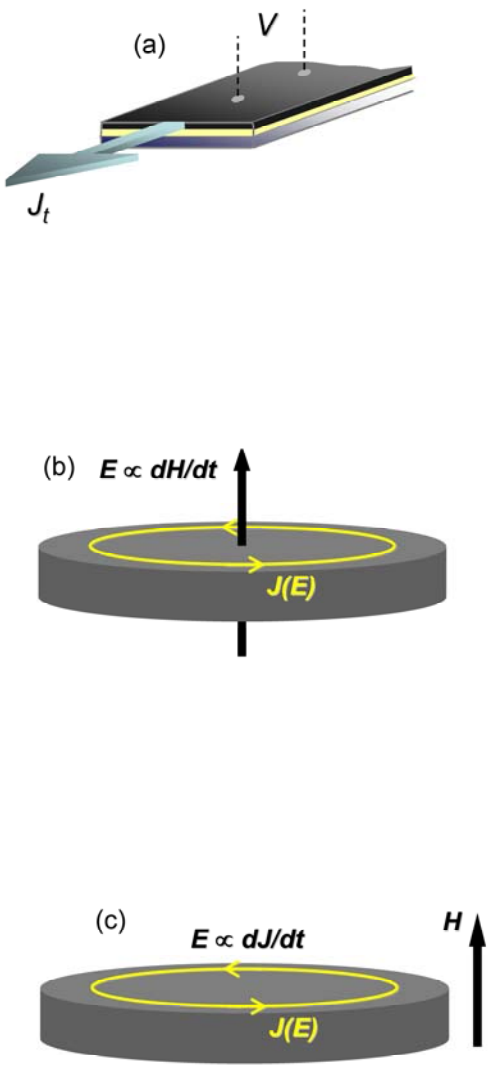

Figure 5.2: (a) Schematic representation of a transport current measurement on a lab-scale sample. The range of accessible currents and voltages in determining $E(J)$ is often limited by the sample size and instrumental resolution. Typical electric fields are ~10^{-6} V/cm. (b) A contactless measurement of $E(J)$ by measuring the supercurrent induced magnetic moment, where E is determined by the change of flux under a constant magnetic field sweep rate dH / dt. (c) Contactless measurement where the electric field is induced by a time decay of the supercurrents.

In this section, to illustrate how the *E-J* characteristics of two representative coated conductors can be determined, two (RE)$Ba_2Cu_3O_{7-x}$ coated conductors in the form of a highly *c*-axis textured, 3 μm thick and 0.7 μm thick films of (SmY)BCO and (GdY)SmYBO, respectively, were investigated. As noted, three complementary methods were used: four-probe electrical transport technique, magnetometry in a swept magnetic field, and magnetic relaxation or "flux creep" measurements. The measurements were performed for wide range of temperature (5-77 K) and magnetic field to 1.5 T or higher. The various investigative methods created electric fields in the region from 10^{-5} to 10^{-13} V/cm, leading to approximate power-law behavior with $E \sim J^n$. The *n* values of two investigated samples were estimated from the *E-J* curves. It is also possible to estimate the power-law index *n* from the relaxation (decay with time) of the critical (persistent) current density. It is found that *J* values of (SmY)BCO and (GdY)SmBCO decay approximately logarithmically with time *t,* as expected from the Anderson-Kim model for creep [14, 15]. As described later, the slope of a log*J*-log*t* plot gives the normalized creep rate *S* that is related to the index *n* via the relation $S=1/(n-1)$ [70]. However, at high temperatures and long relaxation times, the nominally logarithmic relation between *J* and *t* becomes nonlinear, as shown earlier in long-term relaxation experiments [71, 72]. For both superconducting film, the temperature dependence of the relaxation rate $S(T)$ exhibits three different regions. At low temperatures, *S* increases with temperature. In this region, the induced macroscopic current density can be relatively close to the critical current density. This region is followed by a plateau, where *S* values are independent of temperature [73]. At high temperatures, *S* increases again with temperature. These

various features provide insight into the pinning of vortices that is ultimately responsible for the super-conduction of high density electrical currents with minimal dissipation.

5.1.1 Critical Currents

Let's consider first the magnetic field dependence of critical current densities of (SmY)BCO and (GdY)SmBCO films at 77 K for different measurements methods. As noted, these techniques were transport, swept field magnetization, and creep measurements. The J values were magnetically determined by applying Eq. (2.31). Figures 5.3a and 3b show the dependence of J on the applied magnetic field for (SmY)BCO and (GdY)SmBCO samples, respectively. Here we find that that J exhibits a plateau for sufficiently small magnetic fields (up to $\mu_o H < 0.01$ T). In this plateau region, vortices are individually pinned by pinning centers. At higher fields, a gradual transition to an approximate power-law behavior, i.e., $J_c(H) \propto H^{-\alpha}$, was found as can be seen in the log-log presentation. When the magnetic field approaches the irreversibility field, the current density departs from the power-law dependence and decreases rapidly. Focusing on the power-law region in Fig. 5.3, it can be seen that the slopes vary systematically, i.e., $\alpha = -\partial \ln(J)/\partial \ln(H)$, depends on the electric field.

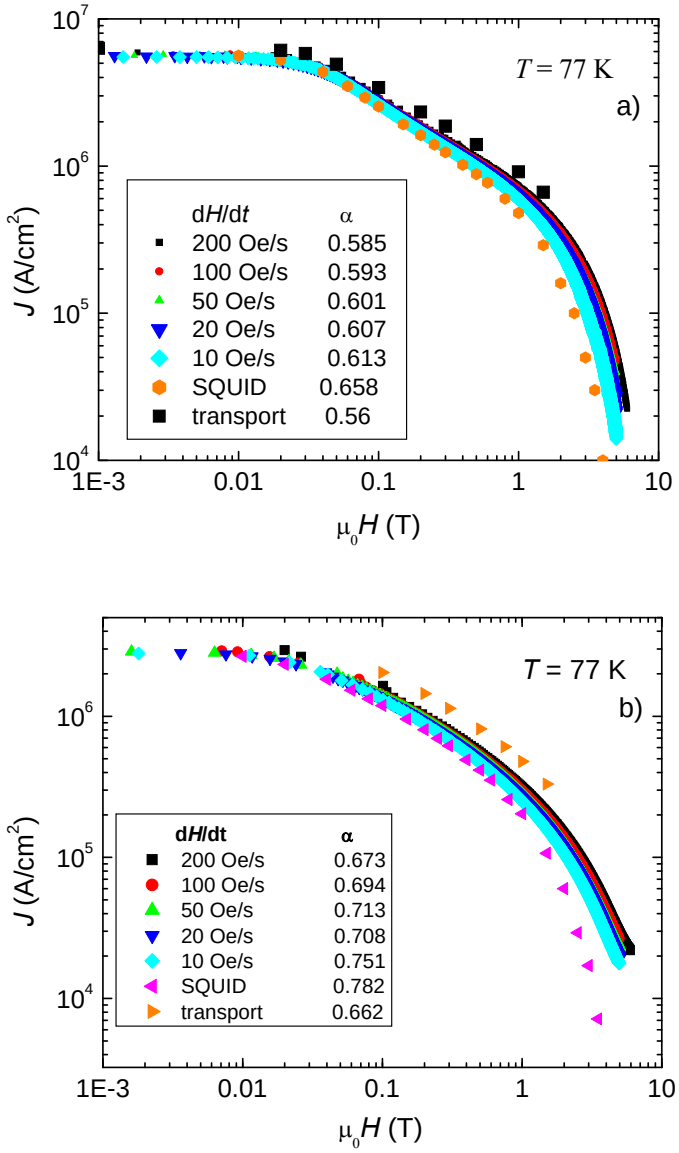

Figure 5.3: The current density J as a function of magnetic field, $H \parallel c$, for a) 3 μm thick (SmY)BCO and b) 0.7 μm thick (GdY)SmBCO coated conductors at 77 K. Data were obtained using three different methods: transport, swept field VSM, and SQUID-based magnetometry.

The resulting dependence is well demonstrated in Fig. 5.4a, a plot of α versus E, for 3 μm thick (SmY)BCO film. On the other hand for the (GdY)SmBCO sample, shown in Fig. 5.4b, the variation is far less apparent. But the tendency, a decrease in the α values with increasing E field criteria, can be noticed. Empirically, it is clear that the values of α at T = 77 K decrease logarithmically as E varies over approximately four orders of magnitude. This relationship can be obtained by combining of the field dependence $J \sim H^{-\alpha}$ with the power-law characteristic $E \propto J^n$, which will be discussed in detail in the next section. This leads straightforwardly to a logarithmic dependence, $\alpha(E)=\alpha(E_c)+n^{-1}[dln(n)/dln(H)] \times ln(E/E_c)$, where E_c is a standard criterion, e.g., 1 μV/cm. A closer examination of Fig. 5.4 reveals that α value varies with temperature and has a minimum value near 40 K, with α eventually becoming nearly independent of E for investigated samples at low temperatures [74]. The temperature dependence of α reflects details of the underlying flux pinning; its dependence on E-field is likely a general phenomenon, especially at higher temperatures. From Figs. 5.3 and 5.4, it is clear that the two REBCO films have different flux pinning mechanisms.

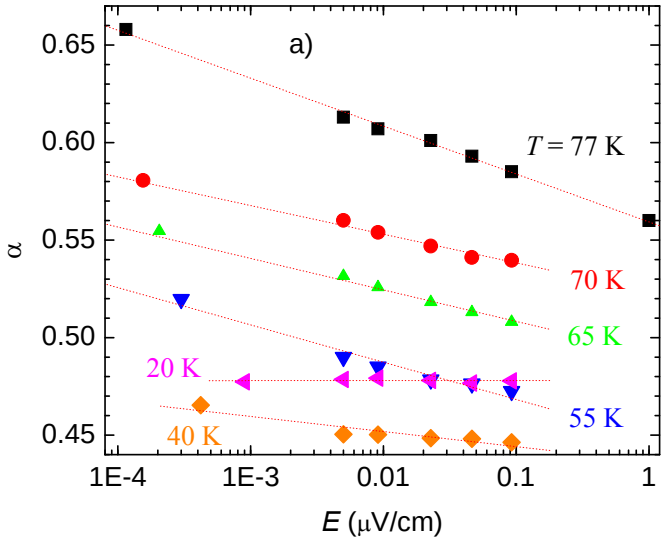

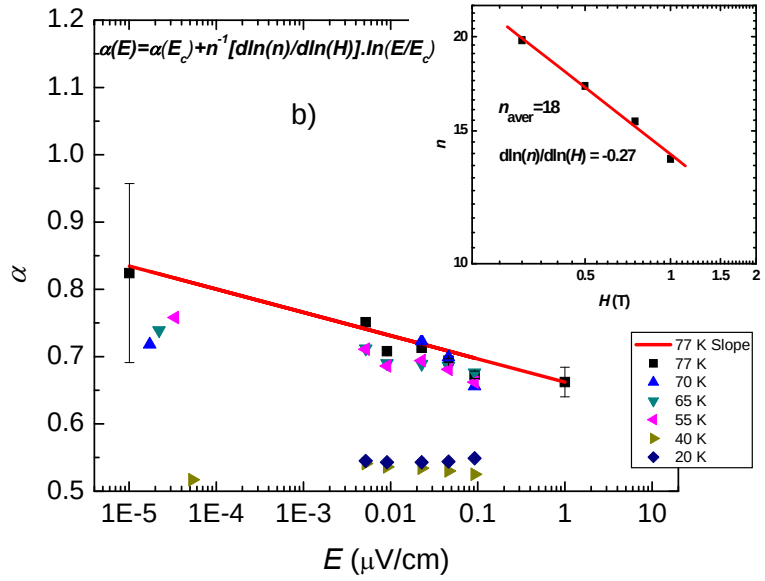

Figure 5.4: Values of $\alpha = -d \ln J / d \ln H$ vs. level of E-field, as observed at the temperatures indicated for a) 3 μm thick (SmY)BCO and b) 0.7 μm thick (GdY)SmBCO.

Now let us clarify the relative pinning strength of the studied samples by analyzing the temperature dependence of J_c at 1 T magnetic field applied parallel to *c*-axis by VSM. It has been shown experimentally [75] and theoretically [76] that in HTS with weak pinning centers, the J_c decays exponentially with temperature. This decay can be described by the following equation

$$J_c^{wk}(T) = J_c^{wk}(0).e^{-(\frac{T}{T_o})} \tag{5.1}$$

Here $J_c^{wk}(0)$ is the weak pinning contribution to the J_c at 0 K and T_o is the characteristic energy of vortex pinning at weak pinning defects. Nelson et al [77] and Hwa et al [78] have predicted that in HTS materials with strong pinning centers, such as correlated defects, J_c decays slowly and shows smoother temperature dependence, described by

$$J_c^{str}(T) = J_c^{str}(0).e^{-3(\frac{T}{T^*})^2} \tag{5.2}$$

Here $J_c^{str}(0)$ is the contribution of strong pinning centers to the J_c at 0 K and T^* is the characteristic energy of vortex pinning by strong pinning defect centers. Experimental results have demonstrated that this model can be applied to HTS materials having strong pinning centers [79-82]. Later on Plain et al. have shown a coexistence of both weak and strong pinning effects in melt-textured YBCO ceramics, where different types of defects coexist [83]. In order to describe their experimental data, they used the combination of Eq. (5.1) and Eq. (5.2),

$$J_c(T) = J_c^{wk}(0).e^{-(\frac{T}{T_o})} + J_c^{str}(0).e^{-3(\frac{T}{T^*})^2} \tag{5.3}$$

Figures 5.5a and 5.5b illustrate the temperature dependence of J_c of (SmY)BCO and (GdY)SmBCO films. For both samples, at low temperatures strong and weak pinning contributions are comparable. However, at high temperatures as one can notice the strong pinning contribution dominates the weak pinning contribution. Fitting Eq. (5.3) to the experimental data for $J(T)$, the characteristic temperatures for weak pinning are similar, 14 K and 16 K for (SmY)BCO and (GdY)SmBCO, respectively. Moreover, the characteristic temperatures T_0 for strong pinning are very similar for the two samples, ~ 81 K.

5.1.2 E-J Characteristics

Next we examine the electric field – current density characteristics over a wide range of *E*-fields. In Fig. 5.6 are collected *E-J* data for the (SmY)BCO coated conductor, as obtained from a combination of transport, swept field magnetometry, and flux creep studies. For these data, the sample temperature was 77 K, with measurements in various magnetic fields, $H \parallel c$. It can be seen that the transport measurements generally have the highest *E* field values ~ 1 μV/cm. For the swept field magnetometry study, values for *J* and *E* were calculated by equations (2.31) and (2.22), respectively. The *E* fields produced by the swept field were about 2-3 orders of magnitude lower than those obtained from transport measurements. Finally, the $E(J)$ curves from the flux creep data were extracted using equations (2.29) and (2.32). The creep studies give the lowest *E* values, which were ~6-8 orders of magnitude lower than those from transport.

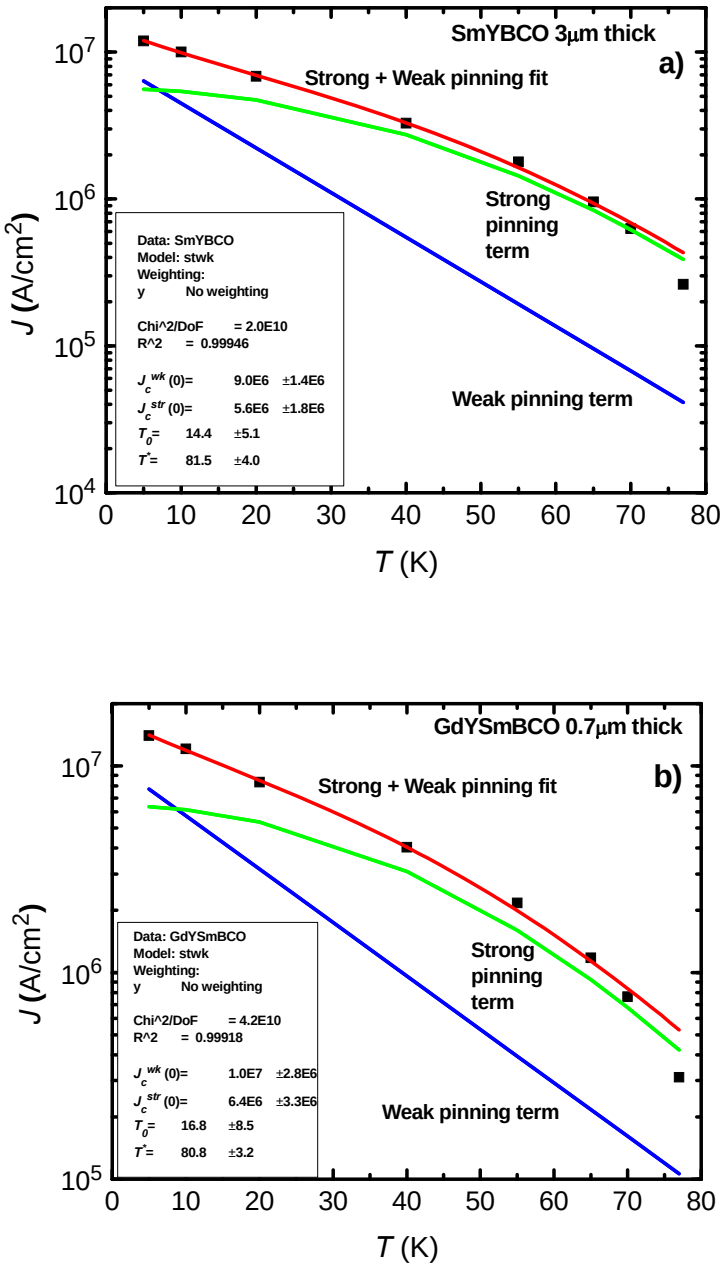

Figure 5.5: The contributions of weak and strong pinning to J obtained from VSM studies with $E \approx 9.2\times10^{-8}$ V/cm, as determined via the temperature dependence, for investigated samples a) 3 μm (SmY)BCO, b) 0.7 μm (GdY)SmBCO thick samples.

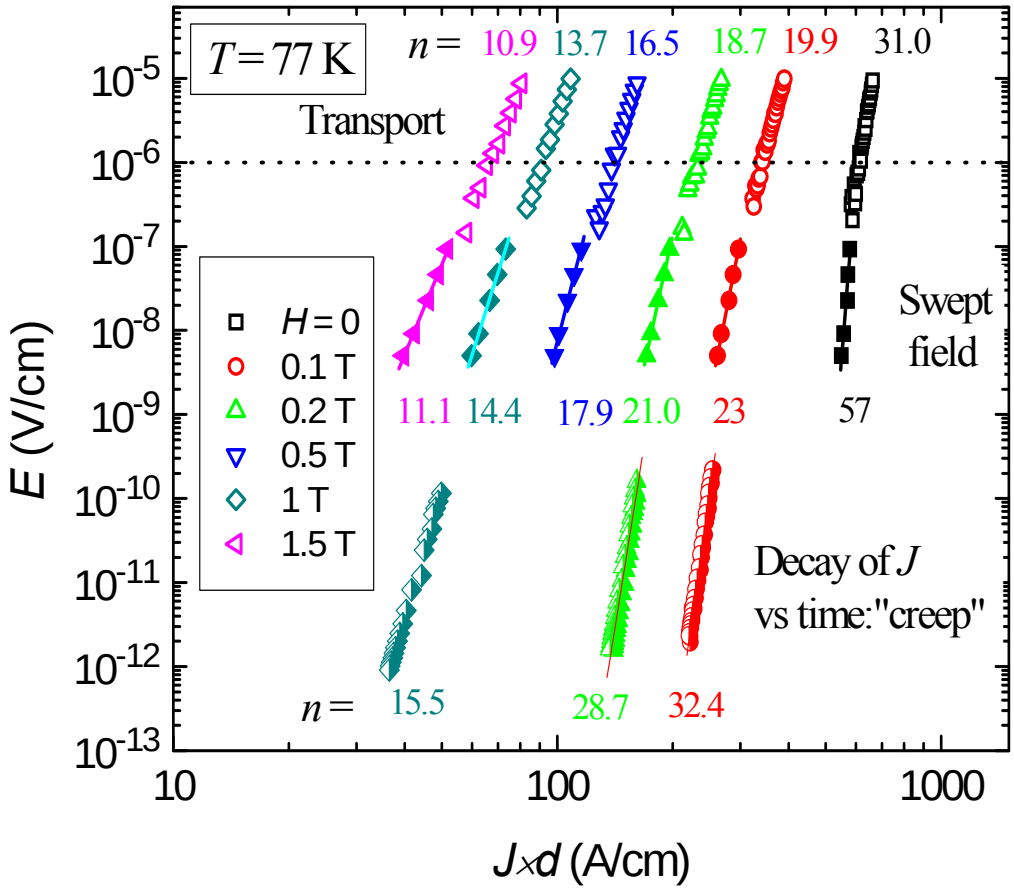

Figure 5.6: Electric field E vs. current per unit width Jd at 77 K, as obtained from transport, swept field VSM, and SQUID-based magnetometry for 3 μm thick (SmY)BCO sample. Values for the power-law index n were determined from slopes in the log-log plots.

The top panel, Fig. 5.7a, shows current density data at 77 K for (GdY)SmBCO obtained from measurements on 3 separate samples of coated conductor. For this material, sample-to-sample variations and sample preparation produced a variation of ~25 % in *J*-values, even when referenced to the same electric field. That variation is visible in Fig. 5.7a as horizontal offsets in data segments measured in the same field, e.g., 0.2 T. To compensate for this effect in the present material, we rescale the swept field values upward by an empirical factor $k = 1.25$, and increase the *J*-values from creep by a factor $k = 1.10$. The rescaled results for $E(J)$ are shown in Fig. 5.7b and in subsequent figures for the (GdY)SmBCO film. The same two scale factors can be used at all temperatures and magnetic fields, implying that the differences are likely geometrical in origin, e.g., remaining small microcracks in the smallest 2×2 mm^2 that is most sensitive to edge damage. For these reasons, it is advisable to study the *same* sample for as many of the measurements as possible. Finally, we note that this is a materials-specific and handling issue. Note that there is no need for rescaling and none was used for the 3 μm thick (SmY)BCO sample. Examination of Fig. 5.6 and 5.7 shows that for individual segments, there is an apparent linearity between *E* and *J* when plotted on log-log scales. This linearity means that the relation between *E* and *J* can be described by a power-law relation, $E \alpha J^n$. This *approximate* power-law dependence was observed in the electric field window of 10^{-5}-10^{-13} V/cm over much of the magnetic field range 0.1-1.5 T. Values for the power-law index *n* were obtained from slopes in the log*E*-log*J* plots. The evolution of *n* values over a wide range of *E*-*J* characteristics reveals significant information about the material.

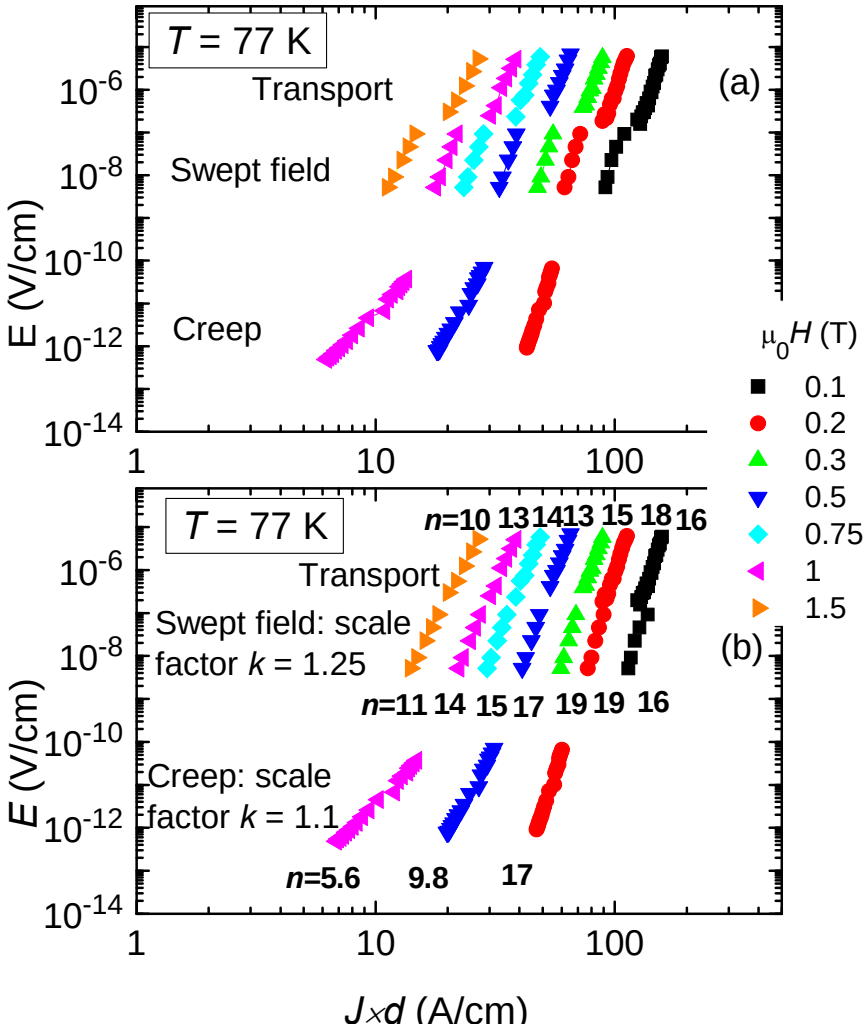

Figure 5.7: Electric field E vs. current per unit width Jd at 77 K, as obtained from transport, swept field VSM, and SQUID-based magnetometry. Values for the power-law index n were determined from slopes in the log-log plots. a) Values as obtained, with no rescaling and b) with J-values rescaled, in consideration of sample-to sample variation.

With the contact-free inductive methods, it is relatively easy to extend measurements to a wide range of temperatures. Figures 5.8a and 5.8b show results from 5 K up to 77 K for studied samples, in a fixed applied magnetic field of 1 T. The figures make it apparent that as the temperature decreases, the current densities become large and the power-law index *n* increases. As one can notice from Fig. 5.8a, the *E-J* curve of (SmY)BCO sample follows the power-law relation even at 77 K. On the other hand, for (GdY)SmBCO sample, there is deviation from the power-law behavior at 77 K, as the *E-J* curves no longer follow a simple power-law-like relation, shown in Fig. 5.8b. Similar deviations are evident in the 77 K data in Fig. 5.7. At this temperature, the *E-J* curve assumes a positive or "S-like" curvature, suggesting the possibility of a phase transition from a vortex glass at lower temperatures to a (pinned) vortex fluid or some other *J*-dependent crossover in the vortex pinning mechanism(s).

The data from the combination of three measurements reveal that there is a general downward curvature in the wide-range log*E*-log*J* plots. This downward curvature is observed for a wide range of temperatures and magnetic fields, except for conditions near the irreversibility line. The downward curvature arises naturally in vortex-glass theory [18, 19] and collective flux-creep theory [20], in which the pinning energy has the form $U(j) \cong U_0(j_0/j)^{\mu}$. Hence the potential barrier for vortex motion tends to diverge as the current density $j \to 0$, meaning that the *E-J* curves get progressively steeper. This increase in energy barrier will be demonstrated more explicitly in a later section on "Maley analysis."

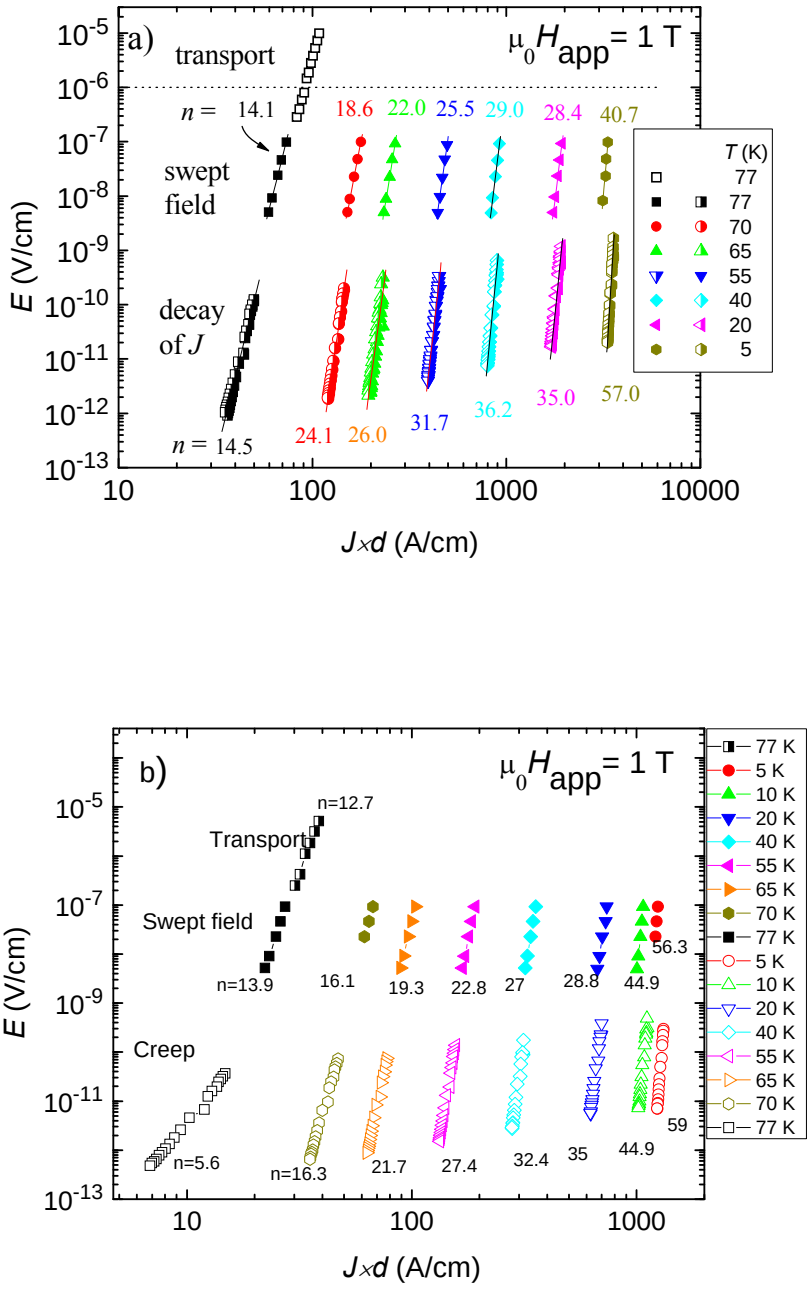

Figure 5.8: The *E* vs. *Jd* characteristics extending to low temperatures, with an applied magnetic field *H* = 1 T applied field along the *c*-axis. Corresponding *n*-values are indicated for a) (SmY)BCO and b) (GdY)SmBCO films.

5.1.3 Creep Measurements

In creep measurements, the current density of the sample at any given time was obtained using the Eq. (2.32). The decay of the persistent current density with time (magnetic relaxation) of the (SmY)BCO superconductor was measured at different temperatures in the range 5-77 K, in magnetic fields of 1 T and 3 T, and the results are shown in Fig. 5.9a and 9b in log-log presentations, respectively.

The magnetic relaxation of the (GdY)SmBCO film was measured in 1 T and 3 T and the data are illustrated in Fig. 5.10a and 10b, respectively. In Fig. 5.9 and 5.10, the value of the current density appears to decrease logarithmically with time. Hence the logarithmic decay rate S corresponds simply to the slopes of the curves in these figures. It should be noted, however, that when viewed over a longer time period, the relaxation of $J(t)$ becomes nonlogarithmic with time, as shown earlier in long term relaxation studies lasting of orders of days. [71, 72] This nonlogarithmic relation between $J(t)$ and t was well described by Eq. (2.18). In such long term creep studies, the quantity S becomes weakly time dependent, as is evident in Eq. (2.20) [84].

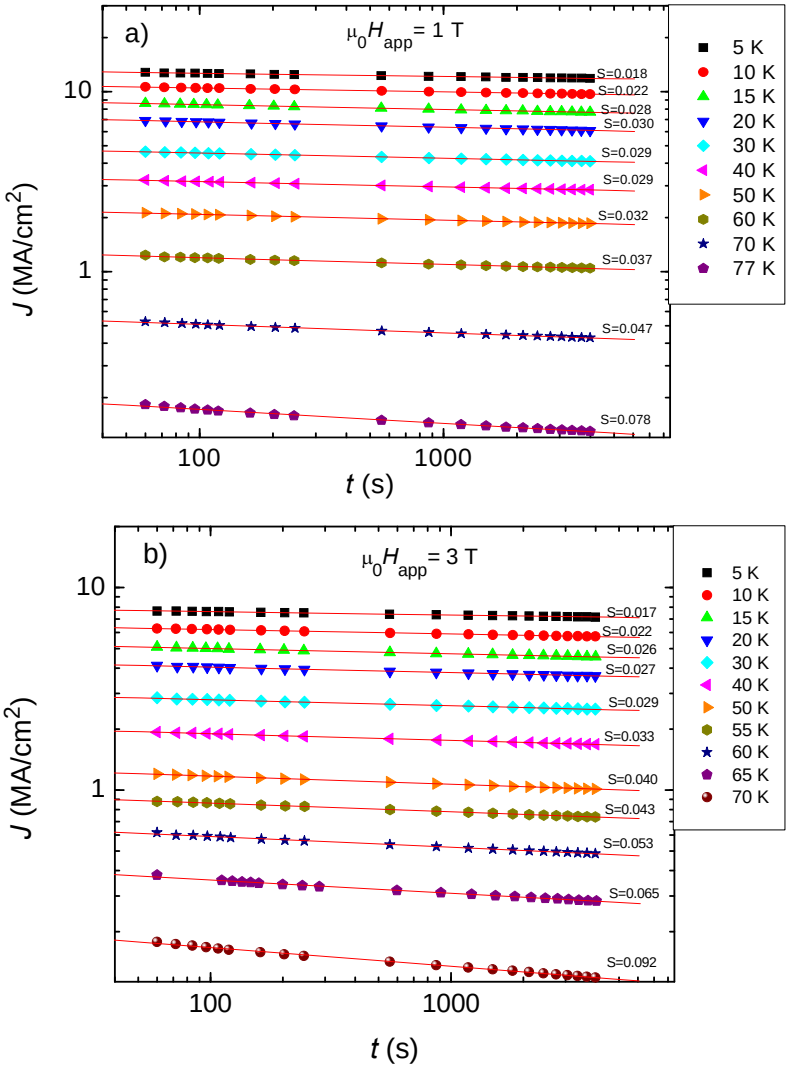

Figure 5.9: Log-log plot of persistent current density J versus time t for (SmY)BCO at various temperatures (5-77 K), in the presence of a) 1 T and b) 3 T magnetic fields applied along the c-axis. The normalized creep rate S was determined from slopes in the log$J$-log$t$ plots.

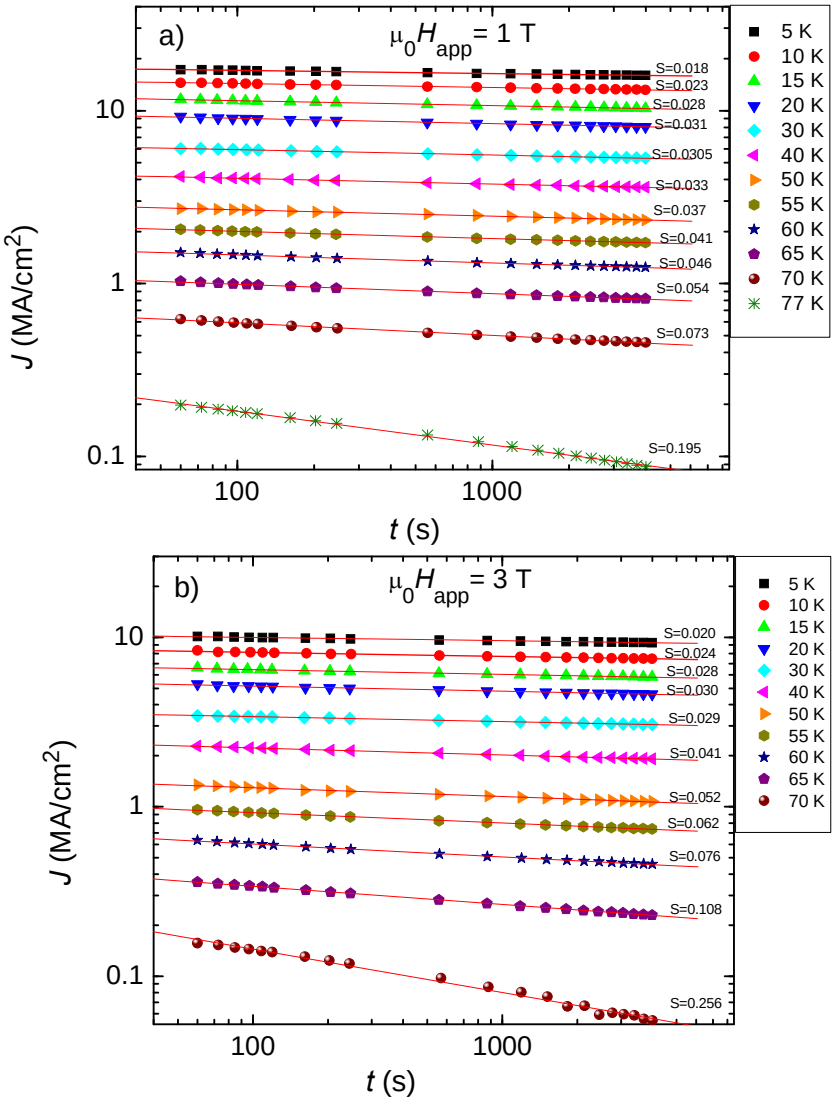

Figure 5.10: Log-log plot of persistent current density J versus time t for (GdY)SmBCO at various temperatures (5-77 K), in the presence of a) 1 T and b) 3 T magnetic fields applied along the c-axis. The normalized creep rate S was determined from slopes in the log$J$-log$t$ plots.

Now let's look at the temperature variation of the normalized creep rate S, as shown in Fig. 5.11 for the (SmY)BCO sample. The temperature variation of creep rate S for the (GdY)SmBCO thin film is exhibited in Fig. 5.12. As noted, these measurements for both REBCO coated conductors were conducted in 1 T and 3 T fields parallel to the c-axis, with results measured in both increasing and decreasing magnetic field histories. Three different regions [85] are evident for both samples at 1 T and 3 T magnetic fields. First, the values of S increase almost linearly at low temperatures, 5-20 K. This increase in the creep rate S is explained by the "interpolation formula," Eq. (2.18). In this low temperature region, the Anderson-Kim model [14, 15] also predicts a linear increase of S with temperature T, considering a finite energy barrier U_o giving $S = k_B T/U_o$. Second, $S(T)$ is nearly constant at intermediate temperatures, 20-50 K, where it forms a "universal plateau" as proposed by Malozemoff and Fisher [73]. Eq. (2.21) derived from "interpolation formula" predicts this plateau region. Third, the rate S increases steeply for $T \geq 50$ K, which can be understood as a decrease of the pinning energy scale $U_o(T)$, due to changes in fundamental parameters, e.g., increases in the penetration depth and coherence length, which gradually smoothes and flattens the pinning energy landscape.

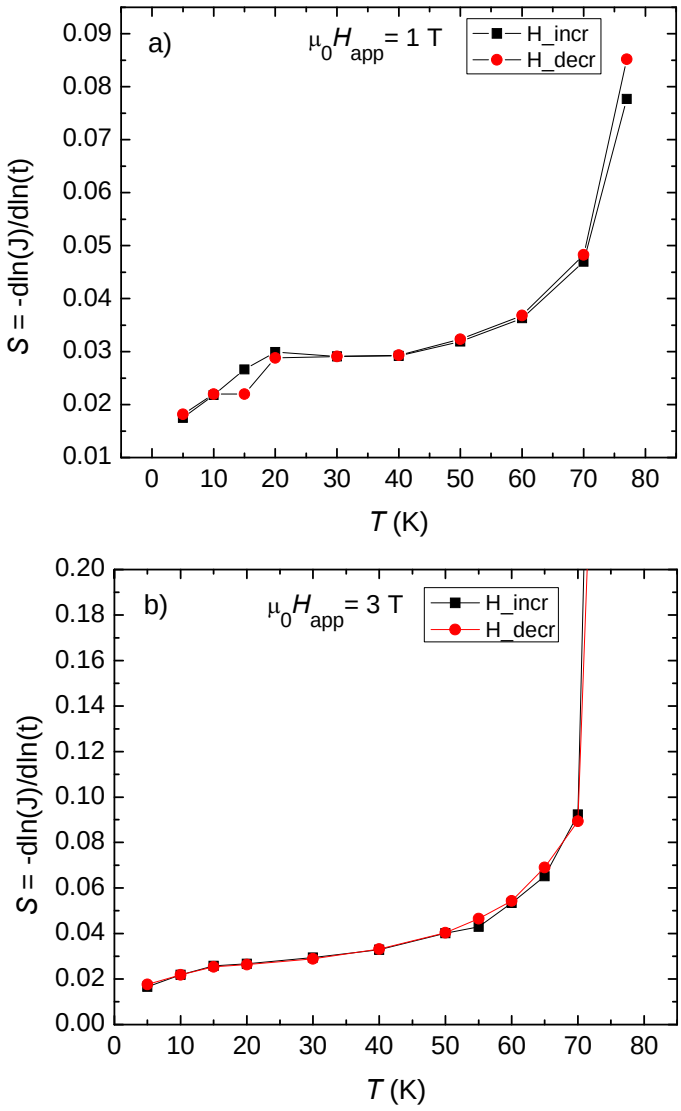

Figure 5.11: The normalized creep rate S versus temperature measured in a) 1 T and b) 3 T with increasing and decreasing field histories for (SmY)BCO sample.

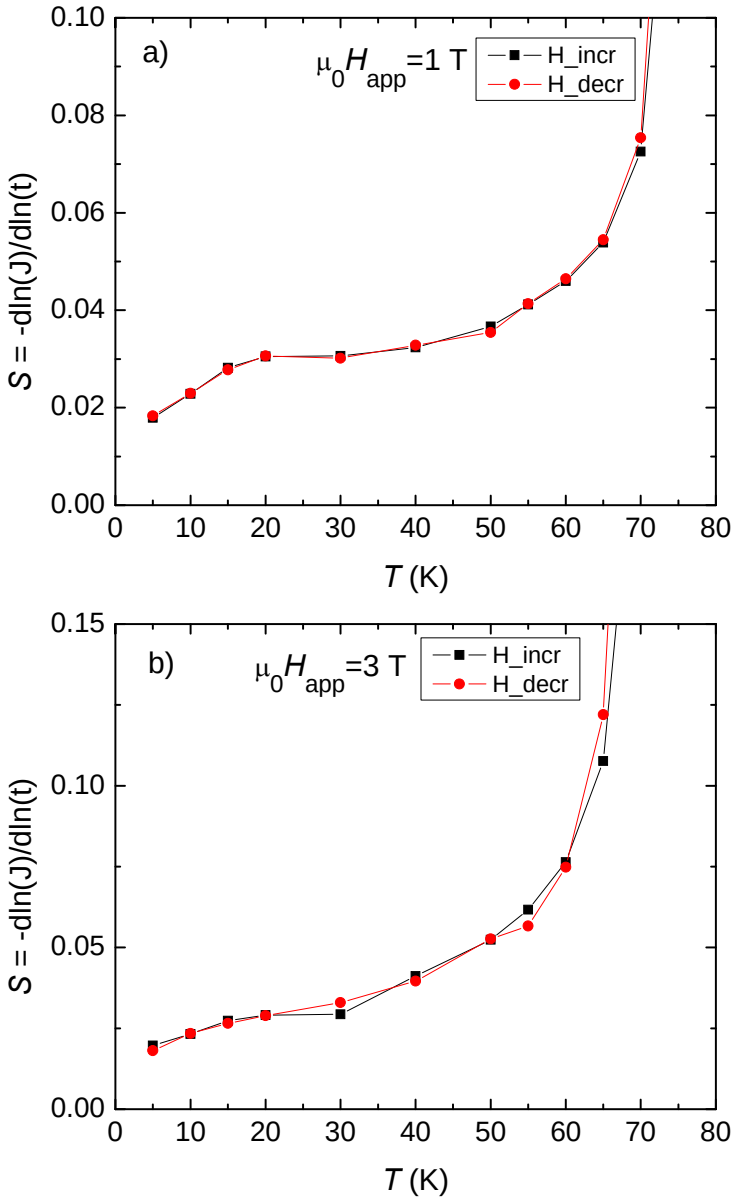

Figure 5.12: The normalized creep rate *S* versus temperature measured in a) 1 T and b) 3 *T* with increasing and decreasing field histories for (GdY)SmBCO sample.

Maley Analysis:

The decay of persistent currents with time is a consequence of vortex depinning. Aside from low temperatures where quantum tunneling of vortices may occur, the depinning of vortices is thermally activated, with an effective pinning energy $U_{eff}(J,T)$ that depends on both *J* and *T*. In an analysis first formulated by Maley et al. [86], one considers a sort of master rate equation containing a Boltzmann factor giving the probability of depinning in the presence of an attempt frequency $(1/\tau)$, so that

$$dJ/dt = -\left(\frac{J_c}{\tau}\right)\exp\left(-\frac{U_{eff}(J,T)}{T}\right) \tag{5.4}$$

Here $k_B = 1$ so that energies are measured in units of Kelvins. Experimentally, one has data for *J*(*t*) at various temperatures, so Eq. (5.4) can be solved for *U*. The factor $\ln(J_c/\tau)$ is treated as an unknown constant that is varied to construct a smoothly varying *U* vs. *J* at low temperatures. The results for $U(J,T)$ are shown in Fig. 5.13a and 5.13b as open symbols. It is desirable to isolate, at least approximately, the explicit dependence on *J* from the effects of temperature. To do so, one can assume that effects are separable and, in the spirit of Ginzburg-Landau theory, write $U(J,T) = U(J,T=0)\times(1-t)^p$, where $t = T/T_c$ is the reduced temperature. Here we take *p* = 2. The resulting $U(J,T=0)$ is depicted with filled symbols in Fig. 5.13a and 13b. The log-log presentation shows that *U* increases as *J* decreases, in accord with Eq. (2.17). For $J << J_0$, Eq. (2.17) provides simple inverse power law dependence, as shown by the straight lines in Fig. 5.13a and 13b.

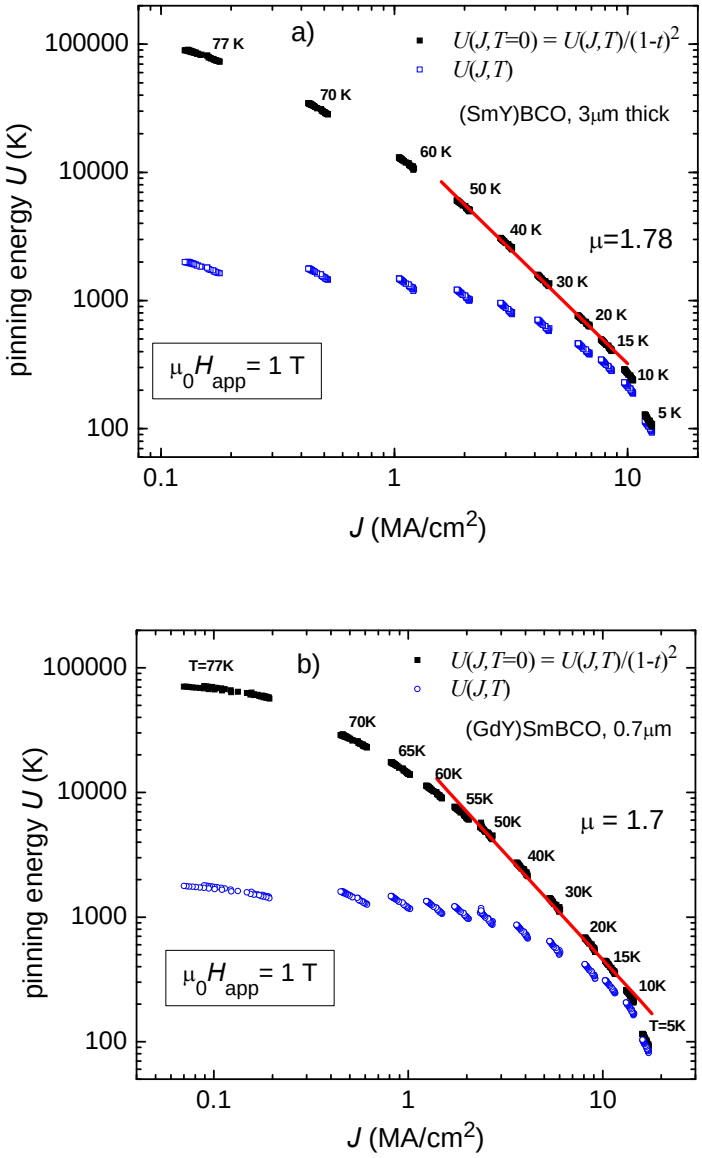

Figure 5.13: Current dependence of the effective pinning energy, which is deduced by using a Maley analysis, in 1 T applied magnetic field. a) 3 μm (SmY)BCO and b) 0.7 μm (GdY)SmBCO thick films. Open symbols represent $U(J,T)$ from the magnetic relaxation, conducted at the temperatures shown. The temperature effects are considered by the relation of $U_{eff}(J;T=0) \approx U_{eff}(J;T)/G(T)$; results are presented as filled symbols.

The slopes correspond to a value of ≈ 1.7 for the glassy exponent μ, which lies near the theoretical value 3/2 for hopping of small vortex bundles. This mechanism appears to be dominant (in a 1 T field) for temperatures 15 – 50 K for both investigated coated conductors, above which temperature (and below which current densities) vortex motion becomes progressively easier until the irreversibility line is reached.

Power law index *n:*

Finally, let us return to the technologically important parameter n in the power law characteristics $E(J)/E_c = \left(J/J_c\right)^n$. The temperature dependence of n in the presence of a 1 T applied field is shown in Fig. 5.14a and 14b. These data originate from both swept field and creep studies. For the latter, note that the normalized relaxation rate $S=-d\ln(J)/d\ln(t)$ is inversely proportional to n via the relation [70] $S=1/(n-1)$. The figure shows that the n values increase as the temperature decreases, meaning that the E-J curves are getting steeper, as is qualitatively evident in Fig. 5.8.

The dependence of n on magnetic field is exhibited in Fig. 5.15a-15d for (SmY)BCO film, for several different temperatures.

Finally, the field dependence of n value is illustrated in Fig. 5.16a-16d for temperatures of 20 K, 55 K, 65 K and 77 K. For the investigated (GdY)SmYBCO sample at low temperatures, e.g., $T = 20$ K, n is nearly constant in the field range explored (up to 4.5 T). At higher temperatures, the values progressively decrease as either the magnetic field H or the temperature T is elevated.

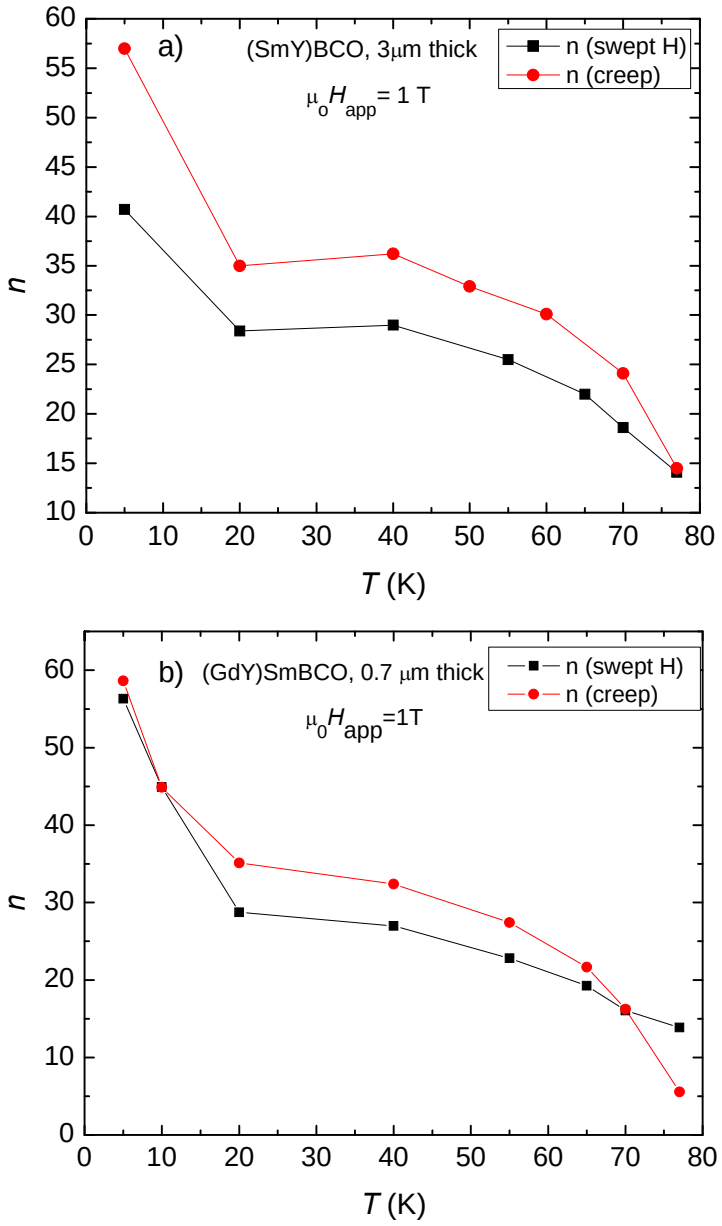

Figure 5.14: The power-law index n values obtained from swept field VSM, and SQUID-based magnetometry versus temperature T, measured in the presence of 1 T applied magnetic field for a) (SmY)BCO and b) (GdY)BCO thin films. The inverse proportionality between power index n and the relaxation rate S can be seen comparing Fig. 5.11a and Fig. 5.12a

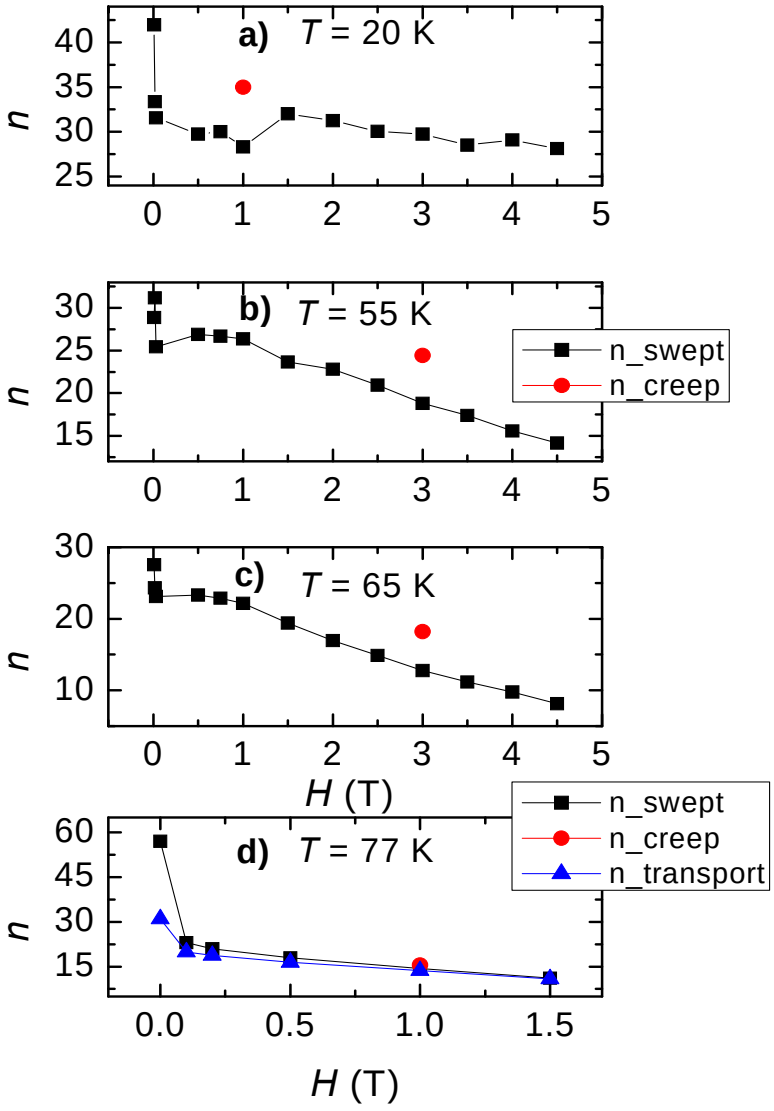

Figure 5.15: The magnetic field dependence of the *n* values determined from swept field VSM, and SQUID-based magnetometry at a) 20 K, b) 55 K, and c) 65 K. In figure d) at 77 K, *n* values were obtained from transport, swept field VSM, and SQUID-based magnetometry for (SmY)BCO sample.

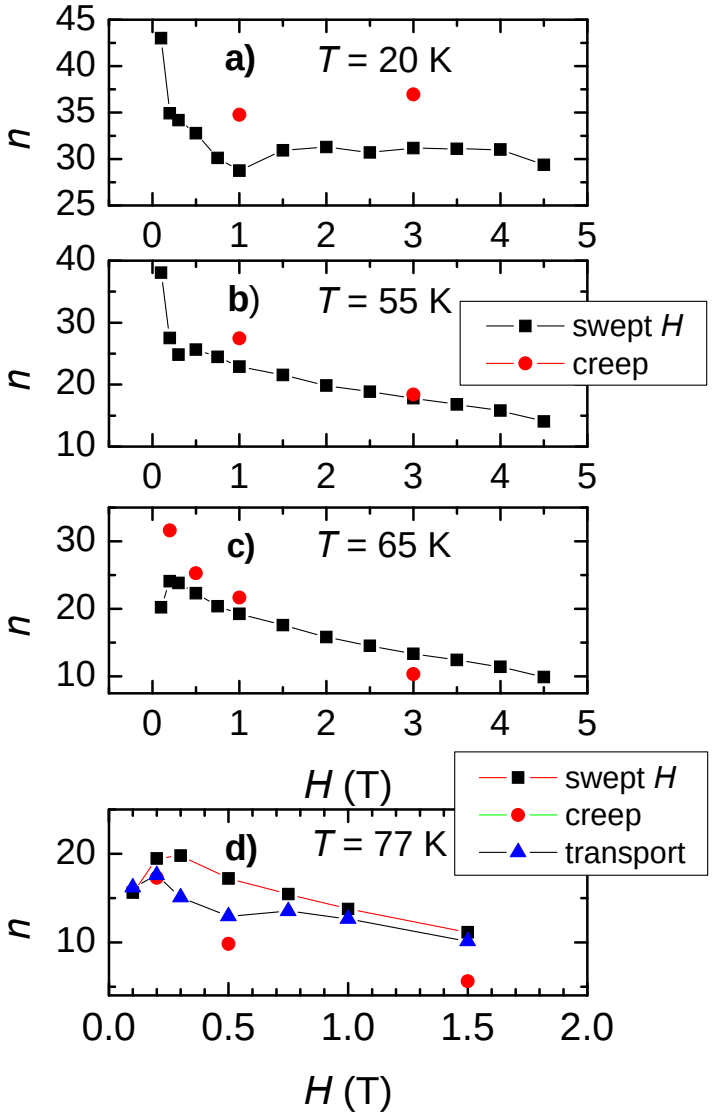

Figure5.16: The magnetic field dependence of the *n* values determined from swept field VSM, and SQUID-based magnetometry at a) 20 K, b) 55 K, and c) 65 K. In figure d) at 77 K, *n* values were obtained from transport, swept field VSM, and SQUID-based magnetometry for (GdY)SmBCO sample.

Chapter 6

Formation of Nanostructures on IBAD Substrates for Added Flux Pinning

In the past 10-15 years, remarkable progress has been made in the development of YBCO-based second generation (2G) coated conductors (CCs). To enhance the critical current and to realize practical applications, it is vital to identify the current limiting mechanisms in the CCs. It has been well demonstrated that a limitation to the critical current a superconductor can carry is vortex motion in the material. In a previous chapter, we have shown that the electric field vs. current density (*E*-*J*) characteristics can be used to investigate the vortex dynamics. It is widely believed that performances improvement of 2G CCs can be achieved through better understanding of vortex-vortex and vortex-defect interactions. In this chapter, we concentrate on the manipulation of the present IBAD template. We first demonstrate fabrication of a simplified IBAD architecture, and then show an enhanced critical current density in YBCO films deposited on these simplified templates, through creation of strong pinning centers within the superconducting matrix.

6.1 Simplification of IBAD Buffer Architecture

YBCO-based second generation (2G) coated conductors are tape-like conductors containing a multilayer architecture with a substrate, a superconductor layer, and a

varying number of buffer layers between the substrate and the superconductor layer. One of the significant issues in the fabrication of high temperature superconductors is the alignment of the crystal grains of the superconducting material. These materials should have biaxially textured crystal grains aligned both parallel to the plane of the layer, *a*-*b* alignment, and perpendicular to the plane of the layer, *c*-axis alignment. This problem can be overcome by employing single crystal substrates, which is the simplest method for obtaining biaxial texturing in the superconducting layer. On the other hand, due to their high cost and poor mechanical properties, single crystal substrates are not appealing for large scale applications of coated conductors. Obviously, for power utility applications, HTS coatings should be formed on long length, flexible wires that can be biaxially textured. There are several different methods used to manufacture biaxially aligned metallic substrates. The most widespread one is so-called Ion Beam Assisted Deposition (IBAD) technique, in which buffer layers can be deposited on metallic substrates with an optimal degree of texture. Note that these buffer layers transfer the desired texture to the subsequent superconductor layer. The present IBAD architecture has several buffer layers, which were described in section 3.2.3. One of the main components of IBAD buffer architecture is the $LaMnO_3$ (LMO) cap layer, the integrity of which is crucial for the growth of high quality HTS coatings. The cap layer of LMO has been shown to ensure a good lattice match and chemical compatibility with the YBCO coatings [62, 63]. Even though other buffer layer materials such as $SrRuO_3$ (SRO) and $SrTiO_3$ (STO) have been used as cap layers with some success [64, 65], neither provided performance levels that were comparable to LMO layers. Some of the main advantages of LMO over SRO or

STO include cost effective fabrication at high deposition rates with a wider processing window, and attainment of higher critical current, I_c, values for YBCO films [56]. In coated conductor architectures, it is well understood that integrity of the cap buffer layer is crucial for epitaxial growth of subsequent HTS coatings. It is also equally important and desirable to minimize the number of buffer layers to reduce the overall process complexity as well as the manufacturing cost. One way to achieve a simplified IBAD architecture is to eliminate the need for the homo-epi MgO layer and to deposit high quality epitaxial cap layers directly on IBAD-MgO templates shown in Fig. 3.1. Note that the lack of successful reports on the growth of SRO and STO cap layers directly on IBAD-MgO apparently led to the persistent use of homo-epi MgO, even after LMO was determined to be a viable cap layer. In fact, only recently have YBCO films with good performance been reported for $Sm_xZr_{1-x}O_y$ cap layers that are deposited directly on IBAD-MgO [87].

In this section, we demonstrate epitaxial fabrication of LMO films on IBAD-MgO templates with no homo-epi MgO layers. We also show that, under the optimized processing conditions, there are no significant structural and morphological differences among the LMO films deposited either on IBAD-MgO or homo-epi MgO layers. Finally, we have established that the performance of YBCO films deposited on both of these architectures is also comparable.

To investigate the effect of different deposition temperatures and sputtering gas mixtures on the crystalline quality of LMO films, detailed XRD analyses were carried out. Figures 6.1a and 6.1b show θ-2θ XRD scans for a series of LMO layers deposited directly on IBAD-MgO templates at various temperatures ranging from 550 to 700^{o}C in pure Ar-4%H_2 and a mixture Ar-4%H_2 + O_2, respectively. It is clear from both figures that the deposition temperature, T_{dep}, plays a significant role on the growth behavior of LMO layers. At $T_{dep} \leq 650^{o}$C, films exhibited both (00*l*) reflections and additional polycrystalline LMO (110) components, signifying that thermal energies are too small to develop a single crystalline LMO phase. Above 650^{o}C, however, the films showed only LMO (00*l*) reflections indicative of *c*-axis oriented films. This is also highlighted in Fig. 6.1c. As long as the $T_{dep} \geq 700^{o}$C, varying the sputtering ambient from Ar-4% H_2 to Ar-4% H_2+ H_2O to Ar-4% H_2+ O_2 does not significantly influence the epitaxial growth of LMO films. Note that for consistency, XRD data are presented only for an LMO thickness of ~240 nm; however, similar results were obtained for the other thickness levels studied.

It is also important to mention that due to the hygroscopic nature of the MgO surface, samples from each template were pre-annealed at the deposition temperatures for approximately 30 min to 40 min to remove any adsorbed H_2O and hydrocarbons. This ensures a chemically clean surface for the reproducible growth of subsequent LMO layers.

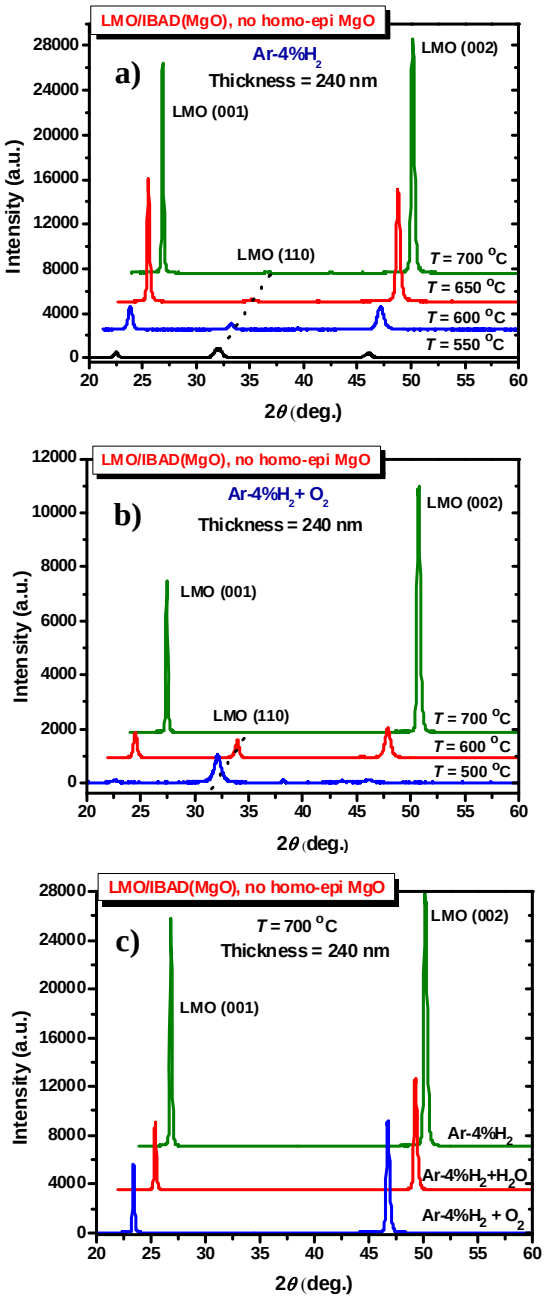

Figure 6.1: A series of XRD θ-2θ scans for 240 nm thick LMO films deposited directly on IBAD-MgO templates at various temperatures (a) in forming gas and (b) in a mixture of forming gas and oxygen ambient. (c) θ-2θ scans of LMO prepared in different sputter environments, revealing *c*-axis growth behavior at $T_{dep.}$ = 700°C.

In fact, information concerning crystalline quality of the surface before and after the pre-anneal was obtained from reflection high-energy electron diffraction (RHEED) analysis as shown in Fig. 6.2. The images taken at ambient temperature displayed an amorphous surface, in that a halo-like RHEED pattern was observed. Upon annealing IBAD-MgO and homo-epi MgO templates at the deposition temperatures, the halo pattern transformed into well-defined elongated streaks indicating an atomically smooth, two dimensional epitaxial, and in-plane textured films. This information implies that there is essentially no particular reason to expect significant differences in the growth characteristics of LMO on either template. In fact, similar XRD observations also apply to LMO deposited on homo-epi MgO layers, except that the *c*-oriented epitaxy develops at relatively lower temperatures (~ 50^{o}C) than those attained directly on IBAD-MgO. As documented previously, this can be explained by the deviation of the IBAD-MgO lattice parameter (0.43-0.44 nm) from that of the homo-epi MgO (0.421 nm) [57], where the lattice mismatch of LMO with respect to IBAD-MgO is larger than that for the latter (~ 9-11% versus ~ 7%, respectively). This necessitates relatively higher growth kinetics to obtain *c*-axis oriented epitaxy directly on IBAD-MgO. It is noteworthy that, although the surface lattice parameter of IBAD-MgO deviates from that of bulk MgO, once the processing conditions were optimized (i.e., T_{dep} = 700^{o}C in Ar-4% H_2) we find that LMO heteroepitaxy is relatively insensitive to these small differences in the lattice parameter. In contrast, a homo-epi MgO layer is generally needed for the epitaxial growth of SRO and STO cap layers on IBAD-MgO,

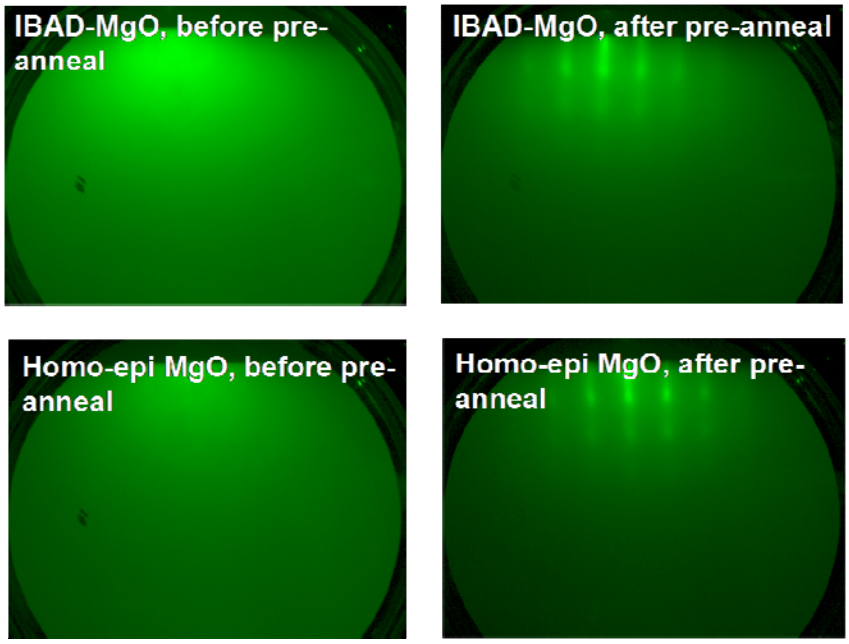

Figure 6.2: RHEED analysis for IBAD-MgO and homo-epi MgO templates before and after pre-annealing.

since it reduces the possibility of strain related misorientations occurring in these cap layers by restoring the lattice parameter of MgO to its bulk value. Apparently, the observed insensitivity of LMO growth characteristics with respect to either IBAD-MgO or homo-epi MgO templates also suggest that the LMO is more tolerant of lattice mismatch induced strain than both the SRO and STO counterparts. This result is actually quite remarkable in that the epitaxial LMO films can be grown reproducibly in a variety of deposition atmospheres, making it a robust and a reliable cap layer. Results also corroborate the established properties/advantages of LMO deposited on homo-epi MgO templates over other buffer layer systems that have been considered for IBAD architectures [56].

The epitaxial relation and the crystallographic alignment of LMO films on the substrates were determined by XRD texture analysis. All samples with LMO thicknesses ranging from 30 nm to 240 nm gave four equally spaced in-plane LMO (111) reflections, separated by 90^{o}, indicating single domain oriented and cube-on-cube films as shown in Fig. 6.3.

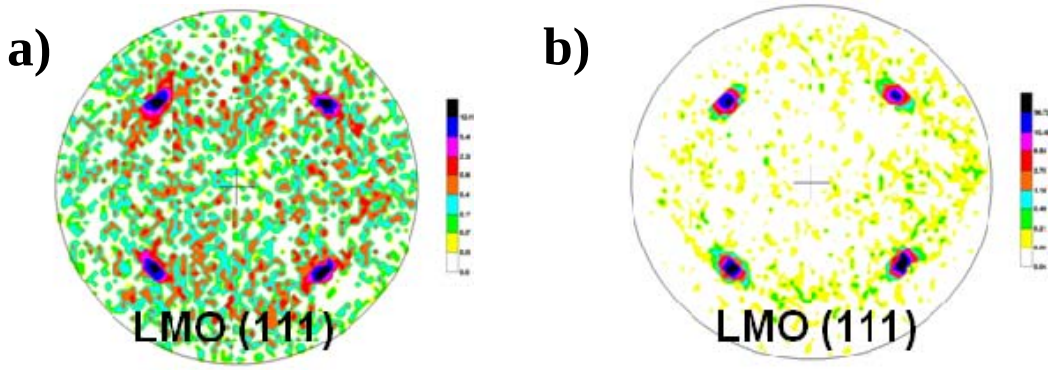

Figure 6.3: Pole figures of LMO films at a) 30 nm and b) 240 nm thickness, deposited directly on IBAD-MgO templates.

From X-ray studies, the in-plane (ϕ-scan) and out-of-plane (ω-scan) full width at half maximum (FWHM) peak-width distributions are presented in Fig. 6.4a as a function of LMO thickness. Again for consistency, we have shown results only for films processed in forming gas and at $T_{dep.}$ = 700^{o}C. The ω-scan and ϕ-scan FWHM ($\Delta\omega$ and $\Delta\phi$) values were obtained using the LMO (002) and (111) peak reflections, respectively. It appears that LMO nucleates with a direct in- and out-of-plane epitaxy, as evidenced by the similar FWHM values compared to the underlying IBAD-MgO template. This is possibly due to the strain, associated with the considerable lattice mismatch between the LMO and MgO, which might not have fully released at the minimum thickness level studied. As the film grows, texture improves with less direct epitaxial match. While the out-of-plane texture stays nearly unchanged, the in-plane texture appears to improve with an increase in LMO thickness. The $\Delta\phi$ values start at 7.8^{o} for 30 nm films and decrease to 5.8^{o} for 240 nm films. To understand this improvement in general, one should take into consideration the grain growth with the increase in film thickness. Indeed, for the LMO case, this phenomenon can be visually seen from the AFM images presented below. Hence, we speculate that LMO film may help to smooth surface irregularities of the IBAD-MgO template, which becomes progressively more effective as the LMO thickness increases. This in turn probably leads to the observed improvement in $\Delta\phi$. In fact, the present observation is in accordance with a previous report on $SrRuO_3$ (SRO) cap layers, where a surface planarization was realized when deposited on homo-epi MgO layers [64, 65].

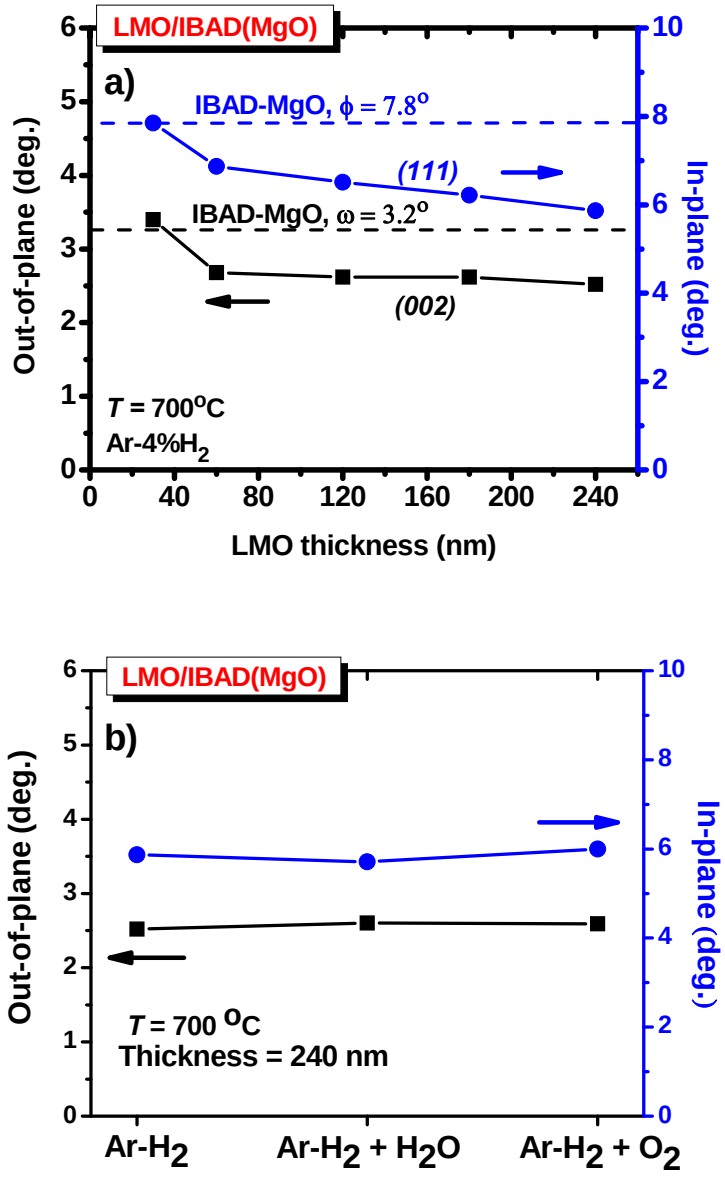

Figure 6.4: Out-of-plane and in-plane textures of LMO films grown directly on IBAD-MgO (without homo-epi MgO) with respect to (a) different film thicknesses and (b) various sputtering gas mixtures.

However, in contrast to the case with SRO, improvements in $\Delta\phi$ did not directly translate into a systematic texture improvement for the YBCO, a finding that is discussed below. This difference may arise from the use of a better ($\Delta\phi < 8^{o}$) in-plane textured IBAD-MgO template in the present study. On the other hand, for a given LMO thickness, e.g., 240 nm, different sputtering gas compositions do not greatly influence the in-plane and out-of-plane textures of LMO layers (Fig. 6.4b).

In addition, LMO films exhibit a smoother surface microstructure compared to the underlying substrate. Figures 6.5a and 6.5b show 3 μm × 3 μm area AFM images for 30 and 240 nm-thick LMO films deposited directly on IBAD-MgO templates, respectively. While both images reveal a dense, crack-free microstructure with narrow distribution of nano-scaled growth nuclei, the surface root-mean-square roughness (R_a) increases from 0.48 nm to 1.34 nm with an increase in LMO thickness from 30 nm to 240 nm. For intermediate film thicknesses, this behavior can be clearly seen from Fig. 6.5c. Consistent with the AFM images, the observed increase in surface roughness is likely associated with the growth of larger LMO grains as the film becomes thicker. Note that even though the surface is becoming progressively rougher with increasing film thickness, which may seem to be contradictory with the planarization argument, the R_a of even the thickest film still lies below the surface roughness of the starting IBAD-MgO template (R_a = 1.94 nm). In addition, the LMO roughness does not affect the superconducting performance of the YBCO films, as discussed later.

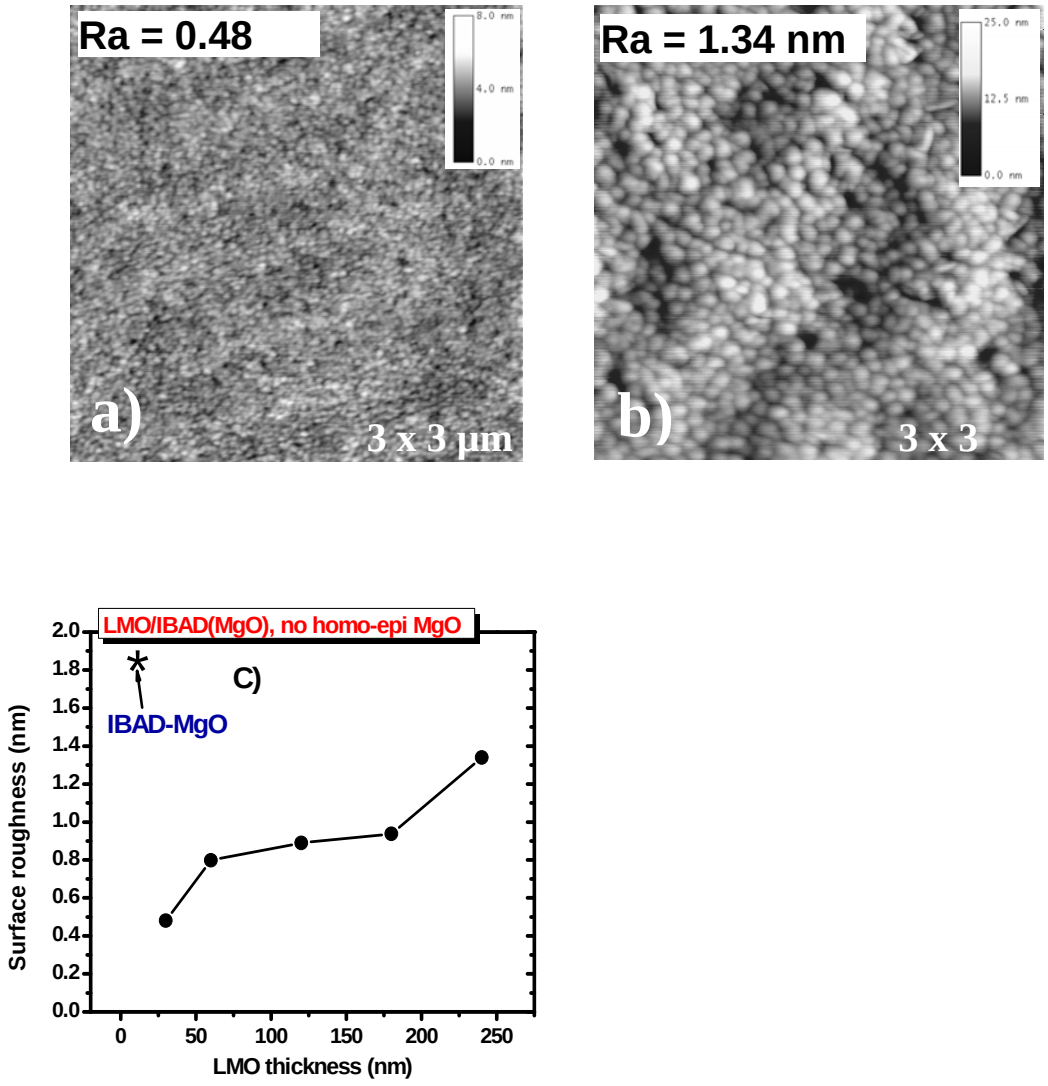

Figure 6.5: AFM surface morphology of (a) 240 nm thick, (b) 30 nm thick LMO coated films on IBAD-MgO templates (without homo-epi MgO), and (c) the variation of surface roughness with the film thickness.

In addition to AFM images, the relatively featureless SEM images of LMO films on IBAD-MgO templates have confirmed that LMO films have dense and crack-free surface as shown in Fig. 6.6. Moreover, a closer examination of SEM images reveals that 30 nm and 240 nm thick LMO films have similar microstructures.

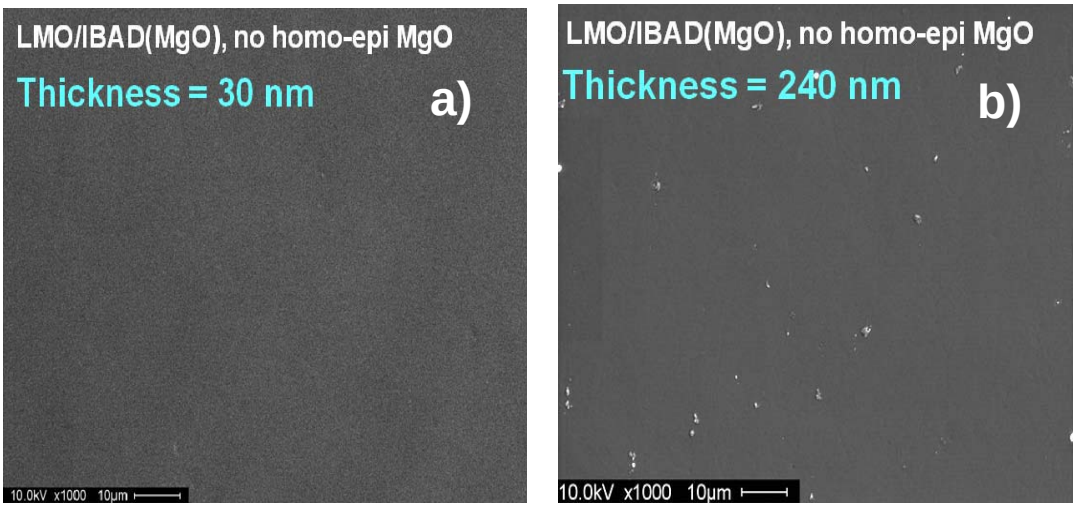

Figure 6.6: Typical SEM surface morphology of (a) 30 nm thick and (b) 240 nm thick LMO films on the IBAD-MgO templates (without homo-epi MgO)

The performance of the LMO/IBAD-MgO samples is qualified by depositing 1 μm thick YBCO coatings by PLD. Typical XRD θ-2θ diffraction patterns of YBCO films deposited on either LMO buffered homo-epi MgO/IBAD (MgO) or IBAD (MgO) templates are shown in Fig 6.7. The strong (*00l*) reflections (and absence of others) from YBCO indicated good *c*-axis alignment of the YBCO films.

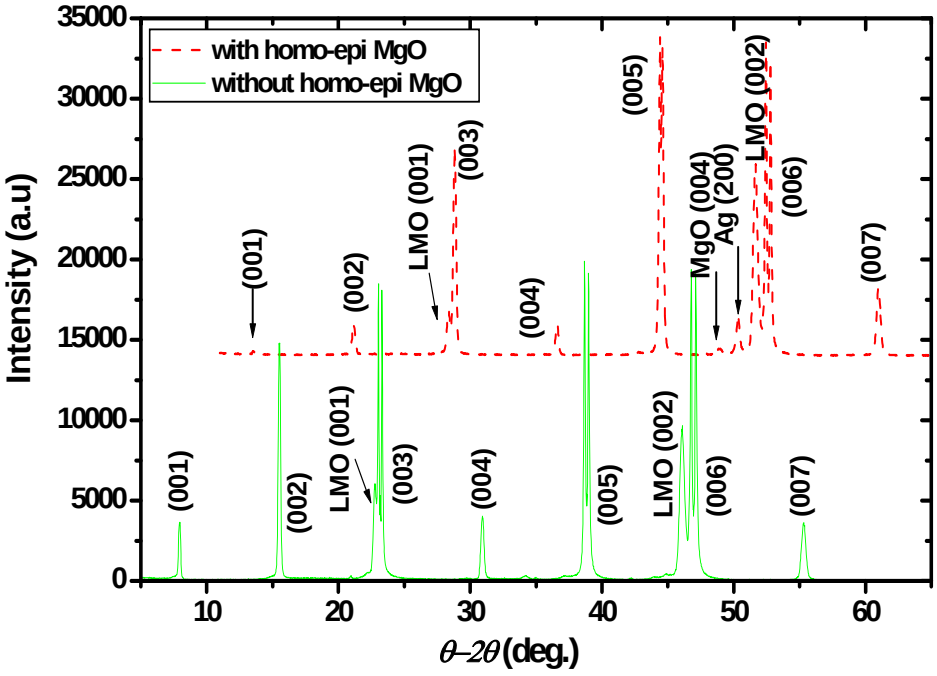

Figure 6.7: A typical θ-2θ scan for 1 μm-thick PLD YBCO films grown on $LaMnO_3$ buffered simplified and standard IBAD architectures. YBCO films have a preferred *c*-axis orientation. Note that, due to absence of homo-epi layer (the bottom scan) it is difficult to distinguish the MgO peak reflection at this level of display.

To confirm the epitaxial growth and crystallinity of YBCO on LMO/IBAD-MgO, ω-scan and ϕ-scan measurements were carried out using (005) and (102) peak reflections of YBCO. The results are shown in Fig. 6.8 for various thickness levels of LMO. Evidently, as mentioned earlier, there is no systematic trend in peak width distributions with respect to the LMO thickness, even for the thinnest LMO films. The FWHM values are found to be between 1.2°-1.6° for the out-of-plane and 2.8°-3.0° for the in-plane textures, an improvement of ~ 3°-5° for the latter compared to $\Delta\phi$ of LMO.

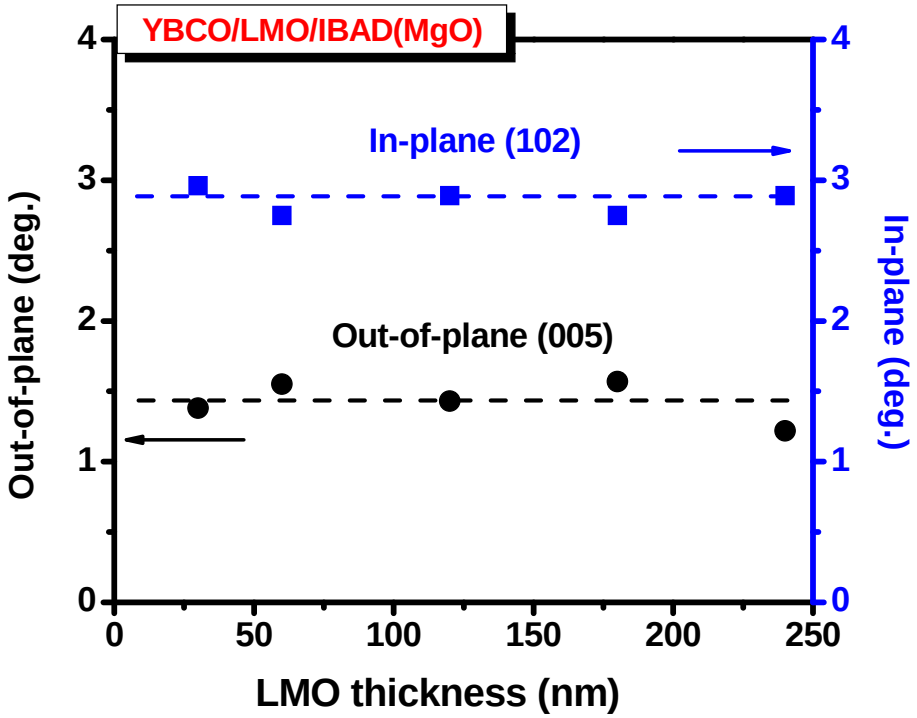

Figure 6.8: Out-of-plane and in-plane scan FWHM values of YBCO films with respect to different LMO cap layer thickness.

To understand whether the observed improvement in $\Delta\phi$ only takes place for thick (1 μm) YBCO films (due to the grain growth considerations), we have deposited thin (150 nm) YBCO films on 30 nm and 240 nm thick LMO layers. Consistently similar degrees of improvements were obtained in the texture of these thin YBCO coatings as well. Hence, we reason that the improved FWHM values are in part due to the highly anisotropic, rapid basal-plane film growth nature of YBCO films [88] and in part due to the suggested surface planarization effect of LMO layers. Apparently, the in-plane improvement must have occurred at an earlier stage. However, further studies are needed to clarify the mechanism.

Similarly, SEM investigations revealed that the thickness of the LMO layer, when deposited directly on IBAD-MgO, does not have a significant effect on the surface morphology of the YBCO films. This point is illustrated in Figs. 6.9a and 6.9c, for samples having 30 and 240 nm thick LMO layers, respectively. For comparison, Figs. 6.9b and 6.9d are included, showing the SEM microstructures for the YBCO films deposited on LMO/homo-epi MgO/IBAD-MgO architectures. Two key points are these: (1) the YBCO films, irrespective of LMO thickness, exhibit a homogeneous and dense surface morphology, and (2) the microstructural characteristics are similar for YBCO deposited on either LMO/IBAD-MgO or LMO/homo-epi MgO/IBAD-MgO templates. (Note that the presence of some small particulates on the surfaces is typical for PLD YBCO films [89] and they have no adverse effect on the structural and superconducting properties of the samples.)

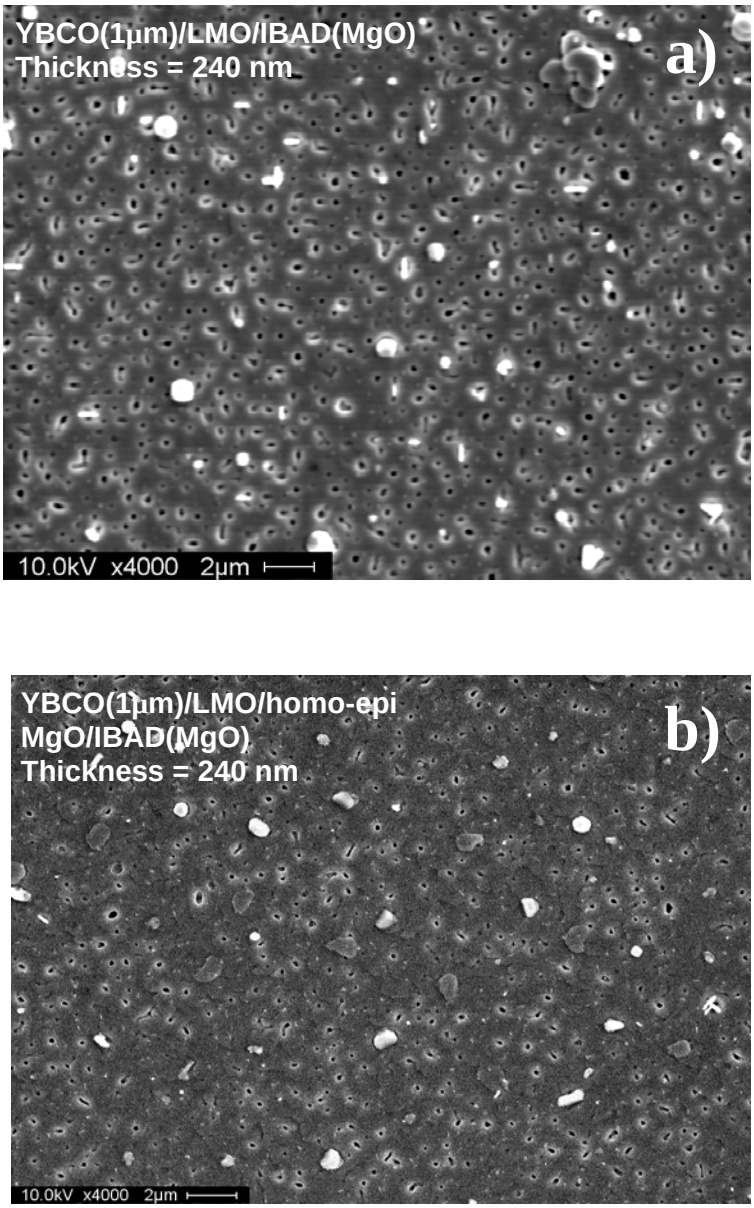

Figure 6.9: Typical SEM surface morphology of 1 μm-thick YBCO films grown on (a) 30 nm thick and (b) 240 nm thick LMO coated IBAD-MgO templates (without homo-epi MgO); (c) and (d) corresponding surface morphologies of YBCO films on the standard LMO/homo-epi MgO/IBAD-MgO architectures having the same thickness LMO layers, respectively.

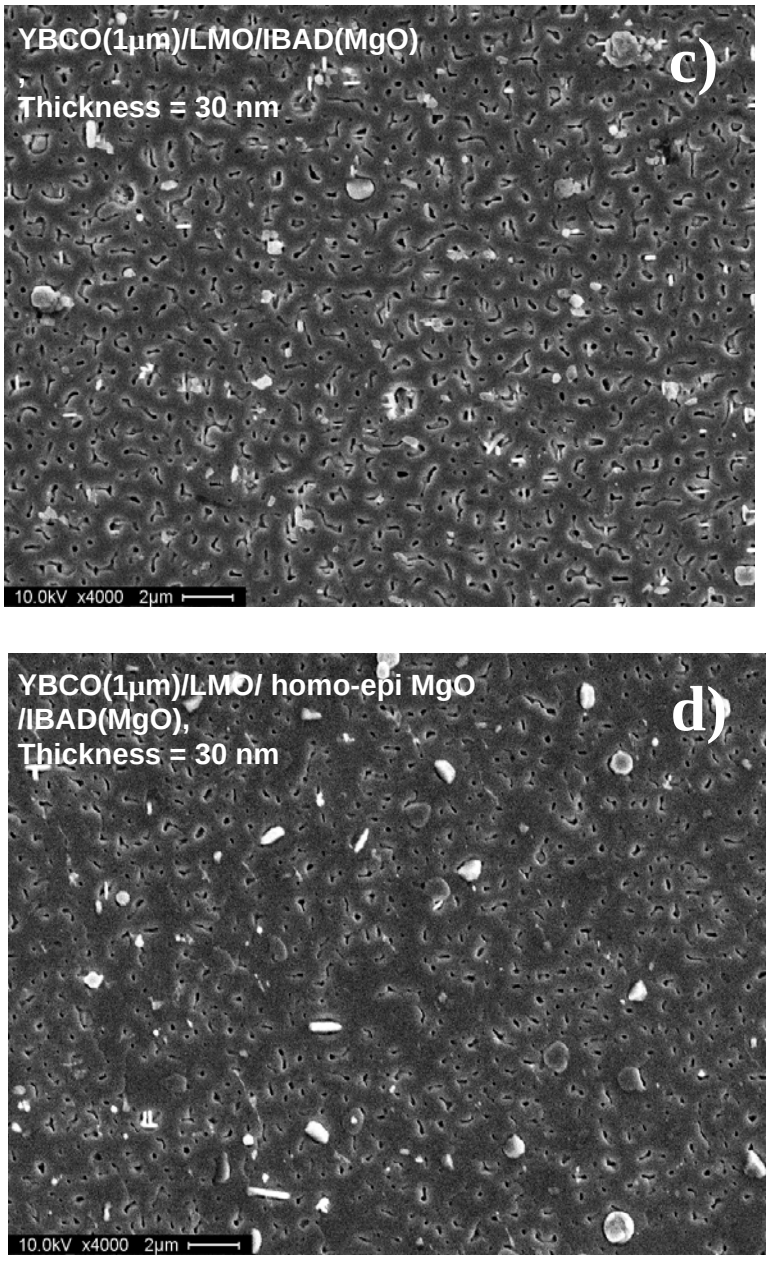

Figure 6.9 continued

Figure 6.10 shows cross-sectional HRTEM images of the standard buffer layer architecture and two examples with simplified architectures (having 30 and 240 nm LMO layers). For each case, insets show key interfaces at higher magnification. In Fig. 6.10a, a standard IBAD-MgO stack containing a 30 nm-thick LMO cap layer is shown. The interfaces between YBCO and LMO and also between LMO and MgO are flat and clean, without any indication of interfacial reaction. It is clear that YBCO growth is epitaxial and the interface between LMO and MgO is of high quality. Now, comparison of Fig. 6.10a with the simplified (no homo-epi MgO) IBAD architectures (Fig. 6.10b and 6.10c), reveals similar microstructural properties. Figures 6.10b and 6.10c show cross-sectional HRTEM images of simplified architectures having two different LMO layer thicknesses of 30 nm and 240 nm, respectively. For both thickness of LMO (Figs. 6.10b and 6.10c), the interfaces among all layers are clean and coherent with no evidence of reactions between the LMO and IBAD-MgO.

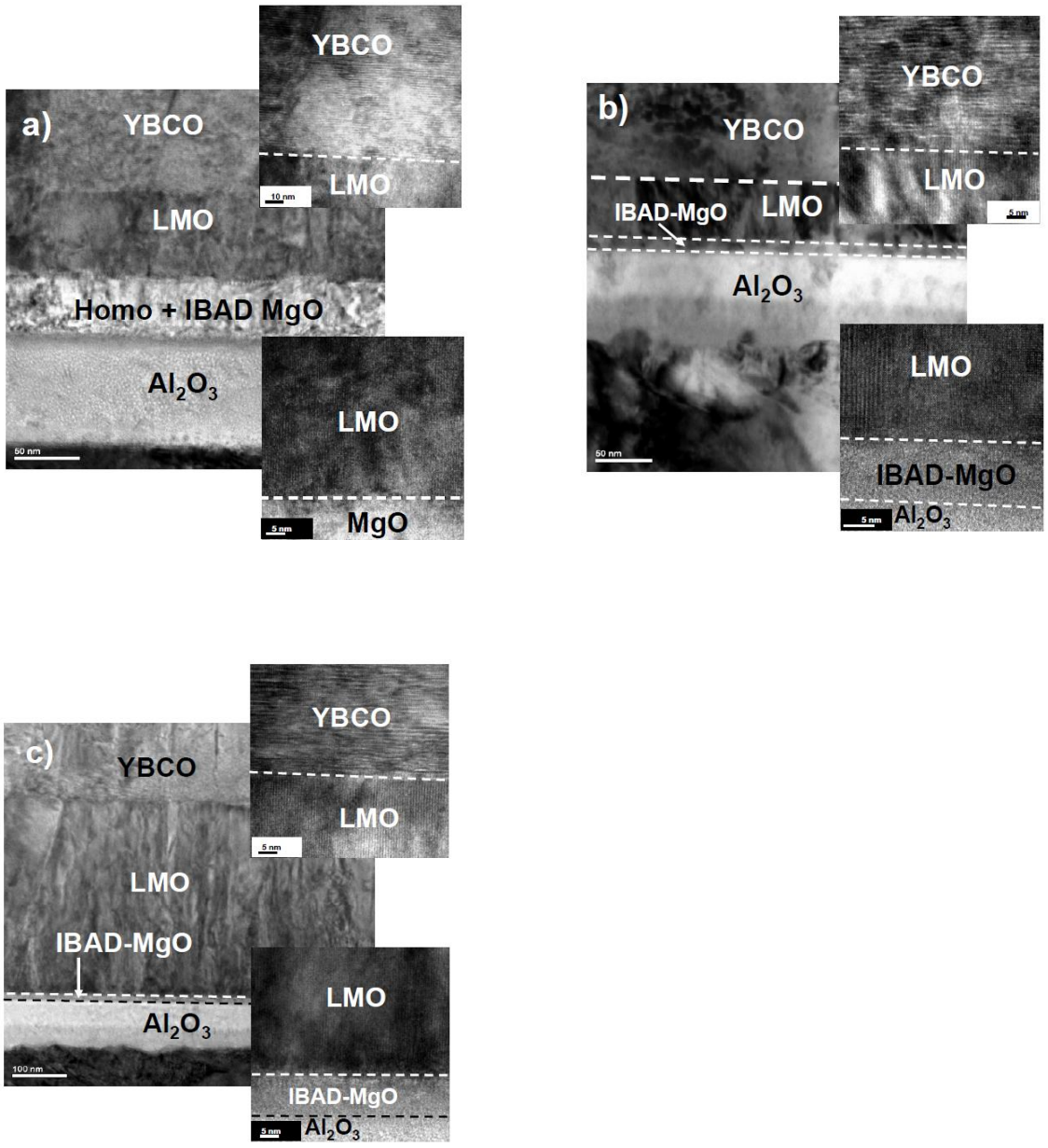

Figure 6.10: Cross-sectional TEM images of PLD-YBCO films on a) LMO (30 nm)/homo-epi MgO/IBAD- (MgO), b) LMO (30 nm)/IBAD (MgO) and c) LMO (240 nm)/IBAD-MgO templates. The insets show the interfaces between YBCO and LMO as well as LMO and homo-epi MgO and IBAD-MgO; the microstructures of three samples are similar.

To confirm this, EDS line scans were conducted across the entire thickness of the samples shown in Figs. 6.10a and 6.10c. An electron probe of approximately 1.5 nm diameter was used. The results, shown in Fig. 6.11, reveal well-resolved interfaces and sharp changes in the signals for the Y, Mn, Mg, Al, Ni, and, Cr. This gives further evidence that no significant intermixing takes place. Apparently, whether there is homo-epi MgO layer or not, the diffusion of substrate cations is blocked by the Al_2O_3, confirming the effectiveness of Al_2O_3 as a good cation diffusion barrier. Moreover, line scans also underscore the prospect of only 10 nm thick IBAD-MgO templates for the growth of high quality LMO films. Among finer details, we note that the observed dip in the Y signal at the Y_2O_3 layer (see Fig. 6.11a) is because of the line scan crossing a "hole" formed by the ion beam damage during sample preparation. It also appears that small amounts of Cr and Mn (that are contained in the Hastelloy) are either segregated to the substrate surface during the processing of buffer and HTS layers or they happened to be initially present at the surface. Overall, these TEM analyses imply two important points: (i) high-quality epitaxial films of LMO can be grown directly on IBAD (MgO); (ii) the quality of subsequent YBCO films does not significantly depend on LMO layer thickness and is similar to those grown on standard IBAD architectures. In fact, it has also been shown in ref. [90] that the performance of YBCO films is not affected by the thickness of LMO layers. The present results, together with those reported previously [90], underscore the strong potential of LMO to serve as a single cap layer directly on IBAD (MgO).

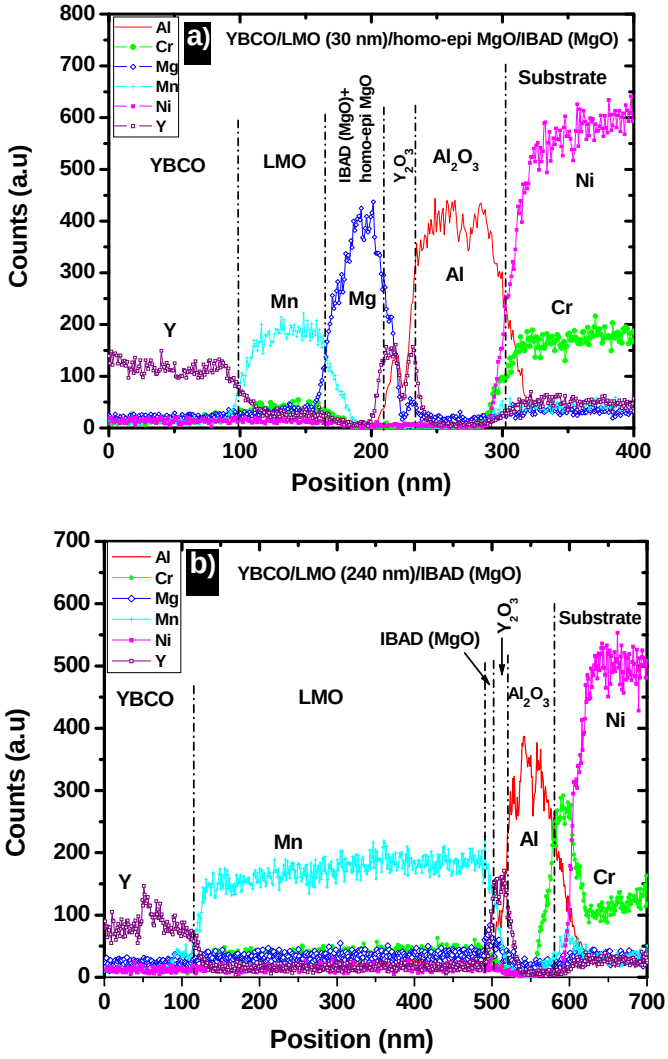

Figure 6.11: EDS analysis of Y, Mn, Mg, Al, Cr and Ni in a) YBCO/LMO/homo-epiMgO/IBAD(MgO)/Y_2O_3/Al_2O_3, b) YBCO/LMO/IBAD (MgO)/Y_2O_3/Al_2O_3 multilayer film stacks on the Hastelloy. The signals corresponding to Y represent YBCO and Y_2O_3; Mn, Mg, and Al represent $LaMnO_3$, MgO, Al_2O_3 layers, respectively. The substrate signals are represented by the Ni and Cr signals.

We now discuss the electrical properties of these samples. The transport critical current density J_c values were assigned at a 1 μV/cm electric field criterion. The self-field J_c performance of the YBCO films at 77 K as a function of LMO thickness is presented in Fig. 6.12. For comparison, data for YBCO films fabricated on LMO/homo-epi MgO/IBAD-MgO are also included. These data are for samples where the LMO films were processed in forming gas. Consistent with the XRD and microstructural observations, practically all samples exhibit excellent self-field J_c values above 2 MA/cm^2 over the entire range of LMO thickness. Small differences in values are due to subtle variations associated with the YBCO deposition conditions, and should not be generalized. The most remarkable attribute of this plot is that the samples on LMO/IBAD-MgO layers show similar performance compared to their counterparts having homo-epi MgO layers. Evidently, a slight increase in the surface roughness of LMO with thickness (see Fig. 6.5c) does not have any adverse effect on the performance of YBCO films. Of greatest interest is the performance of these samples in the presence of substantial magnetic fields.

Figure 6.13a shows the field dependence of J_c for the same samples (one for each LMO thickness) shown in Fig. 6.12, measured at 77 K with the field parallel to the *c*-axis. Shown also in the plot is the corresponding behavior of a typical YBCO film deposited on IBAD template with homo-epi MgO layer. Figures 6.12 and 6.13 clearly demonstrate two key features: the performance of YBCO deposited on our simplified IBAD architecture is highly comparable with that obtained with more complex IBAD templates having homo-epi MgO layers and the in-field J_c performance of the YBCO coatings is

remarkably insensitive to LMO layer thickness. Equally important, the choice of sputtering gas ambient for direct deposition of LMO films does not affect the in-field transport properties of the YBCO coatings (Fig. 6.13b). Clearly, regardless of the conditions used, the minimum self-field J_c values of the samples are around 1.8 MA/cm^2. Finally, all these results underscore the strong potential of LMO as a single cap layer directly on IBAD-MgO for the development of simplified IBAD architecture with reduced cost and high-performance.

We show the angular dependence of J_c (77 K) with respect to the orientation of applied magnetic field at 1 T in Fig. 6.14. When the magnetic field H is oriented parallel to the *ab*-planes, J_c exhibits a sharp peak which is due in part to the intrinsic anisotropy of the YBCO films [91-93] arising from the layered CuO planes. Also contributing to this peak is pinning from other correlated structures oriented parallel to the *ab*-planes, such as stacking faults and/or intergrowths. If the field is oriented near the *c*-axis, a smaller and much broader peak is obtained. This second peak is due to correlated disorder directed near the c-axis, such as threading dislocations, twin boundaries, and grain boundary dislocations. The similarity of the angular dependencies of J_c for the YBCO films on the two different templates suggests that the contributions from correlated and uncorrelated pinning structures are similar in the two materials [94].

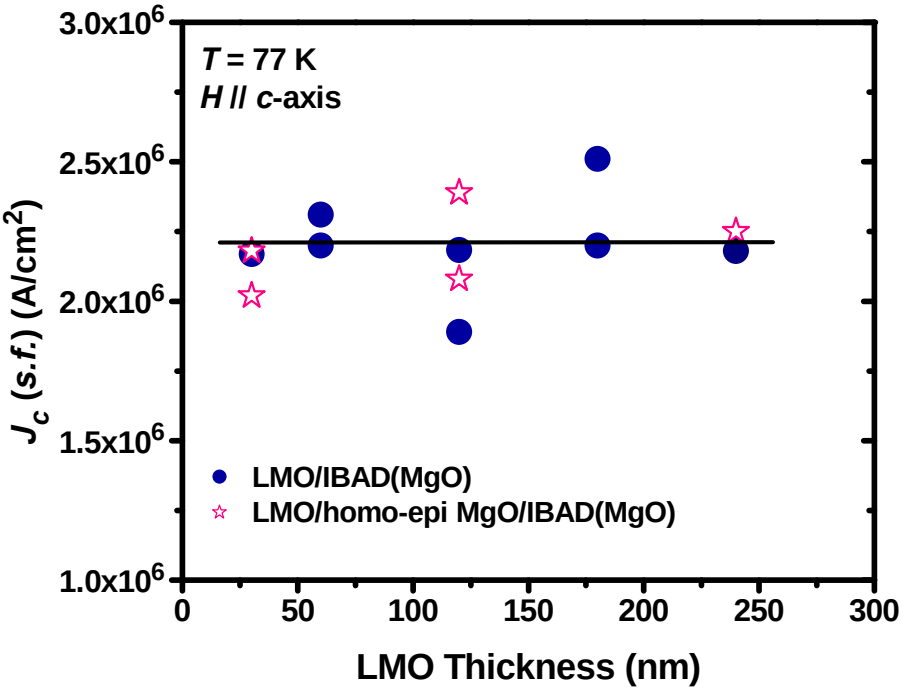

Figure 6.12: Self-field J_c values measured by transport method of YBCO films as a function of LMO thickness. For comparison, YBCO films were deposited both on LMO/IBAD-MgO and LMO/homo-epi MgO/IBAD-MgO architectures.

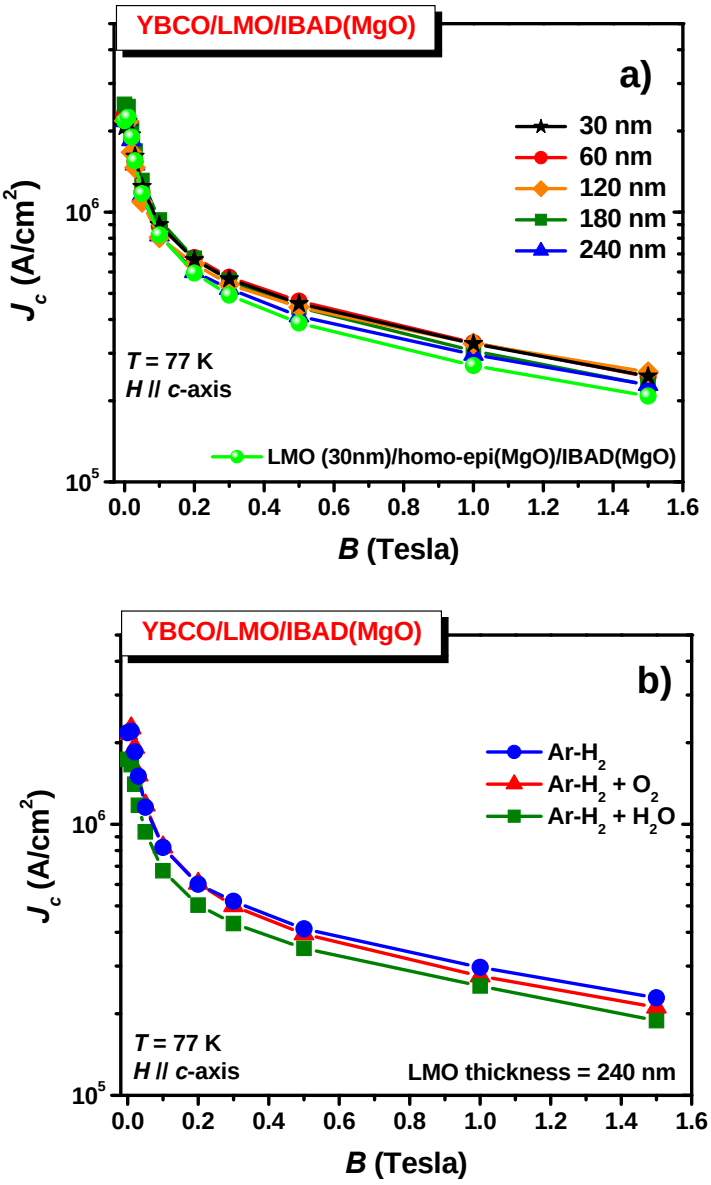

Figure 6.13: (a) Semi-log plot of J_c at 77 K as a function of magnetic field for the same samples presented in Fig. 6.12. The figure compares results for samples having different LMO layer thicknesses as well as J_c results for a typical YBCO/LMO/homo-epi MgO/IBAD-MgO architecture, where the LMO thickness is 30 nm. (b) A plot of the field dependence of J_c for YBCO films grown on 240 nm thick direct LMO coatings that were processed in various sputtering atmospheres.

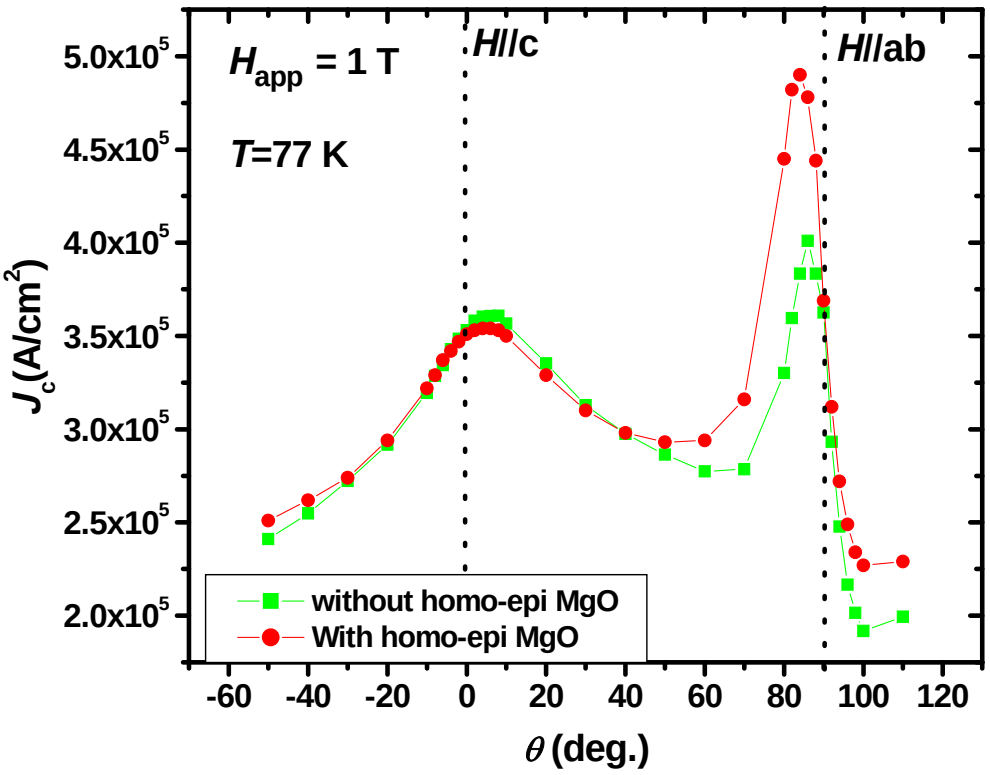

Figure 6.14: Angular dependence of J_c for YBCO films deposited on either LMO/IBAD (MgO) or LMO/homo-epi MgO/IBAD (MgO) architectures. The two samples exhibit similar pinning features.

6.2 Pinning Enhancements in REBCO Films via Template Surface Modifications

6.2.1 Nanostructured Composite $LaMnO_3$:MgO Cap Layer Development

The discovery of ceramic type high temperature superconducting materials in 1986 [2], which exhibit superconductor properties at liquid nitrogen boiling temperature, has triggered broad research into material characterization, development, and fabrication. Particularly, $YBa_2Cu_3O_{7-\delta}$ (YBCO)-based superconducting wires, coated conductors (CCs), are one of the most exciting advancements in high temperature superconductivity. Developing coated conductors will promote practical applications such as motors, generators, and transmission lines. For operation in such power utility applications, a challenge is the requirement to maintain high critical current density, J_c, under high magnetic field strengths and field orientations. As discussed from first principles in Chapter 2.2, this requirement means that the quantized magnetic flux lines (vortices) in the high temperature superconducting (HTS) material must be immobilized through nanoscale materials defects. Even though HTSs have many natural pinning defects, e.g., oxygen/cation vacancies, grain boundaries, dislocations, voids, etc, it has recently been shown that artificially introduced pinning centers are much more effective to enhance J_c in high magnetic fields and at high temperatures [95]. Hence, over the past several years, extensive investigations have been conducted to incorporate a variety of artificial pinning defects in YBCO matrix through nanostructure engineering and manipulation. Many different methods have been used. These include creation of three dimensional, self-

assembled columnar structures of nonsuperconducting nanoparticles such as $BaZrO_3$ [28, 29, 96] and $BaSnO_3$ [32] in the YBCO matrix; multilayering of YBCO with second phase Y_2BaCuO_5 [31], CeO_2 [97, 98], or Y_2O_3 [99]; and doping with rare-earth elements [33-37]. A common attribute of all these methods is that the nanostructural manipulation transpires within the YBCO matrix. Following the initial work of Crisan et al. [39] to increase J_c in Tl-based cuprate superconductors, we have recently demonstrated an indirect, but effective route to introduce growth-induced flux pinning defects in YBCO films, whereby substrate surfaces are decorated with a variety of nanoparticles prior to YBCO deposition [30, 38, 39, 40]. This previous work, along with the widespread and ongoing research on strain-mediated growth of two-phase heteroepitaxial nanocomposite films for semiconductor device applications [100-108], motivated the present study. Here, we have investigated the efficacy of pinning enhancements in YBCO films through development of mixed phase $LaMnO_3$:MgO (LMO:MgO) composite cap buffer layers on ion beam assisted deposition MgO substrates (IBAD-MgO) [56]. Recently, the viability of depositing phase-separated LMO:MgO composite films was reported using pulsed laser deposition (PLD) on the fully buffered IBAD-MgO substrates [109]. In the present work, we have used sputter deposition, a far more scalable deposition technique than PLD, to show formation of chemically phase separated, but at the same time structurally self-assembled MgO nanocolumns within the LMO layer. Upon YBCO film deposition, these second phase nanocolumns nucleate growth defects that retard dissipative vortex motion and enhance in-field J_c performance.

Presently, commercially available tapes of the IBAD-MgO multilayer architecture consist of LMO/homo-epitaxial MgO/IBAD-MgO/Y_2O_3/Al_2O_3/Hastelloy [56, 62]. In the previous section of this chapter, we reported that the IBAD architecture can be "simplified" by eliminating one of these layers (homo-epitaxial MgO), by directly depositing LMO on the IBAD-MgO templates [90, 110]. In the following, we present results to show that the standard LMO buffer layers might be further functionalized to serve as a simplified template for the epitaxial growth of YBCO films with enhanced performance.

The crystalline structure and texture of LMO:MgO composite films were investigated by employing detailed XRD measurements. Figure 6.15 exhibits θ-2θ XRD scans for a series of LMO:MgO layers containing 5 vol%, 25 vol% and 50 vol% MgO deposited directly on IBAD-MgO templates. Depositions were carried out in Ar and O_2 gas mixture at a substrate temperature of 720^{o}C. It is clear from Figure 6.15 that the MgO percentage does not affect crystalline structure of composite cap layers. All films exhibited (00*l*) and additional Ni alloy (111) peak reflections which indicate that the films possess good c-axis orientation. MgO peak reflections can not be distinguished from the IBAD-MgO templates, which preclude differentiating the MgO peak reflections from the substrate material.

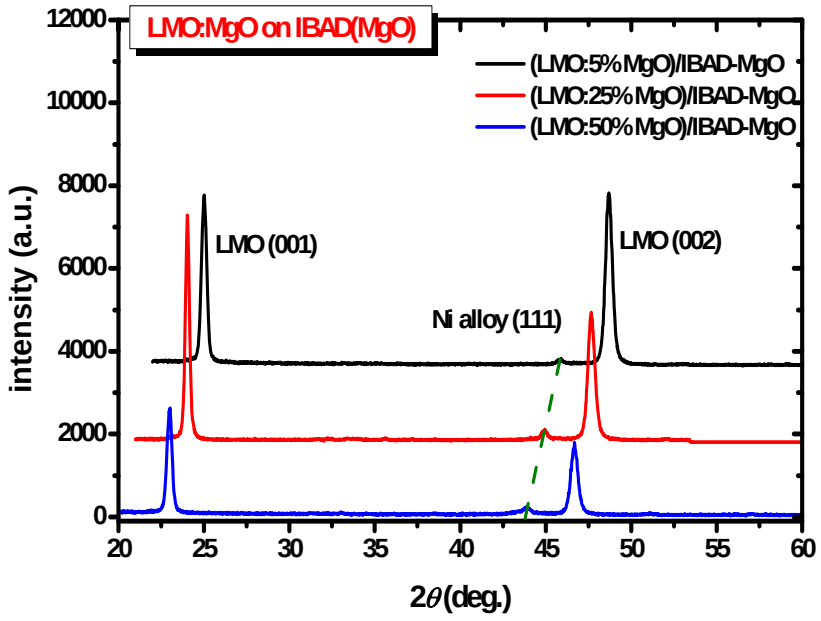

Figure 6.15: A series of XRD θ-2θ scans for composite LMO:MgO films deposited directly on IBAD-MgO templates at various MgO vol. percentages.

Epitaxial orientation of the LMO buffer layers was established by XRD pole figure analysis. We show in Figs. 6.16a and 6.16b typical pole figure data for LMO:MgO films (on IBAD-MgO) having two extreme MgO concentrations of 5 vol% and 50 vol%, respectively. Both of the background-subtracted logarithmic scale LMO(111) pole figures indicate single cube-on-cube epitaxy, with LMO:MgO[001]//substrate[001] and LMO:MgO[110]//substrate[110]; however, the 50 vol% MgO sample clearly shows increased background signal that signifies a reduced epitaxially aligned phase fraction. Nevertheless, we observed comparable in-plane (φ-scan, $\Delta\varphi$) and out-of-plane (ω-scan, $\Delta\omega$) full width at half maxima (FWHM) for the cube textured LMO:MgO grains ($\Delta\varphi$ = 7.6-7.2^o, $\Delta\omega$ = 3.4-3.3^o). These distribution widths are comparable to those of the underlying substrate ($\Delta\varphi$ = 7.8^o, $\Delta\omega$ = 3.2^o).

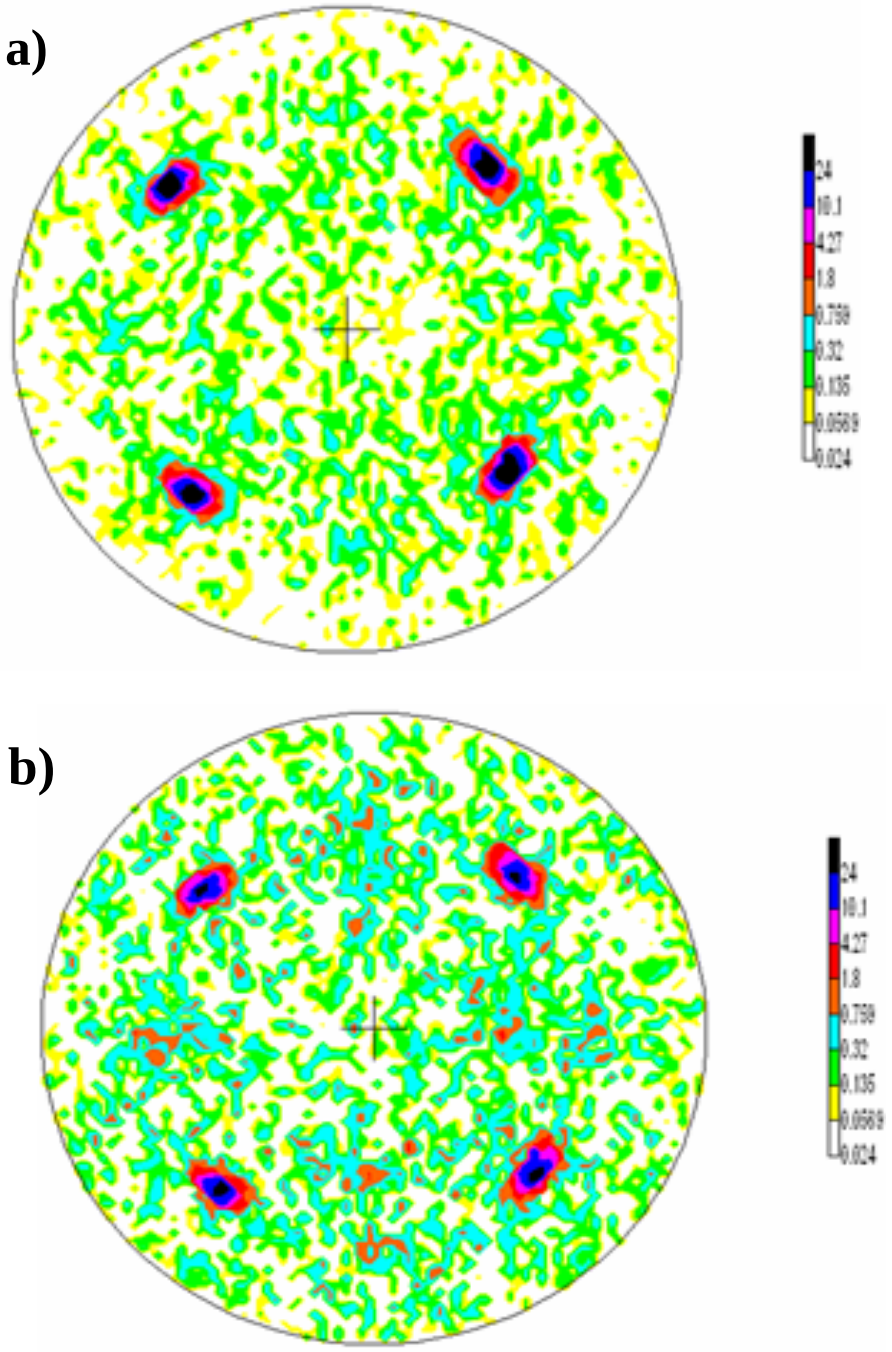

Figure 6.16: The background subtracted logarithmic scale (111) pole figures of LMO:MgO composite films fabricated on IBAD-MgO templates. Films modified with MgO volume percentages of a) 5% and b) 50%.

The surface microstructure of the composite films was examined by SEM after being lightly sputter etched with Ar ions (removing approximately 2-5 nm of material) in order to clean adsorbed atmospheric contaminants and enhance the secondary electron image of the phase segregated regions. A typical SEM image is shown in Fig. 6.17 for a LMO:MgO (25 vol%) film, displaying a high density of bright features with an average diameter of 20 nm. By scanning Auger microanalysis, these features were identified as Mg-rich regions and indicate two-dimensional projections of chemically phase separated, vertically ordered stacks of MgO nanoparticles in the composite film (details discussed below).

Auger elemental maps of the composite LMO:MgO films containing different MgO volume percentages on the IBAD-MgO templates are shown in Fig. 6.18a-6.18c. Red and blue colors represent Mg and La elements, respectively. The existences of distinguishable colors in red and blue underline that phase segregated Mg regions exist on the samples' surface. The overall appearance of the colors quite clearly shows the increase in Mg from one sample to the next one. Quantitative numbers from Auger analysis have confirmed that the Mg atomic percentage, 3.4, 11.8 and 19.3%, increases with the MgO volume percentage in the sputter target, 5, 25, and 50 vol%, respectively.

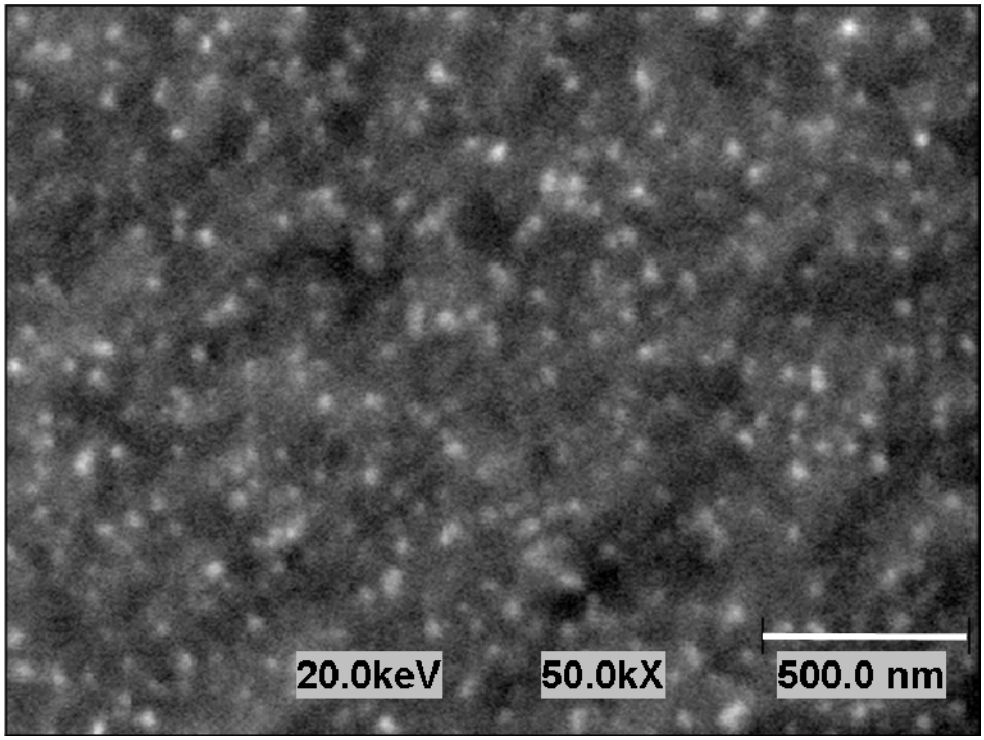

Figure 6.17: Scanning electron micrograph of an LMO:MgO (5 vol%) composite film deposited directly on IBAD-MgO template.

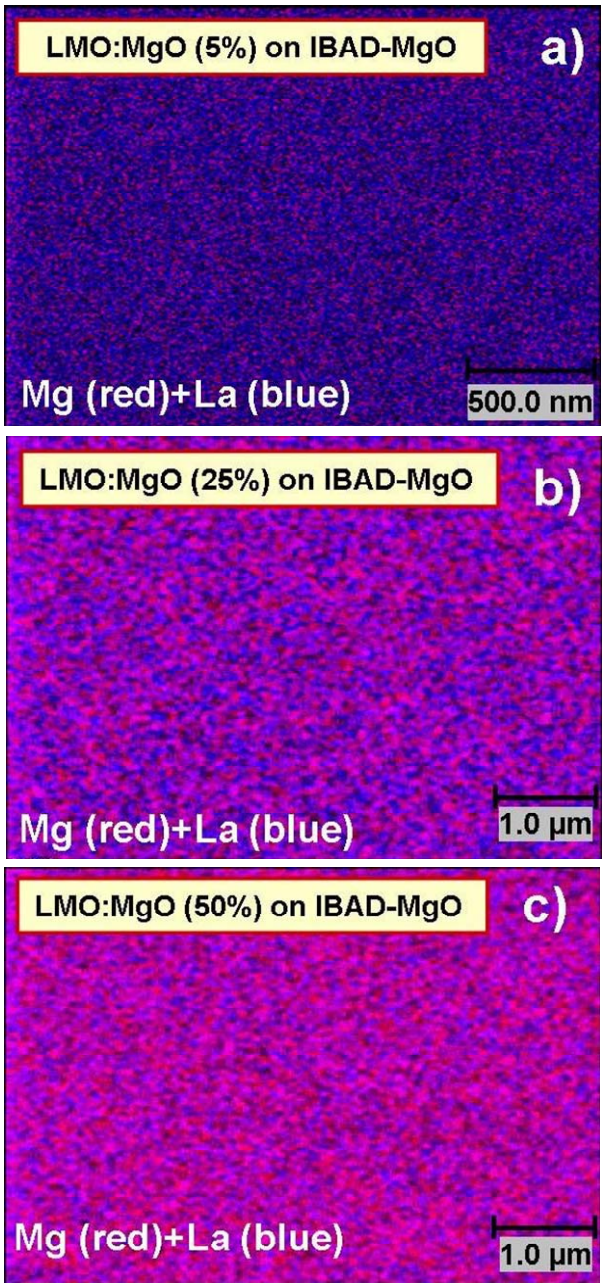

Figure 6.18: Auger elemental map for composite LMO:MgO cap layers on the IBAD-MgO templates containing a) 5 vol%, b) 25 vol% and c) 50 vol% MgO.

The cross-sectional microstructure was evaluated by conventional TEM and Z-contrast microscopy on both IBAD-MgO and homo-epi MgO/IBAD-MgO templates, and for two different concentrations of MgO. The images in Figs. 6.19a and 6.19b display the characteristic Z-contrast STEM images of these composite films deposited on IBAD-MgO templates without and with a homo-epi MgO layer, respectively. For two MgO concentrations (5 vol% directly on IBAD-MgO, 50 vol% on homo-epi MgO), the presence of nearly vertical columnar structures within the LMO matrix can be clearly seen. These columns extend throughout the entire thickness of the composite films. Furthermore, in Z-contrast imaging, a high-Z material appears brighter than a material with lower atomic number Z. Hence, because of the significant difference in Z between Mg(12) and La(57)/Mn(25), the darker contrast regions observed in these images are the MgO phase and the brighter background represents the LMO matrix. It is noteworthy that no such nanostructures have been documented on pure LMO cap films deposited on either IBAD-MgO or homo-epi MgO templates [110]. The corresponding high resolution TEM image of the sample presented in Fig 6.19b is shown in Fig. 6. 19c, revealing that these columns (marked with white arrows) are composed of self-assembled stacks of MgO nanodots that are approximately aligned along the growth direction of the film. The width of the nanocolumns and their average spacing in the micrographs is approximately 5-10 nm and 10-30 nm, respectively.

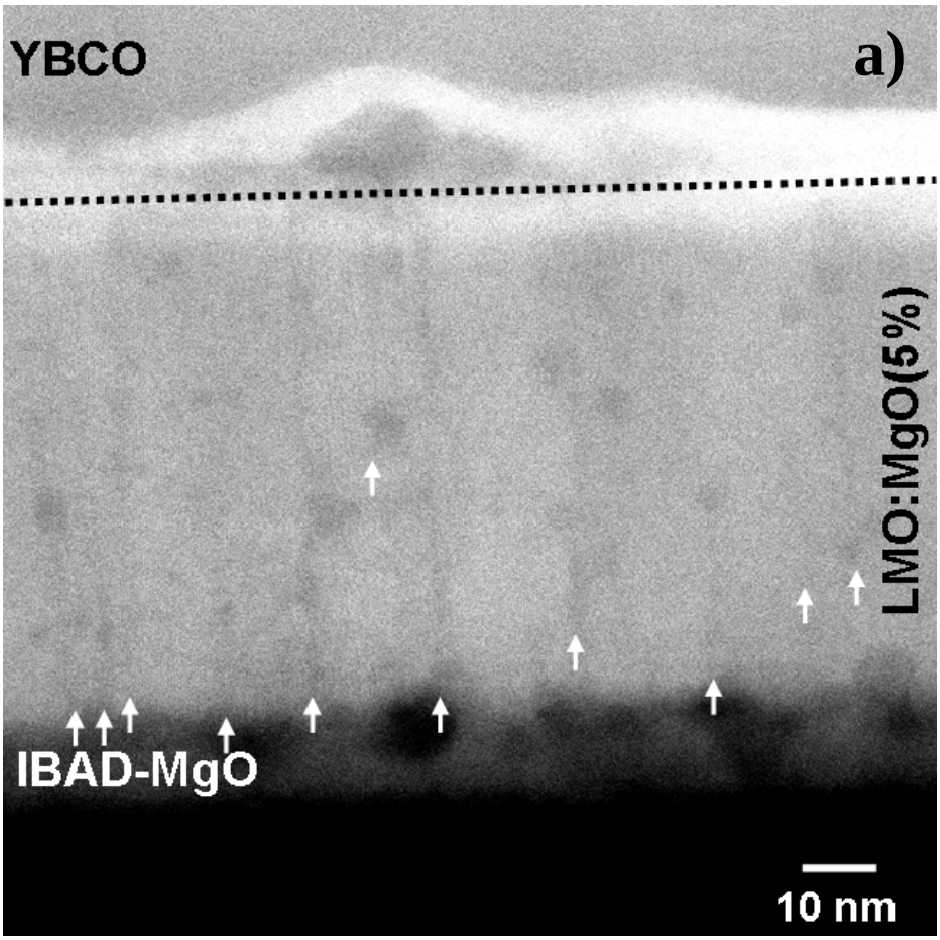

Figure 6.19: Cross-sectional microstructures of the composite cap layers. a) and b) Z-contrast STEM images of LMO:MgO(5%)/IBAD-MgO and LMO:MgO(50%)/homo-epi MgO/IBAD-MgO, respectively, showing the presence of MgO nanocolumns (dark contrast regions; some are marked with white arrows) extending through the thickness of the buffer film matrix. c) Low magnification and d) high resolution TEM images of the YBCO/LMO:MgO interface for the same sample in (b). Origination of additional *c*-axis correlated disorder into the YBCO matrix from the vicinity of the MgO nanocolumns is apparent from the figure. Several of these defective regions are marked with dashed ovals.

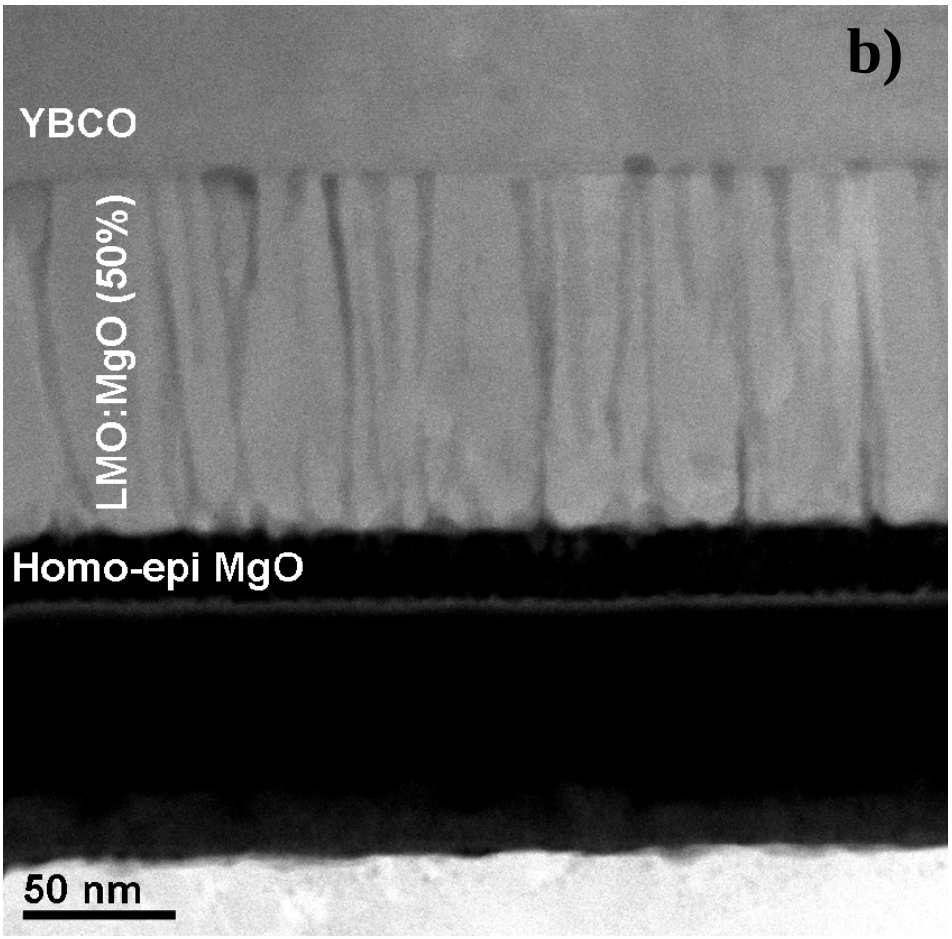

Figure 6.19 continued

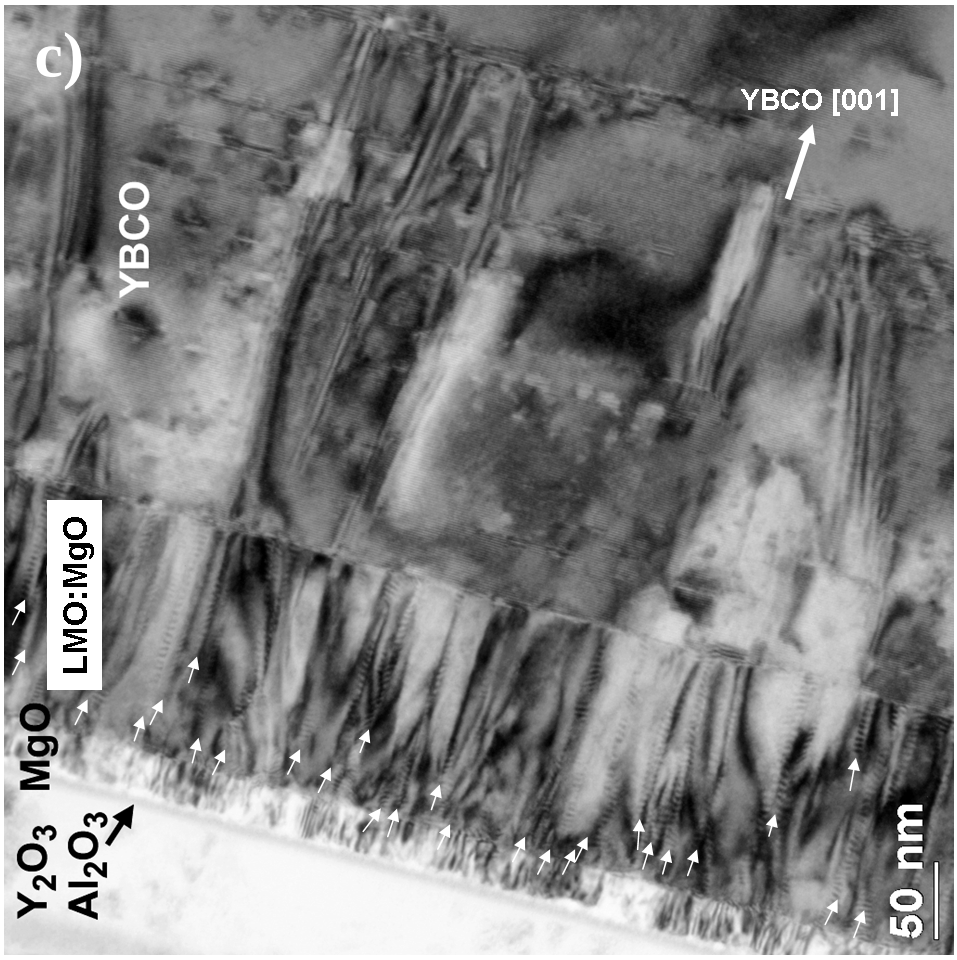

Figure 6.19 continued

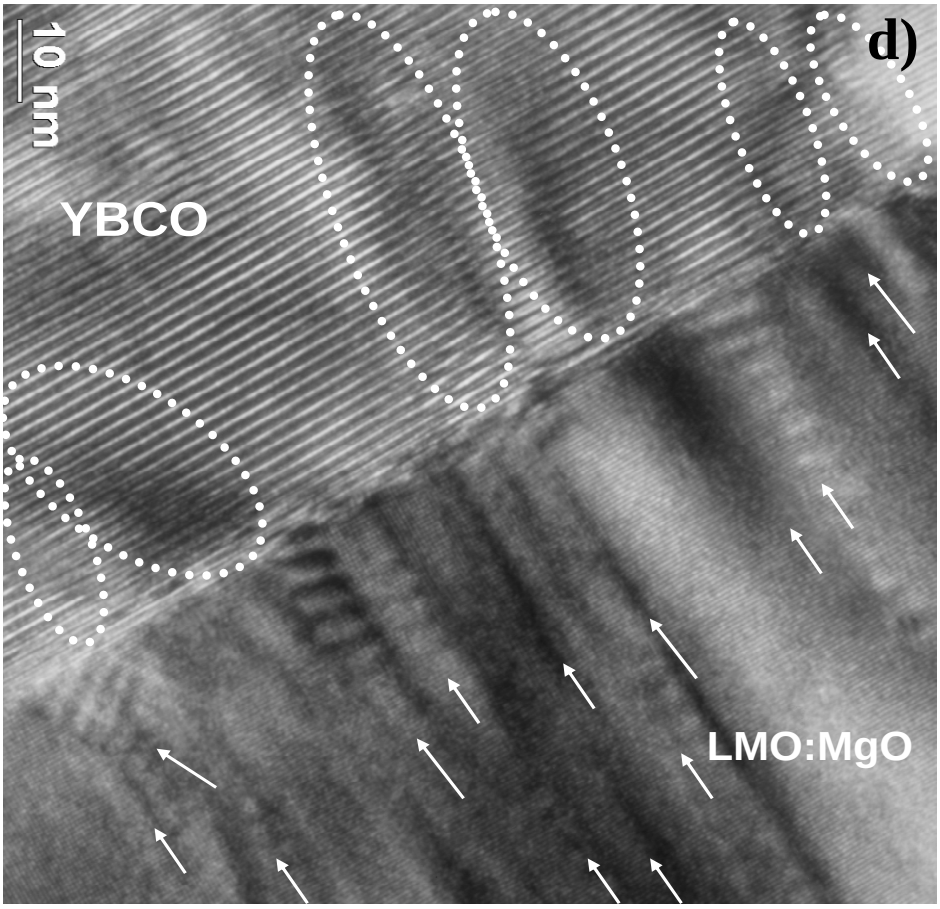

Figure 6.19 continued

Since the two distinct phases grow simultaneously, the mechanisms dictating the formation of the observed phase separated, vertical composite nanostructures are likely two-fold. i) thermodynamic stability combined with the insolubility of LMO and MgO driving the phase separation and; ii) minimization of the large lattice misfit strain (~ 7%) between LMO/MgO combined with preferential isostructural growth (based on the concept of lower interfacial energy) controlling the vertical self-assembly [100-108]. Propagation of extended defects into the YBCO matrix from the composite cap layer is also evident from Fig. 6.19c. A higher magnification image (Fig. 6.19d) reveals anti-phase boundaries and misfit dislocations (highlighted by dashed ovals) originating in the vicinity of the phase-separated MgO nanocolumns. Note that, owing to the large lattice misfit between YBCO and MgO (~ 9%), a significant strain is anticipated on or about the MgO nanocolumn during the HTS growth, which appears to generate of such extended defects within the YBCO matrix. In addition, it is likely that YBCO nucleation is disrupted in the vicinity of these columns, accelerating defect generation. Such extended defects are expected to provide additional pinning action, leading to J_c enhancement. Indeed, for this LMO:MgO(50%) on homo-epi MgO/IBAD-MgO sample, YBCO film yielded a 30% improvement in J_c(77 K) at 1 Tesla for $H \,||\, c$-axis. It should also be pointed out that not all MgO nanocolumns produce YBCO defects. This might be attributed to the highly anisotropic, rapid basal plane growth of YBCO that results in lateral overgrowth of MgO columns, similar to the observed meandering of YBCO grain boundaries about the straight boundaries of bicrystal substrates [111, 112].

We now consider the influence of these nanostructured composite cap layers on the superconductive transport properties of YBCO films. For technological relevance, results are presented for YBCO on composite cap layers grown directly on IBAD-MgO templates, along with typical data for a YBCO film fabricated on standard/pure LMO/IBAD-MgO [self-field J_c (77 K) = 2.2 × 10^6 A/cm^2]. Figure 6.20a exhibits J_c(77 K) versus magnetic field ($H \,||\, c$-axis) for YBCO films deposited on a series of LMO:MgO composite layers with varying MgO contents. YBCO films on the modified cap layers demonstrate significantly improved J_c compared to that obtained for the standard counterparts, despite the similar superconducting critical temperatures, T_c ~ 88-89 K. In particular, the relative improvement becomes more significant with increase in the magnetic field strength, indicating enhanced high-density pinning, consistent with the cross-section TEM of Fig. 6.19. Specifically, at 1 Tesla applied field, over 40% enhancement in J_c is found for cap layers modified with 5 vol% MgO. The self-field J_c(77 K) of this film was slightly higher, ~ 2.8 × 10^6 A/cm^2. However, J_c performance decreases with further increase in the MgO concentration, falling at or below the performance level of YBCO on the standard architectures at MgO content of 50 vol%. This behavior is consistent with the XRD observations, where an increase in misoriented grains was detected with higher MgO concentrations (see Fig. 6.16). Additional information as to the nature of flux pinning comes from the dependence of J_c on the field orientation, θ, with respect to sample normal for the same samples (unfortunately, data are not available for the 50 vol% MgO sample). Data presented in Fig. 6.20b also reveal significant improvement in J_c over wide range of orientations.

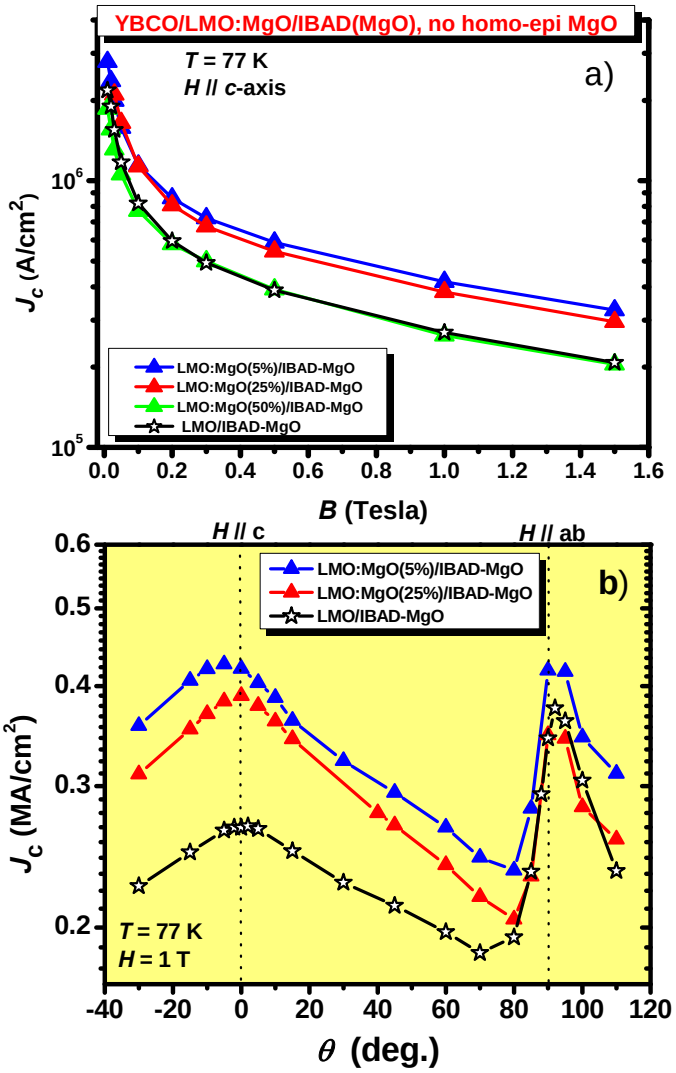

Figure 6.20: a) Comparison of 77 K transport critical current densities as a function of applied magnetic field (H || c-axis) for ~0.7-0.8 μm-thick YBCO films deposited on different MgO containing (5, 25, and 50 vol%) LMO:MgO composite films, as well as on reference standard LMO templates. Note that the sample modified with 25 vol% MgO is measured only up to B = 0.03 Tesla, since the sample was burned during the measurements due to contact heating. b) Angular dependence of J_c at 77 K and 1 Tesla for the same samples shown in part (a). Effect of LMO:MgO films on the angularly selective enhancement of J_c, in particular about the c-axis of the YBCO film is clearly evident from the figure.

In particular, these YBCO films show a much improved large peak about $H||c$-axis ($\theta = 0^{o}$), consistent with the field dependence data, and the presence of additional strong, uniaxial pinning defects approximately along this direction. Again, the TEM analysis shown in Fig. 6.19 corroborates these observations with visual evidence of *c*-axis correlated defects within the YBCO matrix. Interestingly, the reference YBCO/LMO/IBAD-MgO sample also shows a peak in $J_c(\theta = 0^{o})$, most likely arising from the dislocation cores at the low-angle grain boundaries and/or other naturally occurring *c*-axis aligned defects that are related to the growth process of YBCO. Similar trends in pinning performance are also attained for YBCO/LMO:MgO samples fabricated on homo-epi/IBAD-MgO templates.

In summary, these results indicate that the LMO buffer layer can be further functionalized to create vortex pinning defects within the HTS over layer, by incorporation of second phase MgO nanostructures.

Chapter 7

Conclusion

In this dissertation, we have characterized and analyzed YBCO-based second generation (2G) coated conductors in order to establish the limits of performance that are reachable, and addressed materials challenges to improve properties and further decrease the manufacturing cost of wires without compromising their performance levels.

In the first part of this thesis we have focused on the performance of the 2G wires in magnetic fields, where vortex-vortex and vortex-defects interactions determine the material's current conduction capability for technological applications. Of particular interest are the wide range studies of 'current-voltage' $E(J)$ characteristics of these wires, which provide understanding of the electrical properties of these materials in regimes of technological relevance. A combination of electrical and contactless magnetic–based methods - sweeping the magnetic field and observing the magnetic relaxation (current decay with time) - has been employed to broadly characterize and analyze the relevant superconductive properties as a function of temperature, magnetic field, orientation in field, and effective electric field levels commensurate with real devices. The E-J curves in the electric field region 10^{-5} to 10^{-13} V/cm exhibited a general power-law relation, $E \sim J^n$ for a wide range of temperatures (5-77 K) and magnetic fields (0.1-1.5 T). The observed downward curvatures in the log$E$-log$J$ plots arises naturally in vortex-glass and collective creep theories. It has been shown that the power law index n varies with temperature and applied magnetic field, with the n value decreasing as either the temperature or applied

magnetic field increases. Creep studies of the magnetic relaxation of the same materials showed that the persistent current density decreases logarithmically with time. At low temperatures, the obtained normalized relaxation rate $S(T)$ increases linearly with temperature, while a "universal plateau" develops at intermediate temperatures. At still higher temperatures, flux motion becomes progressively easier and the creep rate S increases with temperature as the irreversibility field is approached. Concurrently, the power-law index n decreases and energy dissipation in the material becomes progressively more significant.

In the second part we have concentrated on the materials development. Of specific concern were improvements in materials processing/performance that could potentially lead to reduced manufacturing cost of second generation superconducting wire production. First, we have studied various *rf*-magnetron sputter growth parameters/conditions for epitaxial growth of LMO layers directly on IBAD-MgO without homo-epi MgO layers. Results showed that while epitaxial growth of LMO can be achieved in a variety of sputtering gas mixtures, the deposition temperature has a strong effect on the crystalline quality of these films. Moreover, the cross sectional TEM analysis obtained for both architectures revealed that the interfaces between the YBCO and buffer layers are coherent, sharp, and free from cation diffusion. Electrical transport properties of 1 μm-thick PLD YBCO films on the simplified LMO/IBAD-MgO architecture showed comparable (if not better) performance, compared to those films deposited on templates having homo-epi MgO layers. More importantly, this result is found to be independent of the LMO thickness, which was varied from 30-240 nm. These

investigations may open a pathway for the fabrication of more efficient, robust and lower cost IBAD-based second generation HTS coated conductors. After establishing growth of pure LMO directly on IBAD-MgO template, as a next step we have further functionalized the standard LMO cap layer by replacing it with epitaxial LMO:MgO composite films. These sputter deposited, mixed phase films serve as a simplified template (successfully grown directly on IBAD-MgO) for the epitaxial growth as well as enhanced performance of YBCO films. The microstructural analysis of composite buffer films revealed formation of chemically phase separated, vertically aligned, and self-assembled MgO nanocolumns. These MgO columns extend through the entire thickness of the film matrix and induce additional *c*-axis correlated disorder within the subsequent YBCO films, effectively leading to improved pinning characteristics and higher in-field J_c performance. The present work strongly emphasizes the importance of nanostructure engineering for the realization of enhanced performance, increased efficiency, and reduced cost practical HTS wires.

Future Directions:

So far, enormous effort has been dedicated to characterization and fabrication of nanostructures. Perovskite oxides have grabbed enormous interest due to their unique and versatile physical properties for technological applications in magnetic, photonic, and spintronic applications. However, fabrication of such oxide materials is still challenging since their synthesis and characterization require sophisticated technology and experience. With the experience and knowledge that I gained through my research, I look

forward to productive and impactful research on the production and analysis of oxide nanostructures, together with their influence on the physical properties of the overall system produced.

The new developments in nanoscience and engineering have significantly impacted the performance of HTS materials, enabling them to carry higher J_c by introducing nanosized pinning centers such as BZO and $BaSnO_3$ (BSO) nanorods, nanoparticles, etc. I am interested in understanding and explaining the details of interactions between defect centers and vortices as well as interactions among vortices. I believe these investigations will have significant implications for the development and application of HTS materials.

List of References

References

1. H. K. Onnes, *Leiden Comm*. *B* **120** (1911).

2. J. G. Bednorz and K. A. Muller, *Z. Phys. B* **64**, 189 (1986).

3. M. K. Wu, J. R. Ashburn, C. J. Torng, P. H. Hor, R. L. Meng, L. Gao, Z. J. Huang, Y. Q. Wang, C. W. Chu*, Phys. Rev. Lett*. **58**, 908 (1987).

4. W. Meissner and R. Ochsenfeld, *Naturwissenschaften* **21**, 787 (1933).

5. F. London and H. London, *Proc. Roy. Soc. (London)* **A149**, 71 (1935).

6. V. L. Ginzburg and L.D. Landau, *Zh. Eksperim. i Teor. Fiz*. **20**, 1064 (1950).

7. A. A. Abrikosov, *JETP* **5**, 1174 (1957).

8. U. Essman and H. Traeuble, *Phys. Lett. A* **24**, 526 (1967).

9. D. Cribier, B. Jacrot, L. Madhav Rao and B. Farnoux, *Phys. Lett.* **9**, 106 (1964).

10. H. W. Weber, *et al, Phys. Status Solidi (b)* **57**, 515 (1973).

11. J. Bosch R. Gross, M. Koyanagi, and R. P. Huebener, *Phys. Rev. Lett*. **54**, 1448 (1985).

12. T. Matsuda, S. Hasegawa, M. Igarashi, T. Kobayashi, M. Naito, H. Kajiyama, J. Endo, N. Osakabe, A. Tonomura, R. Aoki, *Phys. Rev. Lett*. **62**, 2519 (1989).

13. A. M. Chang, H. D. Hallen, H. F. Hess, H. L. Kao, J. Kwo, A. Sudbo, T. Y. Chang, *Europhys. Lett*. **20**, 645 (1992).

14. P. W. Anderson, *Phys. Rev*. **9**, 309 (1962).

15. P. W. Anderson and Y. B. Kim, *Rev. Mod. Phys*. **36**, 39 (1964).

16. Y. Xu, M. Suenaga, A. R. Moodenbaugh, and D. O. Welch, *Phys. Rev. B* **40**, 10882 (1989).

17. M. R. Beasley, R. Labusch, and W. W. Webb, *Phys. Rev*. **181**, 682 (1969).

18. M. P. A. Fisher, *Phys. Rev. Lett*. **62**, 1415 (1989).

19. D. S. Fisher, M. P. A. Fisher, and D. A. Huse, *Phys. Rev*. *B* **43**, 130 (1991).

20. R. H. Koch, V. Foglietti, W. J. Gallagher, G. Koren, A. Gupta, and M. P. A. Fisher, *Phys. Rev Lett*. **63**, 1511 (1989).

21. R. H. Koch, V. Foglietti, and M. P. A. Fisher, *Phys. Rev Lett*. **64**, 2586 (1990).

22. M. V. Feigel'man, V. B. Geshkenbein, A. I. Larkin, and V. M. Vinokur, *Phys. Rev. Lett*. **63**, 2303 (1989).

23. G. Blatter, M. V. Feigel'man, V. B. Geshkenbein, A. I. Larkin, V. M. Vinokur, *Rev. Mod. Phys*. **66**, 1125 (1994).

24. C. P. Bean, *Phys. Rev. Lett.* **8,** 250 (1962).

25. Bean C. P. *Rev. Mod. Phys*. **36**, 31 (1964).

26. M. Campbell and J. E. Evetts, *Advances in Physics* **21**, 199-428 (1972) (Reprinted in *Advances in Physics* **50**, 1249-1449 (2001)).

27. M. P. Paranthaman and T. Izumi, *Mater. Res. Soc. Bull*. **29**, 533 (2004).

28. J. L. MacManus-Driscoll, S. R. Foltyn, Q. X. Jia, H. Wang, A. Serquis, L. Civale, B. Maiorov, M. E. Hawley, M. P. Maley and D. E. Peterson, *Nature Mater*. **3**, 439 (2004).

29. A. Goyal, S. Kang, K. J. Leonard, P. M. Martin, A. A. Gapud, M Varela, M Paranthaman, A. O. Ijaduola, E. D. Specht, J. R. Thompson, D. K. Christen, S. J. Pennycook and F. A. List, *Supercond. Sci. Technol.* **18**, 1533 (2005).

30. K. Matsumoto, T. Horide, K. Osamura, M. Mukaida, , Y. Yoshida, A. Ichinose, and S. Horii, *Physica C* **412–414**, 1267–1271 (2004).

31. T. Haugan, P. N. Barnes, R. Wheeler, F. Meisenkothen, M. Sumption, *Nature* **430**, 867 (2004).

32. C. V. Varanasi, P. N. Barnes, J. Burke, L. Brunke, I. Maartense, T. J. Haugan, E. A. Stinzianni, K. A. Dunn, P. Haldar, *Supercond. Sci. Technol.* **19**, L37–L41 (2006).

33. C. Kwon, L. R. Kinder, Y. Gim, Y. Fan, J. Y. Coulter, M.P. Maley, S. R. Foltyn, D. E. Peterson, Q. X. Jia, *IEEE Trans. Appl. Supercond.* **9**, 1575–1578 (1999).

34. A. K. Pradhan, M.Muralidhar, M. Murakami, Koshizuki, *Supercond. Sci. Technol.* **13**, 761 (2000).

35. M. Konishi, K. Takahashi, A. Ibi, T. Muroga, S. Miyata, H. Kobayashi, Y. Yamada and Y. Shiohara, *Physica C* **445–448**, 633–636 (2006).

36. B. Cai, B. Holzapfel, J. Hanisch, L. Fernandez, L. Schultz, *Phys. Rev. B* **69**, 104531 (2004).

37. C. Kwon, L. R. Kinder, Y. Fan, Y. Gim, A. T. Findikoglu, J. F. Bingert, J. Y. Coulter, S. R. Foltyn, D. E. Peterson, Q. X. Jia, *Phil. Mag. B* **80**, 45 (2000).

38. T. Aytug, M. Paranthaman, A. A. Gapud, S. Kang, H. M. Christen, K. J. Leonard, P. M. Martin, J. R. Thompson, D. K. Christen, R. Meng, I. Rusakova, C. W. Chu, T. H. Johansen, *J. Appl. Phys.* **98**, 114309 (2005).

39. A. Crisan, S. Fujiwara, J. C. Nie, A. Sundaresan, H. Ihara, *Appl. Phys. Lett.* **79**, 4547 (2001).

40. P. Mele, K. Matsumoto, T. Horide, O. Miura, A. Ichinose, M. Mukaida, Y. Yoshida, and S. Horii, *Physica C* 445–448, 648 (2006).

41. K. Hasegawa, K. Fujino, H. Mukai, M. Konishi, K. Hayashi, K. Sato, S. Honjo, Y. Sato, H. Ishii, and Y. Iwata, *Appl. Superconduct*. **4**, 487 (1996).

42. U. Balachandran, M. Li, R.E. Koritala, B.L. Fisher and B. Ma, *Physica C* **372**, 869 (2002).

43. D. P. Norton, A. Goyal, J. D. Budai, D. K. Christen, D. M. Kroeger, E. D. Specht, Q. He, B. Saffian, M. Paranthaman, C. E. Klabunde, D.F. Lee, B. C. Sales, and F. A. List, *Science* **274**, 755 (1996).

44. A. Goyal, D. P. Norton, D. K. Christen, E. D. Specht, M. Paranthaman, D.M. Kroeger, J. D. Budai, Q. He, F. A. List, R. Feenstra, H. R. Kerchner, D. F. Lee, E. Hatfield, P. M. Martin, J. Mathis, and C. Park, *Appl. Superconduct*. **4**, 403 (1996).

45. M. W. Rupich, U. Schoop, D. T. Verebelyi, C. Thieme, W. Zhang, X. Li, T. Kodenkandath, N. Nguyen, E. Siegal, D. Buczek, J. Lynch, M. Jowett, E. Thompson, J. S. Wang, J. Scudiere, A. P. Malozemoff, Q. Li, S. Annavarapu, S. Cui, L. Fritzemeier, B. Aldrich, C. Craven, F. Niu, R. Schwall, A. Goyal, M. Paranthaman, *IEEE Trans. Appl. Supercond.* **13**, 2459 (2003).

46. C. P. Wang, K. B. Do, M. R. Beasley, T. H. Geballe, and R. H. Hammond, *Appl. Phys. Lett*. **71**, 2955 (1997).

47. J. R. Groves, P. N. Arendt, S. R. Foltyn, R. F. DePaula, C. P. Wang, and R. H. Hammond, *IEEE Trans Appl. Supercond.* **9**, 1964 (1999).

48. K. Hasegawa, K. Fujino, H.Mukai, M. Konishi, K. Hayashi, K. Sato, S. Honjo, Y. Sato, H. Ishii, and Y. Iwata, *Appl. Supercond*. **4**, 487 (1996).

49. K. Hasegawa, N. Hobara, Y. Nakamura, T. Izumi, and Y. Shiohara, *Physica C* **354**, 424 (2001).

50. A. Goyal, D. P. Norton, J. D. Budai, M. Paranthaman, E. D. Specht, D. M. Kroeger, D. K. Christen, Q. He, B. Saffian, F. A. List, D. F. Lee, P. M.

Martin, C. E. Klabunde, E. Hartfield, V. K. Sikka, *Appl. Phys. Lett*. **69**, 1795 (1996).

51. Q. He, D. K. Christen, J. D. Budai, E. D. Specht, D. F. Lee, A. Goyal, D. P. Norton, M. Paranthaman, F. A. List and D. M. Kroeger, *Physica C* **275**, 155 (1997).

52. M. Paranthaman, A. Goyal, F. A. List, E. D. Specht, D. F. Lee, P. M. Martin, Q. He, D. K. Christen, D. P. Norton, J. D. Budai and D. M. Kroeger, *Physica C* **275**, 266 (1997).

53. Y. Iijima, N. Tanabe, O. Kohno, Y. Ikeno, *Appl. Phys. Lett*. **60**, 769 (1992).

54. Y. Iijima, N. Kaneko, Y. Sutoh, K. Kakimoto, T. Saitoh, T. Kato, T. Hirayama, *Physica C,* **426-431**, 899 (2005).

55. C. P. Wang, K. B. Do, M. R. Beasley, T. H. Geballe, and R. H. Hammond, *Appl. Phys. Lett*. **71**, 2955 (1997).

56. X. Xuming, K. P. Lenseth, J. L. Reeves, A. Rar, Q. Yunfei, R. M. Schmidt, C. Yimin, L. Yijie, X. Y. Yuan, V. Selvamanickam, *IEEE Trans. Appl. Supercond*. **17**, 3375 (2007).

57. P. N. Arendt and S. R. Foltyn, *Mater. Res. Soc. Bull*. **29**, 543 (2004).

58. J. R. Groves, P. N. Arendt, S. R. Foltyn, R. F. DePaula, E. J. Peterson, T. G. Holesinger, J. Y. Coulter, R. W. Springer, C. P. Wang, R. H. Hammond, *IEEE. Trans. Appl. Supercond*. **9**, 1964 (1999).

59. J. R. Groves, P. N. Arendt, S. R. Foltyn, Q. X. Jia, T. G. Holesinger, L. A. Emmert, R. F. DePaula, P. C. Dowden, L. Stan, *IEEE Trans. Appl. Supercond*. **13**, 2651 (2003).

60. M-H Yang and C. P. Flynn, *J. Phys.:Condens. Matter*. **8**, L279 (1996).

61. A. Goyal, M. Paranthaman, and U. Schoop, *Mater. Res. Soc. Bull*. **29**, 552 (2004).

62. M. Paranthaman, T. Aytug, D. K. Christen, P. N. Arendt, S. R. Foltyn, J. R. Groves, L. Stan, R. F. DePaula, H. Wang, T. G. Holesinger, *J. Mater. Res.* **18**, 2055 (2003).

63. M. P. Paranthaman, T. Aytug, S. Kang, R. Feenstra, J. D. Budai, D. K. Christen, P. N. Arendt, L. Stan, J. R. Groves, R. F. DePaula, S. R. Foltyn, T. G. Holesinger, *IEEE Trans. Appl. Supercond*. **13**, 2481 (2003).

64. Q. X. Jia, S. R. Foltyn, P. N. Arendt, J. R. Groves, T. G. Holesinger, M. E. Hawley, and P. Lu, *Appl. Phys. Lett*. **81**, 4571 (2002).

65. H. Wang, S.R. Foltyn, P.N. Arendt, Q.X. Jia, J.L. MacManus-Driscoll, L. Stan, Y. Li, X. Zhang, and P.C. Dowden, *J. Mater. Res.* **19**, 1869 (2004).

66. S. J. Pennycook, D. E. Jesson, *Ultramicroscopy* **37**, 14 (1991).

67. J. Liu, *Electron Microscopy* **1**, 32 (1990).

68. R. F. Loane, P. Xu, and J. Silcox, *Ultramicroscopy* **40**, 121 (1992).

69. H. Lakner, M. Maywald, L. J. Balk, and E. Kubalek, *Surf. Interface Anal*. **19**, 374 (1992).

70. Y. Yamasaki and Y. Mawatari, *IEEE Trans. Appl. Supercond*. **9**, 2651 (1999).

71. J. R. Thompson, Y. R. Sun, D. K. Christen, L. Civale, A. D. Marwick, and F. Holtzberg, *Phys. Rev. B* **49**, 13287 (1994).

72. J. R. Thompson, Y. R. Sun, and F. Holtzberg, *Phys. Rev. B* **44**, 458 (1991).

73. A. P. Malozemoff and M. P. A. Fisher, *Phys. Rev. B* **42**, 6784 (1990).

74. J. R. Thompson, O. Polat, D. K. Christen, D. Kumar, P. M. Martin, and J. W. Sinclair, *Appl. Phys. Lett*. **93**, 042506 (2008).

75. D. K. Christen and J. R. Thompson, *Nature* **98**, 364 (1993).

76. G. Blatter, V. B. Geshkenbein, and A. I. Larkin, *Phys. Rev Lett* **68**. 875 (1992).

77. D. R. Nelson and V. M. Vinokur, *Phys. Rev. B* **48**, 13060 (1993).

78. T. Hwa, P. L. Doussal, D. R. Nelson, and V. M. Vinokur, *Phys. Rev. Lett.* **71**, 3545 (1993).

79. L. Krusin-Elbaum, L. Civale, J. R. Thompson, C. Feild. *Phys. Rev. B* **53**, 11744 (1996).

80. C. J. van der Beek, M. Konczykowski, V. M. Vinokur, T. W. Li, P. H. Kes, and G. W. Crabtree, *Phys. Rev Lett* **74**, 1214 (1995).

81. V. V. Moshchalkov, V. V. Metlushko, G. Güntherodt, I. N. Goncharov, A. Yu. Didyk, and Y. Bruynseraede, *Phys. Rev. B* **50**, 639 (1994).

82. B. Martinez, X. Obradors, A. Gou, V. Gomis, S. Pinol, J. Fontcuberta, and H. Van Tol, *Phys. Rev. B* **53**, 2797 (1996).

83. J. Plain, T. Puig, F. Sandiumenge, X. Obradors, and J. Rabier, *Phys. Rev. B* **65**, 104526 (2002).

84. L. Civale, *Supercond. Sci. Technol*. **10**, A11 (1997).

85. Y. Yeshurun, A. P. Malozemoff, and A. Shaulov, *Rev. Mod. Phys*. **68**, 911 (1996).

86. M. P. Maley, J. O. Willis, H. Lessure, and M. E. McHenry, *Phys. Rev. B* **42**, 2639 (1990).

87. L. Stan, P. N. Arendt, I. O. Usov , H. Wang, S. R. Foltyn, B. Maiorov, J. R. Groves, R. F. De Paula, and Y. Li, *J. Mater. Res.* **22**, 1082 (2007).

88. D.P. Norton, D. H. Lowndes, J. D. Budai, D. K. Christen, E. C. Jones, K. W. Lay, and J. E Tkaczyk, *Appl. Phys. Lett*. **57**, 1164 (1990).

89. S. R. Foltyn, P. Tiwari, R. C. Dye, M. Q. Le, and X. D. Wu, *Phys. Lett*. **63**, 1848 (1993).

90. Ö. Polat, T. Aytug, M. Paranthaman, K. Kim, Y. Zhang, P. M. Martin, J. R. Thompson, D. K. Christen, X. Xiong, and V. Selvamanickam, *J. Mater. Res*. **23**, 3021 (2008).

91. D. E. Farrell, J.P. Rice, D. M. Ginsberg, and J. Z. Liu, *Phys. Rev. Lett*. **64**, 1573 (1990).

92. W. K. Kwok, S. Fleshler, U Welp, V. M. Vinokur, J. Downey, G. W. Crabtree, and M. M. Miller, *Phys. Rev. Lett*. **69**, 3370 (1992).

93. A. Schilling, R.A. Fisher, N. E. Phillips, U. Welp, D. Dasgupta, W. K. Kwok, and G. W. Crabtree, *Nature* **382**, 791 (1996).

94. L. Civale, B. Maiorov, A. Serquis, J. O. Willis, J. Y. Coulter, H. Wang, Q. X. Jia, P. N. Arendt, J. L. MacManus-Driscoll, M. P. Maley, and S. R. Foltyn, *Appl. Phys. Lett*. **84**, 2121 (2004).

95. M. P. Paranthaman and Venkat Selvamanickam, "Flux Pinning and AC Loss in Second Generation High Temperature Superconductor Wires," Book chapter in *Flux Pinning and AC Loss Studies on YBCO Coated Conductors*, Nova Science Publishers Inc., New York, pp. 3-10 (2007).

96. S. Kang, A. Goyal, J. Li, A.A. Gapud, P.M. Martin, L. Heatherly, J.R. Thompson, D.K. Christen, F.A. List, M. Paranthaman, and D.F. Lee, *Science* **311**, 1911 (2006).

97. Q. X. Jia, S. R. Foltyn, P. N. Arendt, and J. F. Smith, *Appl. Phys. Lett*. **80**, 1601 (2002).

98. S. R. Foltyn, H. Wang, L. Civale, B. Maiorov, Y. Li, M. P. Maley, and J. L. MacManus-Driscoll, *Appl. Phys. Lett*. **87**, 162505 (2005).

99. A. A. Gapud, D. Kumar, S. K. Viswanathan, C. Cantoni, M. Varela, J. Abiade, S. J. Pennycook and D. K. Christen, *Supercond. Sci. Technol.* **18**, 1502 (2005).

100. C. Teichert, M. G. Lagally, L. J. Peticolas and J. C. Bean, and J. Tersoff, *Phys. Rev. B* **53**, 16334 (1996).

101. Q. Xie, A. Madhukar, P. Chen, and N. P. Kobayashi, *Phys. Rev. Lett*. **75**, 2542 (1995).

102. L. G. Wang, P. Kratzer, M. Scheffler, and N. Moll, *Phys. Rev. Lett*. **82**, 4042 (1999).

103. Z. Gai, B. Wu, J. P. Pierce, G. A. Farnan, D. Shu, M. Wang, Z. Zhang, and J. Shen, *Phys. Rev. Lett.* ***89,*** 235502 (2002).

104. O. I. Lebedev, J. Verbeeck, G. Van Tendeloo, O. Shapoval, A. Belenchuk, V. Moshnyaga, B. Damashcke, and K. Samwer, *Phys. Rev. B* **66**, 104421 (2002).

105. H. Zheng, J. Wang, S. E. Lofland, Z. Ma, L. Mohaddes-Ardabili, T. Zhao, L. Salamanca-Riba, S. R. Shinde, S. B. Ogale, F. Bai, D. Viehland, Y. Jia, D. G. Schlom, M. Wuttig, A. Roytburd, and R. Ramesh, *Science* **303**, 661 (2004).

106. J. L. MacManus-Driscoll, P. Zerrer, H. Wang, H. Yang, J. Yoon, A. Fouchet, R. Yu, M. G. Blamire, and Q. X. Jia, *Nature Materials* **7,** 314 (2008).

107. H. Zheng, F. Straub, Q. Zhan, P. Yang, W.K. Hsieh, F. Zavaliche, Y.H. Chu, U. Dahmen, and R. Ramesh, *Adv. Mater.* **18**, 2747 (2006).

108. Y. F. Gao, J. Y. Meng, A. Goyal, and G. M. Stocks, *J. Metals* **60**, 54 (2008).

109. S. H. Wee, J. Shin, C. Cantoni, H. M. Meyer, S. Cook, Y. L. Zuev, E. Specht, X. M. Xiong, M. P. Paranthaman, V. Selvamanickam, and A. Goyal, *Appl. Phys. Express* **2**, 063008 (2009).

110. O. Polat, T. Aytug, M. Paranthaman, K. Kim, Y. Zhang, C. Cantoni, Y. L. Zuev, A. Goyal, J. R. Thompson, D. K. Christen, X. Xiong, and V. Selvamanickam, *IEEE Trans. Appl. Supercond*. **19**, 3315 (2009).

111. X.F. Zhang, D.J. Miller, and J. Talvacchio, *J. Mater. Res*. **11**, 2440 (1996).

112. K. E. Gray, M. B. Field, and D. J. Miller, *Phys. Rev. B* **58**, 9543 (1998).

Appendix

Publications and Presentations by Ö. Polat

Publications

1. **O. Polat**, T. Aytug, M. Paranthaman, K. Kim, Y. Zhang, S. W Cook, X. Qiu, K. J. Leonard, H. M. Meyer, A. R. Lupini, X. Xiong, V. Selvamanickam, A. Goyal, S. J. Pennycook, J.R.Thompson, and D.K. Christen "Pinning Enhancements in $YBa_2Cu_3O_{7-x}$ Superconductors through Phase Separated, Self-assembled $LaMnO_3$ Nanocomposite Films" *J. Mater. Res*. submitted (2009).
2. **O. Polat**, T. Aytug, M. Paranthaman, K. Kim, Y. Zhang, C. Cantoni, Y.L. Zuev, A. Goyal, J.R. Thompson, D.K. Christen, X. Xiong, and V. Selvamanickam, "Properties of YBCO on $LaMnO_3$-capped IBAD MgO-templates without homo-epitaxial MgO layer," *IEEE Trans. Appl. Supercond*. **19**, 3315 (2009).
3. **O. Polat**, T. Aytug, M. Paranthaman, K. Kim, Y. Zhang, J.R. Thompson, D.K. Christen, X. Xiong, and V. Selvamanickam, "Direct growth of $LaMnO_3$ cap buffer layers on IBAD-MgO for simplified template-based YBCO coated conductors," *J. Mater. Res.* **23**, 3021 (2008).
4. J. R. Thompson, **O. Polat**, D. K. Christen, D. Kumar, P. M. Martin, J. W. Sinclair, "Wide-Range Characterization of Current Conduction in High-T_c Coated Conductors," *Appl.Phys. Lett*. **93**, 042506 (2008).

5. **O. Polat**, J. R. Thompson, D. K. Christen, D. Kumar, P. M. Martin, J. W. Sinclair, S. Cook "Characterization of Current Conduction in GdYSmBCO Thin Film via Transport and Contactless Methods," book chapter submitted.
6. **O. Polat**, J. R. Thompson, D. K. Christen, D. Kumar, J. W. Sinclair, Y. Zuev "Thickness dependence of Magnetic Relaxations and E-J Characteristics in GdYBCO Thin Films," in preparation.

7. Xiaofeng Oiu, Jane Y. Howe, Mateus B. Cardoso, **Ozgur Polat**, William T. Heller, and M. Parans Paranthaman, "Size Control of Highly Ordered HfO_2 Nanotube Arrays and A Possible Growth Mechanism," *Nanotechnology* **20**, 455601 (2009).

Presentations

1. Materials Research Society spring meeting, San Francisco CA, (March 2009), "Enhanced Flux Pinning in YBCO Films via Defects Created by Mixed Phase Substrate Cap Layers" (Talk)
2. Applied Superconductivity Conference, Chicago IL, (Aug 2008), "Direct growth of $LaMnO_3$ cap layers on IBAD-MgO template for YBCO coated conductors" (Talk)
3. Materials Research Society spring meeting, San Francisco CA, (March 2008), "Direct growth of $LaMnO_3$ cap layers on IBAD-MgO (without homo-epi MgO) for simplified IBAD template based YBCO coated conductors" (Talk)

Vita

Ozgur Polat was born in Zara, Turkey. After graduation in 1994 from Kadikoy Mehmed Bayazid high school in Istanbul, he attended Ankara University, from which he graduated with a B.Sc. in Engineering Physics in 1999. Then he proceeded to studies for a Masters degree in Physics at the Middle East Technical University (METU) in Ankara, Turkey. He earned his Masters in Experimental High Energy Physics in 2003. He arrived in US in 2005 as a research/teaching assistant at The University of Tennessee, Knoxville. In August 2006, he joined the group of Dr. James R. Thompson and Dr. Tolga Aytug as a graduate research assistant. While at UT, he was honored with a Chancellor's award for Extraordinary Professional Promise. He received the degree of Doctor of Philosophy with a major in Physics in December 2009.